LAWRENCE
LIVERMORE
NATIONAL
LABORATORY

UCRL-TH-207378

A High-Energy, Ultrashort-Pulse X-Ray System for the Dynamic Study of Heavy, Dense Materials

D.J. Gibson

October 20, 2004

This work was performed under the auspices of the U.S. Department of Energy by University of California, Lawrence Livermore National Laboratory under Contract W-7405-Eng-48.

A High-Energy, Ultrashort-Pulse X-Ray System for the

Dynamic Study of Heavy, Dense Materials

by

DAVID JEREMY GIBSON

B. S. (Harvey Mudd College) 1998

M.S. (University of California, Davis) 2003

DISSERTATION

Submitted in partial satisfaction of the requirements for the degree of

DOCTOR OF PHILOSOPHY

in

Applied Science – Engineering

in the

OFFICE OF GRADUATE STUDIES

of the

UNIVERSITY OF CALIFORNIA

DAVIS

Approved:

_____

_____

_____

Committee in Charge

2004

This work was performed under the auspices of the U.S. Department of Energy

by University of California, Lawrence Livermore National Laboratory

under Contract W-7405-Eng-48.

Abstract

Thomson-scattering based x-ray radiation sources, in which a laser beam is scattered off a relativistic electron beam resulting in a high-energy x-ray beam, are currently being developed by several groups around the world to enable studies of dynamic material properties which require temporal resolution on the order of tens of femtoseconds to tens of picoseconds. These sources offer pulses that are shorter than available from synchrotrons, more tunable than available from so-called $K_{\square}$ sources, and more penetrating and more directly probing than ultrafast lasers. Furthermore, Thomson-scattering sources can scale directly up to x-ray energies in the few MeV range, providing peak brightnesses far exceeding any other sources in this regime. This dissertation presents the development effort of one such source at Lawrence Livermore National Laboratory, the Picosecond Laser-Electron InterAction for the Dynamic Evaluation of Structures (PLEIADES) project, designed to target energies from 30 keV to 200 keV, with a peak brightness on the order of 10^{18} photons·s^{-1}·mm^{-2}·$mrad^{-2}$·0.01% $bandwidth^{-1}$. A 10 TW Ti:Sapphire based laser system provides the photons for the interaction, and a 100 MeV accelerator with a 1.6 cell S-Band photoinjector at the front end provides the electron beam. The details of both these systems are presented, as is the initial x-ray production and characterization, validating the theory of Thomson scattering. In addition to the systems used to enable PLEIADES, two alternative systems are discussed. An 8.5 GHz X-Band photoinjector, capable of sustaining higher accelerating gradients and producing lower emittance electron beams in a smaller space than the S-Band gun, is presented, and the initial operation and commissioning of this gun is presented. Also, a hybrid chirped-pulse amplification system is presented as an alternative to the standard regenerative amplifier technology in high-power ultrafast laser systems. This system combines an optical-parametric chirped-pulse amplification (OPCPA) system with a titanium:sapphire-based four-pass amplifier to provide the high pre-pulse contrast and ease of assembly of an OPCPA using a commercial pump laser while avoiding the loss of efficiency such a system would normally entail.

Acknowledgements

No dissertation would be complete without the long list of names the casual reader will have no interest in. Perhaps the acknowledgements never get read, but they do an excellent job of allowing an author to relieve his conscience where credit is due.

Let's begin with the professional thank-yous. First, on the X-Band accelerator project, I must thank Dr. Neville C. Luhmann, Jr., who took me into his group as a graduate student, and allowed me to remain behind when that effort was transferred to SLAC. Thanks here go also in great amounts to Eric Landahl, then-fellow DAS graduate student, who brought me up to speed on all the important aspects of both the experiment and grad school life; it's hard to determine which is more valuable. On the HCPA portion of the project, thanks go to Igor Jovanovic, who passed his Ph.D. research hardware on to me to improve upon, and on more than one occasion saved me countless hours of head-scratching with a simple mirror tweak. I also appreciate the occasional conversation with Chris Ebbers, who warned me of many of the common problems one encounters in dealing with nonlinear processes (some of which I managed to find despite his efforts).

As 8.5 GHz made way for 11.4 GHz and the accelerator expertise of SLAC, I moved to the PLEIADES project (then known only as the Thomson Scattering SI). There, Paul Springer, the project PI, was kind enough to take me on as a member of that team (he had previously gotten me started here at the lab the summer before classes began, another reason for appreciation). PLEIADES was successful due to the large number of very skilled people who worked together to get the system up and running, and I would be remiss to not acknowledge their efforts. For the accelerator side of things, as well as the electrical and mechanical engineering work, thanks go to: Gerry Anderson, Scott Anderson, Jeremy Jacob, Lynn James, Bill Patterson, Chris Robins, Vince Tsai, Aaron Tremaine, and several others with whom my personal contact was too spurious to recall, but were nonetheless crucial to running the B194 Linac. For the system diagnostics (streak camera, CCD, etc.), I am indebted to Rex Booth, Winthrop Brown, and Jaroslav Kuba for helping to make them work, and helping me figure out what to make of the data.

Then, there is the laser side. This is where I spent most of my time, so the greatest thanks go here. Rick Cross and John Crane, with whom I worked on a daily basis, always made sure all the bits were there when I needed them, and figured out why things didn't work when I wasn't able to. It is so much easier to produce good scientific result when you have someone as skilled as Shawn Betts to answer when you call out "Hey, this laser broke again!" (or to save you from having to enter the grimy linac escape tubes during interlock checks). Finally, thanks are owed to David Fittinghoff for, among other things, explaining the intricacies of ultrashort-pulse measurement, driving the initial PLEIADES results, and repeatly reviewing the text of my papers to make sure I didn't sound too dumb.

Through all the phases of this dissertation, Fred Hartemann was around providing guidance and support, both academic and bureaucratic, and made sure I kept moving the right direction. We worked closely together getting the X-Band gun final results, successfully commissioning it before its all-to-abrupt decommissioning, and he explained all the Thomson scattering theory in a way that I was able to understand (conceptually, if not mathematically) immediately. Finally, I must thank my committee: Rick Freeman, who took over my committee when I left Dr. Luhmann's group, Hector Baldis, who stood by me through bureaucratic wrangling and provided excellent advice for dealing with problems, and Dr. Chris Barty, who's weekly meetings and innumerable suggestions really led my way through the maze of scientific endeavor.

Financially, I must thank Don Hoffman, Charlie Westbrook, and the Student Employee Graduate Research Fellowship program, who took care of all the lab paperwork, insulated me from the lab bureaucracy, and provided funding for the first five years of my research, allowing me to concentrate on classwork and research without worrying about who was going to pay. Also, I need to thank Ed Hartouni for taking me into N-Division when my Fellowship ended, allowing me to complete my work over this last year.

Personal thank-yous go first to Paul Steele, former Mudder and ex-roommate, and fellow DAS student, who was always around to answer my silly questions about physics I could never remember, reassure me that I wasn't alone in my feelings of inadequacy, or just to provide something to do at lunch. My roommate Justin Isaac has kept me sane at home, dragging me

away from work when necessary to do some all-to-often-needed decompression, and whipping up dinners for me when accelerator runs last late into the night, after the City of Livermore shuts down. Finally, of course, thanks aren't enough for my parents, John and Candis, and my brother, Mark, who have spent the last 28 years supporting me in everything, as much as any son could wish. They are the reason I am here today to write this.

Those who I have left out, be assured it was merely because my enfeebled brain is unable to recall you as I write this – no doubt once this dissertation is filed I'll remember a dozen people who deserved full recognition. Feel free to direct your complaint towards me.

Chapter 1. Introduction

The unique conditions of atomic-scale interactions impose stringent requirements on any potential experimental probe of such phenomena. The characteristic spatial scale is given by the size of an atom, which is on the order of 1 ångstrom (10^{-10} m). For example,, the spacing of atoms in a crystal of silicon is[1] 5.43 Å This length scale is considerably shorter than, for example, the wavelength of visible light, with is typically on the order of 0.4 – 0.7 μm. Meanwhile, the characteristic time scale of atomic level changes, such as non-thermal melting[2] or shock-induced phase changes[3], is determined by the atomic vibrational period, which is typically on the order of hundreds of femtoseconds to a few picoseconds.

The obvious solution to the first requirement – a short distance scale – is the use of x-rays. Within months of their discovery by Wilhelm Roentgen in November 1895 (winning him the first Nobel prize in physics in1901), x-rays were being used as an invaluable medical diagnostic due to their penetration depth, which can be orders of magnitude greater than that of visible light through opaque objects. The work of Max von Laue and William and Lawrence Bragg (again earning Nobel prizes in 1914 and 1915, respectively), demonstrated the use of the short wavelength of x-rays to make atomic-structure based measurements via diffraction of x-rays off crystal lattices. X-rays have benefits in addition to their small wavelength. If structure of an atomic system is to be studied, the best indicator will be the locations of inner-shell electrons, which are most closely bound to the nuclei. These electrons are bound with energies on the order of thousands of electron volts, and so are well suited for study with x-rays. Optical light would instead probe the outermost, least bound electrons.

The solution to the second requirement – a fast time scale – came with the advent of ultrafast lasers. To measure fast phenomena, either a fast detector or a fast probe of the subject is needed. For example, if you wanted to catch an image of a bullet in flight, you could either get a very high-speed camera, which could capture an image of the flying bullet on a short timescale relative to it's motion, or you could use a slower camera, and instead use a strobe light to image the bullets position at a specific moment of time. Modern detector technology can't effectively get

much shorter than a picosecond or so. Streak cameras have been demonstrated[90] with resolution down to a few hundred femtoseconds, but the signal-to-noise ratio is typically poor. This leaves, as the most feasible choice, a fast probe signal, which is where ultrafast lasers come in to play. Q-switched lasers, wherein all the energy of the cavity is released in a short burst, create pulse-lengths on the order of several nanoseconds[4]. Mode-locked lasers[5], wherein several different longitudinally allowed cavity modes are phase-locked to each other, adding coherently to produce femtosecond scale laser pulses, pushed the ultrafast science field to the forefront. which has resulted in pulse durations less than 5 fs[6]. These pulses have been used to make numerous measurements on ultrashort timescales, such as studies of optically induced phase transitions in semiconductors[2,7-9], the evolution of chemical reactions[10], and optical phonon excitation[11]. The problem with using ultrafast lasers for atomic-scale measurements is that such systems all operate in the 0.1 – 1 μm range, and therefore run immediately into the length scale problem discussed above. Furthermore, the long wavelengths of the light are orders of magnitude larger than the atomic spacing, and so would average over large atomic volumes.

What is therefore most needed is an ultrafast (fs-ps) x-ray source.

1.1 Approaches to Ultrafast X-Rays

There are several different ways to create short x-ray pulses. The relevant figure of merit for an x-ray source is what is termed the "peak spectral brightness". Essentially, it is a measure of the number of photons available in some small volume of the beam space: having a certain energy, in a certain time window, going in a certain direction, and coming from a certain point. The brightness typically is quoted in units of

$$\frac{photons}{mm^2 \cdot mrad^2 \cdot s \cdot 0.1\%\ bandwidth}$$

The energy range and brightness of a few of sample sources are summarized in Figure 1, and include synchrotrons, non-thermal laser plasmas, x-ray FELs, and Thomson scattering sources. These schemes are reviewed here.

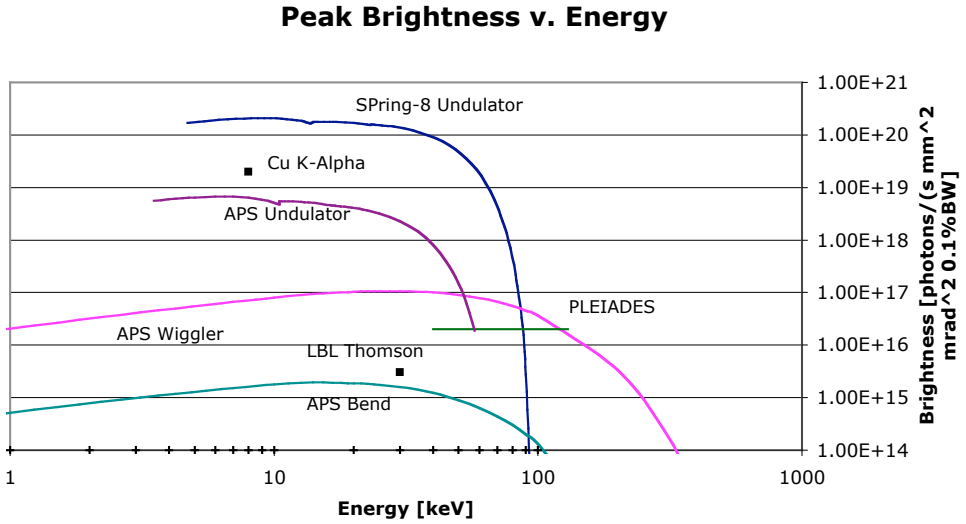

Figure 1 Peak brightness of several short x-ray pulse sources. Spring-8 and APS are synchrotron facilities, Cu K-alpha is a non-thermal laser plasma source, and PLEIADES and LBL Thomson are Thomson scattering based sources.

1.1.1 A Few Sources

The mostly widely known (and used) bright, hard x-ray source is the synchrotron. In a modern (or "third generation") synchrotron, electrons are circulated at energies up to a few GeV. The electron path consists of several straight sections of beamline connected with bending magnet systems, can generates basically three different types of radiation, as shown in Figure 1. Radiation with a broad, essentially fixed spectrum is produced in the bending magnet sections, a natural result of the centripetal acceleration of the electrons. In the straight section of beamline, a periodic magnetic structure is inserted (called, appropriately enough, in synchrotron parlance an "insertion device" – see Figure 7). This structure causes the electrons to oscillate, and thereby produce radiation. This radiation is generally beamlike, and, depending on the strength of the magnetic field applied, either relatively narrow in bandwidth and tunable (the "undulator" limit, when the transverse excursions of the electron remain within the emission cone of the radiation) or as broad as that of bending magnet radiation, though significantly brighter (the "wiggler" limit, when each oscillation of the electron radiates like a bending magnet))[12]. Quite a bit of ultrafast science has been done using this radiation, often coupled with an ultrafast laser[13-16].

Table I shows some typical synchrotron parameters. Synchrotron radiation usually has a pulse length on the order of a few tens to hundreds of picoseconds, the length of the electron bunch. However, a way to reduce this length has been proposed[17] and demonstrated[18] recently at Lawrence Berkeley National Laboratory (LBL). In this scheme, the electron bunch circulating in the synchrotron is made to interact with a high-intensity short-pulse laser inside a wiggler structure, causing a shift in energy of the part of the electron bunch that sees the laser pulse. This "slice" of the electron bunch is then spatially separated from the rest of the bunch in a bending magnet, and produces it's own radiation that is spectrally similar to that of a normal bunch, but much shorter in duration (typically 10s to 100s of fs). Although this helps overcome some of the limits in the pulse duration, it doesn't change the energies achievable in a synchrotron which, as can be seen in Figure 1, starts to fall off rapidly as you get past 100 keV.

A newer laser-driven source, and one of growing popularity, is what is generally referred to as a "K_{α} source" [20]. The name comes from the fact that the spectrum generated is that of the K_{α} line of the target material. These are systems in which an ultrashort pulse laser is focused onto a metal, creating a plasma. The intense laser field then accelerates the electrons in the plasma to energies up to 100 keV in back towards the metal, and when they interact they give off a bright flash of x-rays. The duration of this x-ray burst is similar to the duration of the laser pulse, and therefore can be as short as tens of femtoseconds. These pulses have allowed for numerous useful experiments[21-30]. The significant downside is the fixed energy of the x-ray pulse. Since the energy is defined by the K_{α} line of the target material (e.g. 8 keV for copper), changing the energy requires replacing the target material, which is generally not something that could be done

Table I — Sample synchrotron parameters[19]

	Electron Energy	Pulse Duration	Undulator Tuning Range
Advanced Light Source – ALS (California)	1.9 GeV	35-70 ps	0.23-1.8 keV
Advanced Photon Source - APS (Illinois)	7.0 GeV	100 ps	3.5-38 keV
European Synchrotron Radiation Facility – ESRF (France)	6.04 GeV	70 ps	2.6-22 keV
Spring-8 (Japan)	8.0 GeV	120 ps	4.7-51 keV

during the course of an experimental run.

A third source is an x-ray free electron laser, such as the proposed Linac Coherent Light Source (LCLS) to be built at the Stanford Linear Accelerator Center (SLAC) [31]. This system would produce light at a few keV that is 10 orders of magnitude brighter than current sources (expected brightness is ~10^{34} photons s^{-1} mm^{-2} $mrad^{-2}$ 0.1%BW^{-1}). The downside here is again the low energy limit, and the fact that it will be years before this source is operational (currently scheduled for 2009). Plus this source also suffers one of the other significant drawbacks of synchrotrons – the large-scale facility investments required limit the number of available sources.

1.1.2 Thomson Scattering

The fourth option is what is referred to as a "Thomson source". In this scheme, high-intensity laser light is scattered from relativistic electrons, and the Doppler shift induced in the scattered light transforms the laser photons into x-ray photons. This process is referred to in the literature variously as "Thomson scattering"[48], because that is typically the scattering process involved in the rest frame of the electron since the laser photon energy is below the rest-mass energy of the electron; "Compton scattering"[41] as a more general name when the Thomson condition isn't met; "Inverse Compton scattering"[59], due to the transfer of energy and momentum from the electron to the photon, the opposite of the effect Compton first observed; and "Laser Synchrotron Radiation" [37], due to the parallels between this source and synchrotron radiation that will be discussed in Section1.2.3.1. Because the physics of the source covered in this dissertation are based in the Thomson scattering limit, I will refer to this process as Thomson scattering throughout.

Thomson scattering from relativistic electrons was first studied in depth in the 1940s, when it was postulated as a slowing mechanism for intergalactic electrons[32]. It was not until the invention of the laser in the 1960s, however, that the first Compton sources were proposed[33,34] and demonstrated[35,36]. These experiments generated 4 photons shifted by only 259 Å, and eight 850 MeV photons per pulse, respectively.

After the initial demonstrations, interest in producing Compton sources waned due to the low brightness of the x-rays produced — a consequence of the low cross-section for Compton

scattering [σ_T = 6.65 x10^{-25} cm^2, see (21)]. In recent years, however, powerful lasers, photoinjectors, and high-quality accelerators have become commonplace, and the possibility of producing a high photon and relativistic electron densities, and consequently high x-ray fluxes, has renewed interest in the field. A variety of theoretical research into proposed sources was performs[37-39], and in 1996 the first subpicosecond hard x-ray source was demonstrated at Lawrence Berkeley National Laboratory[40]. This projected produced 5 × 10^4 photons with a peak energy of 30 keV. Similar results have been obtained by others (see Figure 9).

1.2 The Theory of Thomson-Scattering Based X-Ray Sources

Numerous articles studying the properties of Thomson scattering from a relativistic electron beam have been published[41-52], focusing on different aspects of both linear and non-linear Thomson scattering processes and taking various approaches. For the source we are interested in developing, only the linear theory is relevant; that is what I shall develop here (the meaning of "linear" in this context will be explained which the assumption is made). I'll begin with straightforward derivation of the key features of Thomson scattering using a single electron and a electromagnetic plane wave. Those results can then be applied to a "real" source, with an electron bunch of finite emittance and a laser beam of finite size and duration. I'll give a general overview of some of the nonlinear effects at the end.

1.2.1 An Ideal System

To introduce the main features of Thomson scattering, we'll start by assuming we have an infinite plane wave, polarized along the x axis, with frequency ω_{inc}:

$$\vec{E}\left(\vec{x},t\right) = E_0\hat{x}e^{i\left(\vec{k}_{inc}\cdot\vec{x}-\omega_{inc}t\right)}. \qquad (1)$$

This wave impinges upon an electron, traveling with speed v in the +z direction, at an angle of θ_{inc} relative to the electron's direction of motion. Since the plane wave is propagating in vacuum, the x-axis polarization (chosen here to be perpendicular to the electron's direction of motion) requires the laser wave vector , $\vec{k}_{inc}$, to lay in the y-z plane (i.e. k_x=0) because, via Maxwell,

$$\nabla\cdot\vec{E}=0 \Rightarrow \vec{k}_{inc}\cdot\hat{x}=0.$$

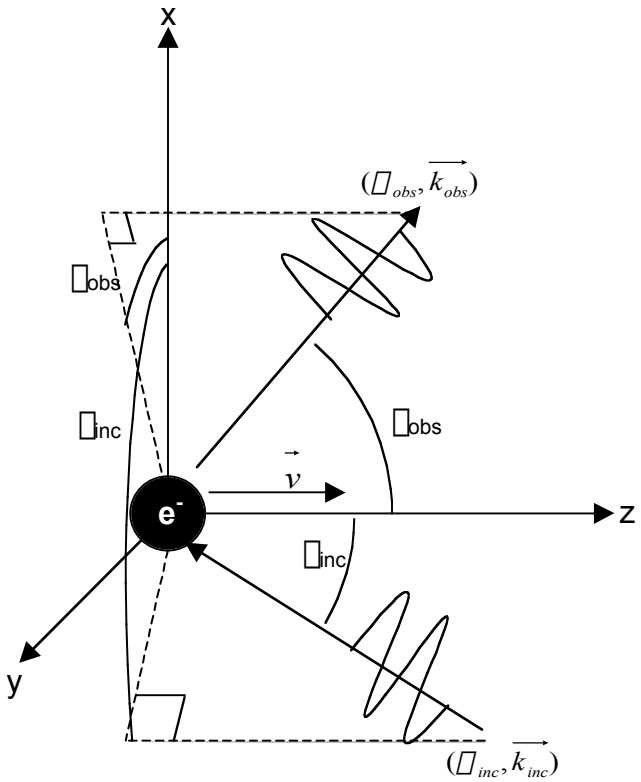

Figure 2 Simple Thomson scattering geometry for calculating the observed scattered radiation

A similar derivation to what follows, but for an arbitrary incoming polarization (and $\vec{k}_{inc}$), is presented in Ref. 53.

1.2.1.1 Scattered Photon Energy

We begin with the observed energy of the scattered radiation. Figure 2 shows the geometry we are considering: an electron with velocity $\vec{v} = v\hat{z}$, and a plane EM wave with frequency ω_{inc} incident upon it at an angle θ_{inc} from the +z axis. The scattered radiation will be observed at an angle θ_{obs}. The lab-frame wave 4-vectors for the incoming and observed radiation are

$$\mathbf{k}^{\mu}_{inc} = \left(\frac{\omega}{c}, \vec{k}_{inc}\right) = \left(\frac{\omega}{c}, k_{0,inc}\sin(\theta - \theta_{inc})\cos\phi_{inc}, k_{0,inc}\sin(\theta - \theta_{inc})\sin\phi_{inc}, k_{0,inc}\cos(\theta - \theta_{inc})\right)$$

$$= \left(\frac{\omega}{c}, k_{0,inc}\sin\theta_{inc}\cos\phi_{inc}, k_{0,inc}\sin\theta_{inc}\sin\phi_{inc}, -k_{0,inc}\cos\theta_{inc}\right)$$

$$\mathbf{k}^{\mu}_{obs} = \left(\frac{\omega}{c}, k_{0,obs}\sin\theta_{obs}\cos\phi_{obs}, k_{0,obs}\sin\theta_{obs}\sin\phi_{obs}, -k_{0,obs}\cos\theta_{obs}\right)$$

Transforming to a coordinate system co-moving with the electron with the Lorentz transformation

$$\mathbf{k}'_{inc} = \left(\frac{\omega'_{inc}}{c}, -k_x, k_y, k_z\right) = \left(\frac{\omega_{inc}}{c}, -\beta\gamma\right), \tag{2}$$

where

$$\gamma = \sqrt{\left(1-\beta^2\right)^{-1}}, \quad \beta = \frac{v}{c}, \quad k_0 = \left|\vec{k}\right|,$$

gives for the electron-frame wave vectors

$$\mathbf{k}'_{inc} = \left(\frac{\omega'_{inc}}{c} + \beta k_{0,inc}\cos\theta_{inc}, k_{0,inc}\sin\theta_{inc}\cos\phi_{inc}, k_{0,inc}\sin\theta_{inc}\sin\phi_{inc}, -k_{0,inc}\cos\theta_{inc} - \beta\frac{\omega_{inc}}{c}\right)$$
$$= \left(\frac{\omega'_{inc}}{c}, \vec{k}'_{inc}\right)$$

$$\mathbf{k}'_{obs} = \left(\frac{\omega'_{obs}}{c}, -k_{0,obs}\cos\theta_{obs}, k_{0,obs}k_{0,inc}\sin\theta_{obs}\cos\phi_{obs}, k_{0,obs}\sin\theta_{obs}\sin\phi_{obs}, k_{0,obs}\cos\theta_{obs} - \beta\frac{\omega_{obs}}{c}\right).$$

Assuming we are in the Thomson scattering limit, so the scattered frequency, ω'_{obs}, is equal to the incident frequency, ω'_{inc}, in this frame, we get

$$\frac{\omega'_{inc}}{c} = \frac{\omega'_{obs}}{c}$$
$$\left(\frac{\omega_{inc}}{c} + k_{0,inc}\cos\theta_{inc}\right) = \left(\frac{\omega_{obs}}{c} - \beta k_{0,obs}\cos\theta_{obs}\right).$$

Add to this the assumption that we are in vacuum, so

$$k_0 = \frac{\omega}{c},$$

and we have

$$\frac{\omega_{obs}}{c}\left(1-\beta\cos\theta_{obs}\right) = \frac{\omega_{inc}}{c}\left(1+\beta\cos\theta_{inc}\right)$$

$$\omega_{obs} = \omega_{inc}\frac{\left(1+\beta\cos\theta_{inc}\right)}{\left(1-\beta\cos\theta_{obs}\right)}. \tag{3}$$

The peak energy is observed when $\theta_{obs} = 0$. In the highly relativistic limit , where $\beta \to 1$ and

$$\gamma^2 = \frac{1}{1-\beta^2} = \frac{1}{(1-\beta)(1+\beta)} \to \frac{1}{2(1-\beta)}, \tag{4}$$

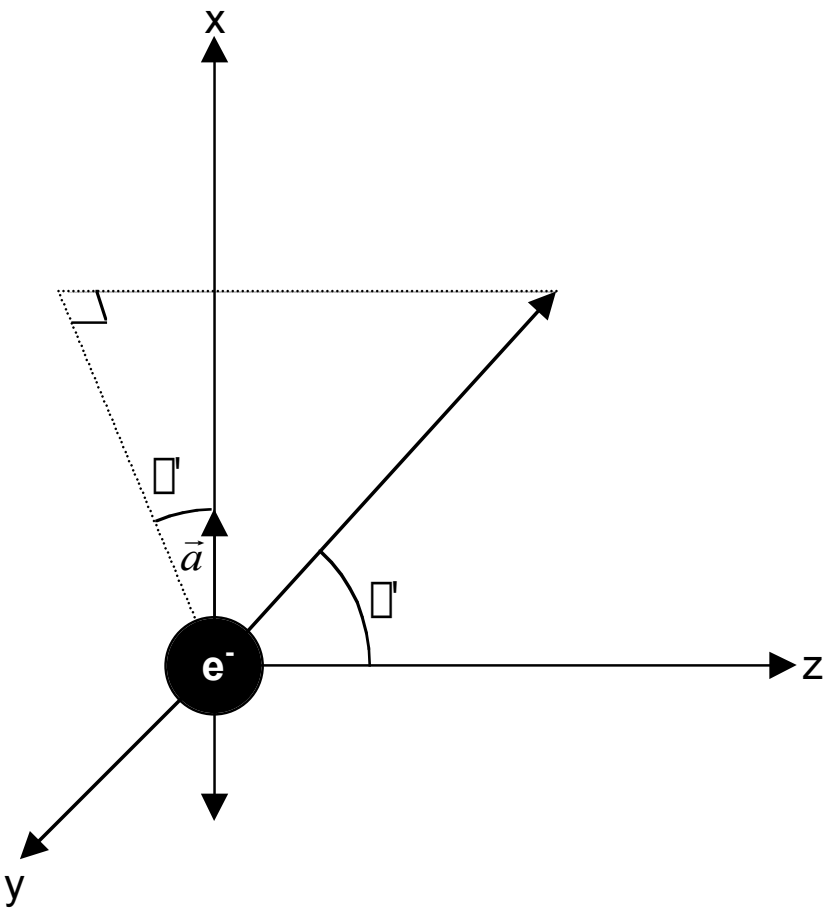

Figure 3 The geometry used for considering the Thomson radiation pattern. The electron is moving in the +z direction in the lab frame.

we have

$$\Box_{peak} = 2\Box^2\left(1+\Box\cos\Box_{inc}\right). \tag{5}$$

Equation 5 shows that even for an ideal electron, a broad spectrum of radiation is produced, although the frequency has a perfect correlation with observation angle. This will not be true once we have multiple electrons and a non-plane-wave laser pulse, as will be discussed in section 1.2.2. Also, note that the angle $\Box$ does not appear in this equation. This result does not depend on the laser polarization, and therefore is true for arbitrary laser polarization and $\vec{k}_{inc}$, including polarizations not perpendicular to *z*.

1.2.1.2 Scattered Radiation Pattern

The next significant feature of Thomson scattering is the radiation pattern produced. Figure 3 shows the geometry under consideration in a frame moving with the average velocity of the electron. θ is the polar angle with respect to the *z*-axis, and ϕ is the azimuthal angle in the *x*-*y* plane. A laser polarized along the *x* axis drives the electron at frequency ω', causing an acceleration in *x* of $\vec{v} = \dot{v}c\hat{x}$. The total power radiated per unit solid angle is given by[54]

$$\frac{dP}{d\Omega} = \frac{e^2}{4\pi c}\left|\hat{n}\times\left(\hat{n}\times\vec{\beta}\right)\right|^2 \tag{6}$$

where $\hat{n}$ is a unit vector in the direction of observation, defined by

$$\hat{n} = \sin\theta\cos\phi\hat{x} + \sin\theta\sin\phi\hat{y} + \cos\theta\hat{z}. \tag{7}$$

As long as the acceleration is along the x-axis, $\dot{\vec{\beta}} = \dot{\beta}\hat{x}$ (this is the linear assumption), (6) and (7) give

$$\frac{dP}{d\Omega} = \frac{e^2\left|\dot{\beta}\right|^2}{4\pi c}\left(1-\sin^2\theta\cos^2\phi\right). \tag{8}$$

This is the standard $\sin^2$ dipole radiation pattern shown in Figure 4, albeit in a non-standard coordinate system (if the acceleration is taken to be $\vec{v} = \dot{v}c\hat{z}$, the $\sin^2$ result appears). Because the energy of all the photons emitted in this frame is the same, the power emitted per unit solid angle is directly proportional to the number of photons emitted per solid angle:

$$\frac{dP}{d\Omega}\propto\frac{dN}{d\Omega} = A\left(1-\sin^2\theta\cos^2\phi\right). \tag{9}$$

We will come back to determine the magnitude of the value *A* in the next section.

This result must now be transformed to the lab frame. The angle θ' can be defined by[55]

$$\cos\theta' = \frac{k_z'}{k_0'} = \frac{k_z'c}{\omega'}.$$

Using the Lorentz transform relationships from (2), we get

$$\cos\theta = \frac{\gamma\left(k_z - \frac{\omega}{c}\beta\right)c}{\gamma\left(\omega - \beta ck_z\right)} = \frac{\gamma\left(k_0\cos\theta - \beta k_0\right)c}{\gamma\left(k_0c - \beta ck_0\cos\theta\right)} = \frac{\cos\theta-\beta}{1-\beta\cos\theta}. \tag{10}$$

The same process with k_y', instead of k_z', gives

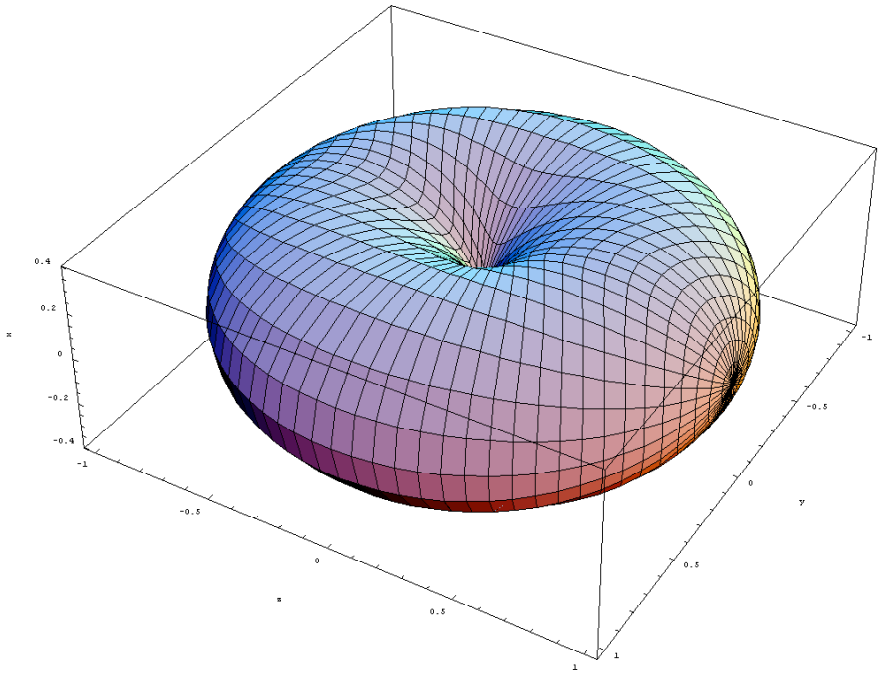

Figure 4 Radiation pattern from an oscillating electron with no average velocity (β=1)

$$\sin\theta' = \frac{k_y' c}{\omega'} = \frac{k_y c}{\omega(1-\beta k_z)} = \frac{ck_0 \sin\theta}{\omega(k_0 c - \beta c k_0 \cos\theta)} = \frac{\sin\theta}{\gamma(1-\beta\cos\theta)}. \quad (11)$$

The converse relations result from swapping primed and unprimed coordinates and changing the sign of β:

$$\sin\theta = \frac{\sin\theta'}{\gamma(1+\beta\cos\theta')}, \text{ and} \quad (12)$$

$$\cos\theta = \frac{\cos\theta' + \beta}{1+\beta\cos\theta'}. \quad (13)$$

The azimuthal angle ϕ=ϕ' doesn't change upon transformation, as can be demonstrated by following the same procedure with k_x' and k_y'.

We can now plug (10) and (11) into (9):

$$\frac{d\Omega'}{d\Omega} = A\left[1 - \frac{\sin^2\theta\cos^2\theta}{\gamma^2(1-\beta\cos\theta)^2}\right]$$

The number of photons is invariant – it is a counting operation. This leaves the $d\Omega'$ term to deal with:

$$\frac{d\sigma}{d\cos\theta} = \frac{d\sigma}{d\theta}\frac{d\theta}{d\cos\theta} = \frac{d\sigma}{d\theta}\frac{\sin\theta\, d\theta\, d\phi}{\sin\theta\, d\cos\theta\, d\phi} = \frac{d\sigma}{d\theta}\frac{d(-\cos\theta)d\phi}{d(-\cos\theta)d\phi}.$$

Using $d\sigma = d\sigma$ (because $\sigma = \sigma$), and differentiating (10) with respect to $\cos\theta$, gives

$$\frac{d\sigma}{d\theta} = \frac{d\cos\theta}{d\cos\theta} = \frac{1-\beta^2}{\left(1-\beta\cos\theta\right)^2},$$

gives us

$$\frac{d\sigma}{d\cos\theta} = \frac{d\sigma}{d\theta}\left[\frac{1-\beta^2}{\left(1-\beta\cos\theta\right)^2}\right]^{-1}$$

and therefore

$$\frac{d\sigma}{d\theta} = \frac{A\left(1-\beta^2\right)}{\left(1-\beta\cos\theta\right)^2}\left[1-\frac{\sin^2\theta\cos^2\theta}{\beta^2\left(1-\beta\cos\theta\right)^2}\right] \tag{14}$$

or, if the total energy per unit solid angle is desired, we can simply multiply by the photon energy:

$$\frac{dU}{d\theta} = \frac{A\left(1-\beta^2\right)\hbar\omega_{obs}}{\left(1-\beta\cos\theta\right)^2}\left[1-\frac{\sin^2\theta\cos^2\theta}{\beta^2\left(1-\beta\cos\theta\right)^2}\right]$$

$$= \frac{A\hbar\omega_{inc}\left(1+\beta\cos\theta_{inc}\right)}{\left(1-\beta\cos\theta\right)^2}\frac{\left(1-\beta^2\right)}{\left(1-\beta\cos\theta\right)}\left[1-\frac{\sin^2\theta\cos^2\theta}{\beta^2\left(1-\beta\cos\theta\right)^2}\right]$$

$$\frac{dU}{d\theta} = \frac{A\hbar\omega_{inc}\left(1+\beta\cos\theta_{inc}\right)}{\beta^2\left(1-\beta\cos\theta\right)^3}\left[1-\frac{\sin^2\theta}{\beta^2\left(1-\beta\cos\theta\right)^2}\cos^2\theta\right]. \tag{15}$$

This function is plotted in Figure 5 for several electron energies. The most significant factor at large θ is the $\left(1-\beta\cos\theta\right)^{-3}$ term, which dominates the equation and leaves the radiation directed in a tightly focused forward cone. The null of the radiation, at $\theta=\pi/2$,gives $\cos\theta = \beta$. In the highly relativistic limit, where $\beta \to 1$, $\cos\theta \to 1$ and we can make the small –angle approximations

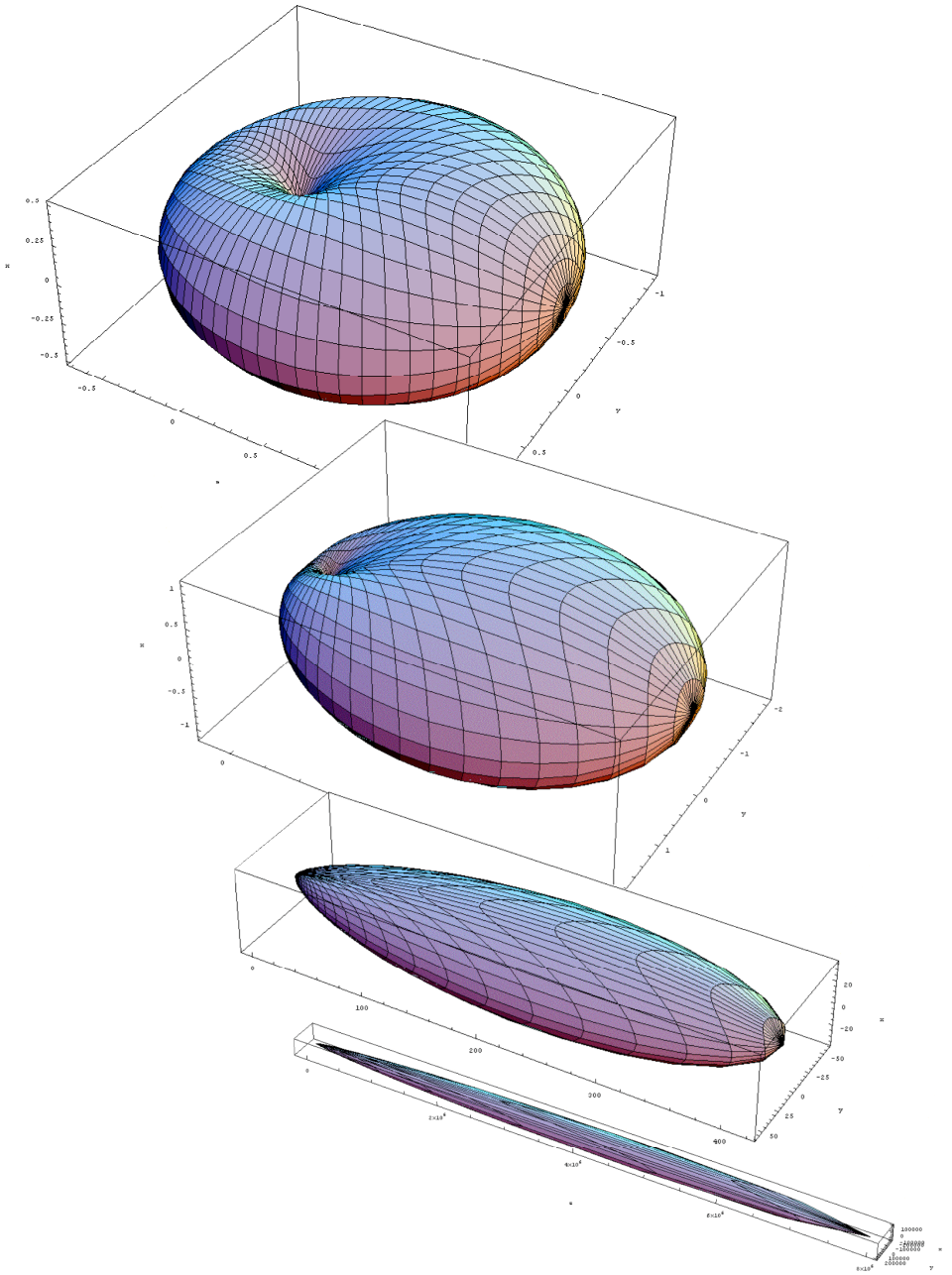

Figure 5 Radiation patterns for assorted electron velocities. From top to bottom: β = 1.01, 1.1, 2, 10

$$\cos\theta \approx 1 - \frac{\theta^2}{2}$$

$$\sin\theta \approx \theta$$

which gives us

$$1 - \frac{\theta^2}{2} = \beta \quad 2(1-\beta) = \theta^2 = \frac{1}{\gamma^2}$$

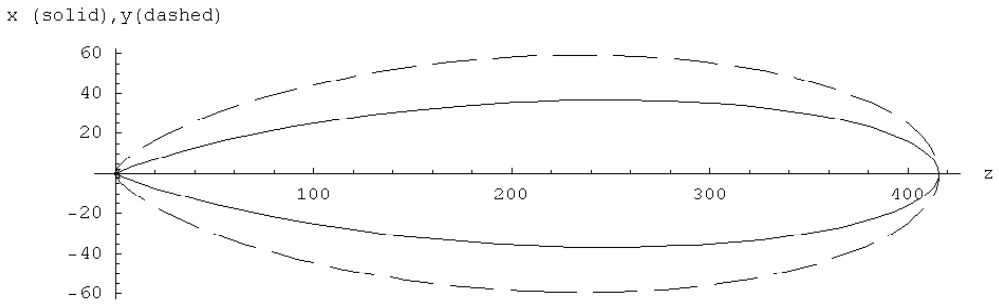

Figure 6 The radiation pattern in the *x*-*z* (solid) and *y*-*z* (dashed) planes for an electron oscillating along the *x* axis. β=2.

where we have made use of (4). This gives a good number for the size of the emission cone. Since only small angles are relevant, we can use the small angle approximation and (4) to get

$$1-\beta\cos\theta \approx 1-\beta+\beta\frac{\theta^2}{2} = \frac{1}{2\gamma^2}+\frac{\beta\theta^2}{2} = \frac{1+\gamma^2\beta\theta^2}{2\gamma^2}, \tag{16}$$

making (15), in the highly relativistic limit,

$$\frac{dU}{d\Omega} = \frac{8A\hbar\omega_{inc}\left(1+\beta\cos\theta_{inc}\right)\beta^4}{\left(1+\gamma^2\beta^2\theta^2\right)^3}\left[1-\frac{4\gamma^2\beta^2}{\left(1+\gamma^2\beta^2\theta^2\right)^2}\cos^2\phi\right] \tag{17}$$

The other important effect to notice is the variation in the radiated power with β. If you observe the radiation in the plane of polarization, the intensity drops off with β faster than if you look in the plane perpendicular to the polarization. This leads to a slightly oblong radiation profile, with the beam elongated along the axis perpendicular to the polarization. This effect is illustrated in Figure 6.

1.2.1.3 Scattered Amplitude

The last step for our idealized source is to determine the value of *A*. Recall from (8) that

$$\frac{dP}{d\Omega} = \frac{e^2\left|\dot{\beta}\right|^2}{4\pi c}\left(1-\sin^2\theta\cos^2\phi\right).$$

We therefore need to determine $\dot{\beta}$. Starting with (1)

$$\vec{E}\left(\vec{x},t\right) = E_0\hat{x}e^{i\left(\vec{k}_{inc}\cdot\vec{x}-\omega_{inc}t\right)}, \tag{1}$$

we can use the Lorentz force equation

$$\vec{F} = m\dot{\vec{v}} = q\vec{E} + \frac{q\vec{v}}{c} \times \vec{B}$$

to find $\dot{\beta}$. If we assume $|\vec{v}| << c$, we have

$$\vec{v} = \frac{e}{m_e} E_0 e^{i(\vec{k}\cdot\vec{x} - \omega t)} \hat{x}. \tag{18}$$

Integrating this with respect to time,

$$\vec{v} = \int \dot{\vec{v}} dt = \int \frac{e}{m_e} E_0 e^{i(\vec{k}\cdot\vec{x} - \omega t)} \hat{x} = \frac{eE_0}{-i\omega m_e} e^{i(\vec{k}\cdot\vec{x} - \omega t)} \hat{x}.$$

The peak magnitude $v_{peak} = eE_0 / m\omega$ must be much less than c to satisfy our assumption in deriving (18), so

$$a_0 \equiv \frac{eE_0}{mc\omega} << 1 \tag{19}$$

a_0 is called the "normalized vector potential" of the laser, and a_0^2 is directly proportional to the photon density. This restriction defines the "linear" regime in Thomson scattering – the regime relevant for the source we are developing.

The power incident upon the electron is given by the time averaged Poynting vector of the incoming plane wave[54]:

$$\langle \vec{S} \rangle = \frac{1}{2} \left\langle \frac{c}{4\pi} \vec{E} \times \vec{B} \right\rangle = \frac{c}{8\pi} |E_0|^2.$$

We can therefore take the time-averaged value of $|\dot{\beta}|^2$,

$$\left\langle |\dot{\beta}|^2 \right\rangle = \left\langle \frac{|\dot{\vec{v}}|^2}{c^2} \right\rangle = \left(\frac{e|E_0|}{m_e c} \right)^2 \left\langle \left| e^{i(\vec{k}\cdot\vec{x} - \omega t)} \right|^2 \right\rangle = \frac{1}{2} \left(\frac{e|E_0|}{m_e c} \right)^2,$$

plug it in to (8), and divide by the total incident power to get the cross section

$$\frac{d\sigma}{d\Omega} = \frac{1}{P_{inc}} \frac{dP}{d\Omega} = \underbrace{\left(\frac{e^2}{m_e c^2} \right)^2}_{=A} \left(1 - \sin^2\theta \cos^2\phi \right). \tag{20}$$

Integrating this over all solid angles yields:

$$\sigma = \frac{8\pi}{3}\left(\frac{e^2}{m_e c^2}\right)^2 = \frac{8\pi}{3} r_e^2 = \sigma_T = 6.652 \times 10^{-25}\ \text{cm}^2, \tag{21}$$

the Thomson cross section. r_e is known as the "classical electron radius". Now that we know $A = r_e^2$, we can write at last the full relativistic differential Thomson cross section:

$$\frac{d\sigma}{d\Omega} = \frac{r_e^2}{\gamma^2\left(1-\beta\cos\theta\right)^2}\left[1 - \frac{\sin^2\theta\cos^2\phi}{\gamma^2\left(1-\beta\cos\theta\right)^2}\right] \tag{22}$$

Or, in the large γ/small θ limit,

$$\frac{dU}{d\Omega} = \frac{4r_e^2\gamma^2}{\left(1+\gamma^2\theta^2\right)^2}\left[1 - \frac{4\gamma^2\theta^2}{\left(1+\gamma^2\theta^2\right)^2}\cos^2\phi\right] \tag{23}$$

1.2.2 A Real Source

While the previous section fully described Thomson scattering with an infinite plane wave and a single electron, a real Thomson source will involve an electron bunch containing >10^9 electrons and a tightly focused laser beam. Due to the incoherent nature of the Thomson scattering process[56], this real source can be modeled using a distribution of infinite plane waves that add up to form a real laser beam, and a distribution of electrons to form a real electron bunch. Although in the idealized source in the previous section there was a one-to-one correspondence between observation angle and observed energy, a real source, with the different electrons and plane waves added up, will yield significant spectral broadening at a given observation angle.

1.2.2.1 Laser Effects

Because of the low cross-section for Thomson scattering, it is crucial to get the photon and electron densities to be as large as possible (within the limits of the linearity requirement on a_0). Furthermore, the duration of the Thomson x-ray pulse is correlated with the duration of the electron and/or laser pulses, depending on the interaction geometry. This means that for short x-ray pulses, either short laser pulses or short electron bunches are required. Once one of the two is short it is, in general, no great benefit to having the other be much longer, as the photons or

electrons outside the temporal interaction window won't contribute to the x-ray flux. These two requirements on intensity and pulse duration lead to the decision to use an ultrashort (<ps) laser system for photon production.

Of course, an ultrashort pulse laser is not monochromatic, as was assumed in deriving the Thomson equations above. If we want a pulse with a $1/e^2$ intensity duration of $2\Delta t$, we need to sum up infinite plane waves of different frequencies in such a way that

$$E(\vec{x},t) = E_0(\vec{x})e^{\frac{t^2}{\Delta t^2}}e^{i(\vec{k}\cdot\vec{x}-\omega_c t)} = \int A(\omega)e^{i(\vec{k}\cdot\vec{x}-(\omega_c-\omega)t)}d\omega$$
$$= E_0(\vec{x})e^{\frac{t^2}{\Delta t^2}} = \int A(\omega)e^{i\omega t}d\omega$$

This is simply a Fourier transform relationship, so[57]

$$A(\omega) = \frac{1}{2\pi}E_0(\vec{x})\int e^{\frac{t^2}{\Delta t^2}}e^{-i\omega t}d\omega$$
$$= \frac{\Delta t}{2\sqrt{\pi}}E_0(\vec{x})e^{\frac{\omega^2\Delta t^2}{4}} = \frac{1}{\Delta\omega\sqrt{\pi}}E_0(\vec{x})e^{-\frac{\omega^2}{\Delta\omega^2}},$$

with $\Delta\omega = \frac{2}{\Delta t}$. Because of this relation, a Gaussian pulse always has

$$\Delta t\,\Delta\omega \geq 2,$$

where both widths are $1/e^2$ half-widths of the intensity distributions. From (3), in the high-γ limit using (16),

$$\omega_{obs} = \omega_{inc}\frac{2\gamma^2}{1+\gamma^2\theta_{obs}^2}\left(1+\beta\cos\theta_{inc}\right) \tag{24}$$

or $\omega_{obs} \propto \omega_{in}$, so the relative bandwidth of Thomson scattered energy observed as a result of the finite pulse width is the same as that of the laser:

$$\frac{1}{\omega_{obs}}\frac{\partial\omega_{obs}}{\partial\omega_{inc}} = \frac{1}{\omega_{inc}}\Rightarrow\ \frac{\Delta\omega_{obs}}{\omega_{obs}} = \frac{\Delta\omega}{\omega}. \tag{25}$$

Similarly, to maximize the intensity, the laser is tightly focused. Adding up plane waves, this time with differing $\vec{k}$, and using a coordinate system where the average laser direction is along the *z* axis, we can get

$$E(\vec{x},t) = E_0(t)e^{-\left(\frac{x^2}{\sigma_{x_f}^2}+\frac{y^2}{\sigma_{y_f}^2}\right)}e^{i(k_z z-\omega t)} = \iint A(k_x,k_y)e^{i(\vec{k}\cdot\vec{x}-\omega t)}dk_x dk_y.$$

Again, this is a Fourier transform, so

$$A(k_x,k_y)=\frac{1}{2\pi}\iint E_0(t)e^{-\left(\frac{x^2}{\sigma_{x_l}^2}+\frac{y^2}{\sigma_{y_l}^2}\right)}e^{-i(k_x x+k_y y)}dxdy$$

$$=\frac{\sigma_{x_l}\sigma_{y_l}}{4\pi}E_0(t)e^{-\left(\frac{k_x^2\sigma_{x_l}^2}{4}+\frac{k_y^2\sigma_{y_l}^2}{4}\right)}=\frac{1}{\sigma_{k_x}\sigma_{k_y}}E_0(t)e^{-\left(\frac{k_x^2}{\sigma_{k_x}^2}+\frac{k_y^2}{\sigma_{k_y}^2}\right)}$$

with $\sigma_{k_{x,y}}=\frac{2}{\sigma(x_l,y_l)}$ and therefore

$$\sigma_{k_x}\sigma_{x_l}\geq 2,\quad \sigma_{k_y}\sigma_{y_l}\geq 2.$$

Converting this into angles,

$$\sin\sigma\theta_l\approx\sigma\theta_l=\frac{\sigma k}{k_0}.$$

Note that for $\sigma x>1$ μm and 800 nm laser light,

$$\frac{\sigma k_x}{k_0}<\frac{\frac{2}{\sigma x_l}}{\frac{2\pi}{\lambda_0}}=0.25,$$

assuming an ideal focus, so the small angle approximation is valid. We therefore have

$$\sigma\theta_{lx}\sigma x_l\geq\frac{\lambda_0}{\pi},\quad \sigma\theta_{ly}\sigma y_l\geq\frac{\lambda_0}{\pi}.$$

This angle spread on the laser varies the incoming incidence angle θ_{inc}. Taking (24), we get

$$\frac{1}{\omega_{obs}}\frac{\partial\omega_{obs}}{\partial\theta_{inc}}=\frac{\omega_{inc}\frac{2\beta^2}{1+\beta^2\omega_{obs}^2}\left(-\sin\theta_{inc}\right)}{\omega_{inc}\frac{2\beta^2}{1+\beta^2\omega_{obs}^2}\left(1+\cos\theta_{inc}\right)}=\frac{-\beta\sin\theta_{inc}}{1+\beta\cos\theta_{inc}}\Rightarrow\frac{\sigma\omega_{obs}}{\omega_{obs}}=\frac{\beta\sin\theta_{inc}}{1+\beta\cos\theta_{inc}}\sigma\theta_{inc}.$$

We can see that the bandwidth for a head on collision (θ_{inc}=0°) is

$$\omega_{obs}=\omega_{inc}\frac{2\beta^2}{1+\beta^2\omega^2}\left(1+\cos\sigma\theta_l\right)\approx A\left(1+1-\frac{\sigma\theta_l^2}{2}\right)$$

$$\frac{\sigma\omega_{obs}}{\omega_{obs}}=\frac{A\left(2-\frac{\sigma\theta_l^2}{2}\right)-A(2)}{A(2)}=-\frac{\sigma\theta^2}{4}\qquad(26)$$

while for a side-on collision (θ_{inc}=90°) it's

$$\omega_{obs} = \omega_{inc}\frac{2\gamma^2}{1+\gamma^2\theta^2}\left[1+\cos\left(90+\theta_l\right)\right] = A[1-\sin\theta_l] \approx A\left(1-\theta_l\right)$$

$$\frac{\Delta\omega_{obs}}{\omega_{obs}} = \frac{A\left(1-\Delta\theta_l\right)-A\left(1\right)}{A(1)} = -\Delta\theta_l \tag{27}$$

1.2.2.2 Electron Effects

Naturally, the same two effects from the laser beam, energy spread and divergence angle, are present in the electron beam as well. Here, the limits on the beam performance are usually not dominated by physical limits like diffraction but by limits on the engineering of the e-beam system. Instead of calculating a spectral width or wave-vector spread, the electron beam energy spread and *emittance* are simply measured. For an energy spread in the electron beam of $\Delta\gamma$ in the high-γ limit,

$$\frac{1}{\omega_{obs}}\frac{\partial\omega_{obs}}{\partial\gamma}\Delta\gamma \quad \frac{\Delta\omega_{obs}}{\omega_{obs}} = \frac{2}{1+\gamma^2\theta_{obs}^2}\frac{\Delta\gamma}{\gamma}.$$

I will discuss in Chapter 3 the concept of emittance more fully, but for this analysis it is sufficient to note that

$$\Delta\theta_{ex} = \frac{\varepsilon_x}{\Delta x_e}, \quad \Delta\theta_{ey} = \frac{\varepsilon_y}{\Delta y_e}$$

where the widths are rms quantities. The electron angle, unlike the laser angle, affects both the angle of incidence of the laser *and* the observation angle, since it is defined relative to the propagation direction of the electrons. The effect on the incident angle is the same as for the laser, given by (26). The effect on the observation angle is given by

$$\frac{1}{\omega_{obs}}\frac{\partial\omega_{obs}}{\partial\theta_{obs}}\Delta\theta \quad \frac{\Delta\omega_{obs}}{\omega_{obs}} = \frac{2\gamma^2\theta_{obs}}{1+\gamma^2\theta_{obs}^2}\Delta\theta_e,$$

which scales with γ^2, and therefore dominates the effect produced by the incidence angle variation.

1.2.2.3 Sample Beam

To summarize, (24) is shown indicating which components are affected by which broadening effects:

$$\omega_{obs} = \overbrace{\omega_{inc}}^{\text{Laser Bandwidth}} \frac{2\overbrace{\sigma^2}^{\text{Electron Energy Spread}}}{(1+\underbrace{\sigma^2}_{\text{Electron Energy Spread}}\underbrace{\sigma_{obs}^2}_{\text{Electron Emittance}})}(1+\overbrace{\cos\theta_{inc}}^{\text{Laser Focus}}).$$

If we assume a source such as the one we have developed, using the various parameters shown in Table II we can find for the different contributions:

Laser bandwidth:

$$\frac{\Delta\omega_{obs}}{\omega_{obs}} = \frac{\Delta\omega}{\omega} = \frac{2}{\frac{85}{2}\,fs}\frac{820\,nm}{2\pi c} = 2\%$$

Laser focus:

$$\frac{\Delta\omega_{obs}}{\omega_{obs}} = \frac{\Delta\omega_l^2}{4} = \frac{1}{4}\left(\frac{820\,nm}{20\,\mu m}\right)^2 = 0.004\%$$

Electron energy spread:

$$\frac{\Delta\omega_{obs}}{\omega_{obs}} = \frac{2}{1+\sigma^2\sigma_{obs}^2}\frac{\Delta\gamma}{\gamma} = 2\cdot 0.002 = 0.4\%$$

Electron divergence:

$$\frac{\Delta\omega_{obs}}{\omega_{obs}} = \frac{2\sigma^2\sigma_e}{1+\sigma^2\sigma_e^2}\Delta\sigma_e = \frac{2\cdot 100^2\left(5\,mm\,mrad\cdot\frac{rad}{1000\,mrad}\right)^2}{1+100^2\left(\frac{5\,mm\,mrad\cdot\frac{rad}{1000\,mrad}}{100\cdot 0.99995\cdot 20\,\mu m}\right)^2} = 11.7\%$$

Table II —Sample source parameters used to estimate the relative contributions of various broadening effects

Interaction angle - θ_{inc}	0°
Laser wavelength - λ_0	820 nm
Laser pulsewidth - $2\sigma_t$	85 fs
Laser focal spot - $\sigma_{x_l}, \sigma_{y_l}$	20 μm
Electron energy - γ	100
Electron energy spread – $\Delta\gamma/\gamma$	0.002
Electron spot size - $\sigma_{x_e}, \sigma_{y_e}$	20 μm
Electron emittance - $\varepsilon_x, \varepsilon_y$	5 mm mrad

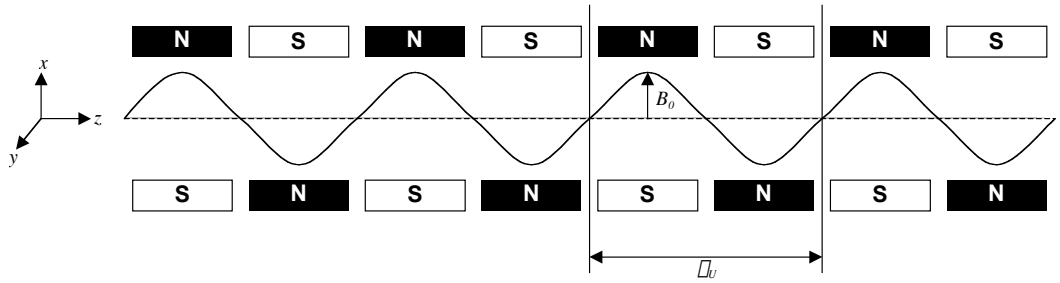

Figure 7 Undulator geometry.

It's clear that the electron emittance is the dominant effect in a source with these parameters. This demonstrates the importance of having a high-quality electron beam.

1.2.3 Nonlinear Scattering

Although only linear Thomson scattering will be performed with the source we are developing, it is worth briefly exploring some of the nonlinear effects that can be observed. A full derivation is not intended, merely a general overview. Detailed theories are presented elsewhere[43,45-48]. The applicability of these effects will be discussed in Chapter 5, where a future path is laid out.

There are two somewhat different nonlinear effects. The first manifests itself as a reduction in scattered x-ray energy as a function of laser intensity, which will be shown to parallel "K" tuning in synchrotron undulators. The second is the generation of harmonics of the radiation as the laser intensity rises. This effect is seen at intensities higher than those of the first effect. Both of these are directly related to the magnitude of a_0, defined in (19).

1.2.3.1 Energy Depression

This effect is best seen by starting with a synchrotron undulator. An undulator is a magnetic device used to produce x-ray radiation from electron beams. It consists (Figure 7) of alternating pairs of magnetic poles, with a period of λ_u and peak field B_0. An electron traveling with velocity v along the z axis sees the B-field along the x axis, and so feels a force $\vec{F} = e\vec{v} \times \vec{B} = evB(z)\hat{y}$, which causes it to oscillate, and therefore radiate.

The undulator creates a field in the lab frame of

$$\vec{B} = B_0 \cos\frac{2\pi z}{\lambda_u}\hat{x}. \tag{28}$$

To find the field in the electron frame, we have to transform the fields and the undulator length using[54]

$$\begin{aligned}
\vec{E}' &= \gamma\left(\vec{E} + \vec{\beta}\times\vec{B}\right) - \frac{\gamma^2}{\gamma+1}\vec{\beta}\left(\vec{\beta}\cdot\vec{E}\right) \\
\vec{B}' &= \gamma\left(\vec{B} - \vec{\beta}\times\vec{E}\right) - \frac{\gamma^2}{\gamma+1}\vec{\beta}\left(\vec{\beta}\cdot\vec{B}\right). \\
z' &= \gamma\left(z - \beta ct\right)
\end{aligned} \tag{29}$$

Plugging (28) into (29) gives

$$\begin{aligned}
\vec{E}' &= \tilde{B}\hat{y} \\
\vec{B}' &= \tilde{B}\hat{x} \\
\tilde{B} &= B_0 \cos\left[\underbrace{\frac{2\pi\gamma}{\lambda_u}}_{k_u}\left(z - vt\right)\right]
\end{aligned}.$$

As $v \to c$, $\gamma \to 1$ and the undulator field starts to look like a plane wave, with frequency $\omega_u = k_u c = \frac{2\pi c}{\lambda_u}$ and amplitude $E_0 = cB_0$. If we plug this into the definition of a_0 (19), we get

$$a_0 = \frac{eB_0}{mc\left(\frac{2\pi c}{\lambda_u}\right)} = \frac{eB_0\lambda_u}{2\pi mc^2} = K,$$

which is the undulator deflection parameter[12]. This means that for large γ, Thomson scattering and undulator radiation are nearly identical, and many of the well known undulator equations can be used to describe Thomson scattering, with K replaced by a_0. Most useful is the "Undulator equation"[55]:

$$\lambda = \frac{\lambda_u}{2\gamma^2}\left(1 + \frac{K^2}{2} + \gamma^2\theta^2\right),$$

or, in Thomson scattering form,

$$\omega_{obs} = \omega_{inc}\frac{2\gamma^2(1+\beta\cos\theta_{inc})}{1 + \frac{a_0^2}{2} + \gamma^2\theta^2},$$

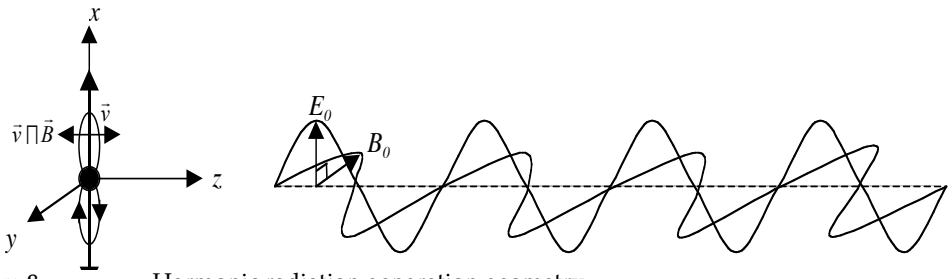

Figure 8 Harmonic radiation generation geometry.

where the cos θ_{inc} term has been added to account for non-head-on collisions. This is equation is the same as (3), with the exception of the extra $\frac{a_0^2}{2}$ term. As the laser intensity increases, the observed scattered photon energy starts to drop. This can be thought of as a reduced effective θ that results from some of the electrons momentum being shifted from the z axis to the x axis as it oscillates, resulting in a slightly smaller θ_z.

1.2.3.2 Harmonic Generation

The second nonlinear effect is harmonic generation. Recall that in (18), the equation for $\vec{v}$ was derived by assuming $v<<c$, and ignoring the $\frac{q\vec{v}}{c}\times\vec{B}$ term. When $a_0>1$ however, this term is no longer negligible because $v||c$. As the electron moves along the x axis relativistically, the magnetic field starts to push it along the z axis. The velocity changes direction 90° out of phase with the E and B fields (recall that the amplitude in (18) was imaginary), so during one period the direction of the force will change 4 times, and the electron, in the frame co-moving with the average electron velocity, will execute a "figure-8" pattern, as shown in Figure 8.

There is therefore an oscillation in the z direction at a frequency of $2\theta'$, which will produce dipole radiation at that frequency. As the laser becomes even more intense, this z-axis motion becomes relativistic as well, and interacts with the B field to add a further oscillation in the x direction, at $3\theta'$. As the laser intensity grows, this process continues, creating higher and higher harmonics.

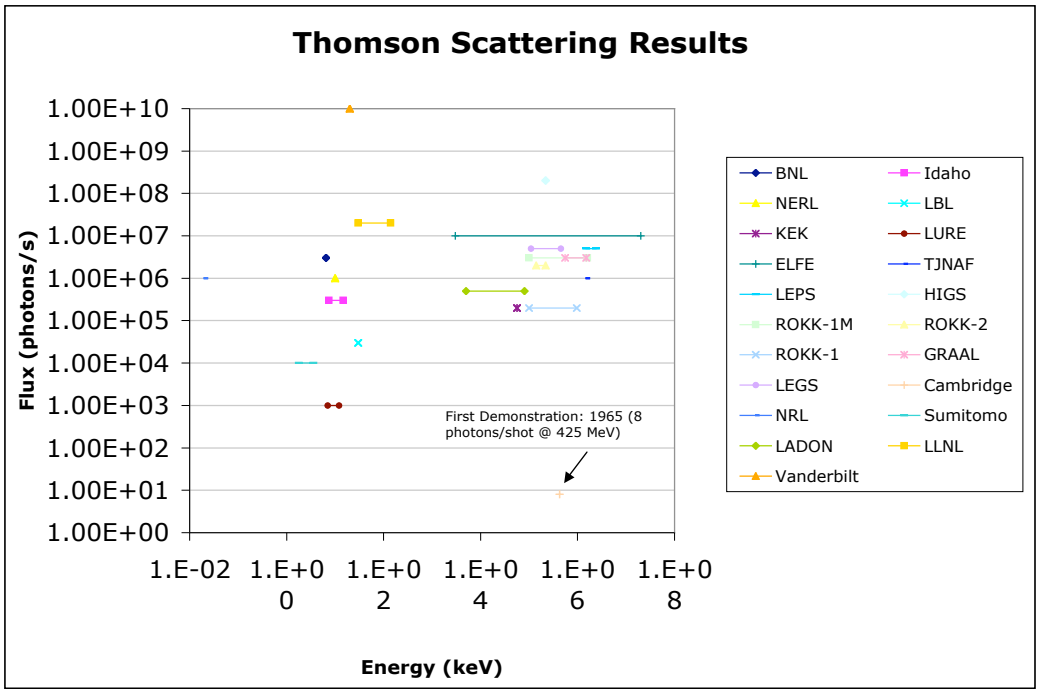

Figure 9 Summary of reported observations of Thomson scattering from relativistic electron beams, showing results from LURE[58], KEK[59], LBL[40], NERL[60], Idaho[61], BNL[62], Cambridge[36], NRL[63], Sumitomo[64], LLNL, Vanderbilt[65], and several γ-ray sources[66].

1.3 The PLEIADES System

Thomson scattering has been successfully observed at a number of sites around the world, as Figure 9 shows. It is interesting to note that several sources have been operated at very high (greater than 1 MeV) energies, and a few have been built at lower (<50 keV) energies, but none between 50 keV and 1 MeV. This region of the spectrum is interesting because, for example, the K-edges of most heavy metals lie in this region, e.g. tantalum (67.5 keV), gold (80.7 keV), bismuth (90.54 keV), and uranium (115.0 keV). Also, this part of the spectrum is higher than most synchrotrons are easily able to produce, so there aren't as many alternative sources. For these reasons we decided to build a Thomson source targeting x-ray production in this regime. This source is called PLEIADES, which stands for Picosecond Laser-Electron InterAction for the Dynamic Evaluation of Structures. The goal is to produce ultrashort (100s of fs to a few ps), high brightness (10^{18} photons/mm^2/s/mrad^2/0.1% BW) x-ray pulses with tunable photon energies from 20-200 keV for single-shot diffraction and radiography experiments in high-Z materials.

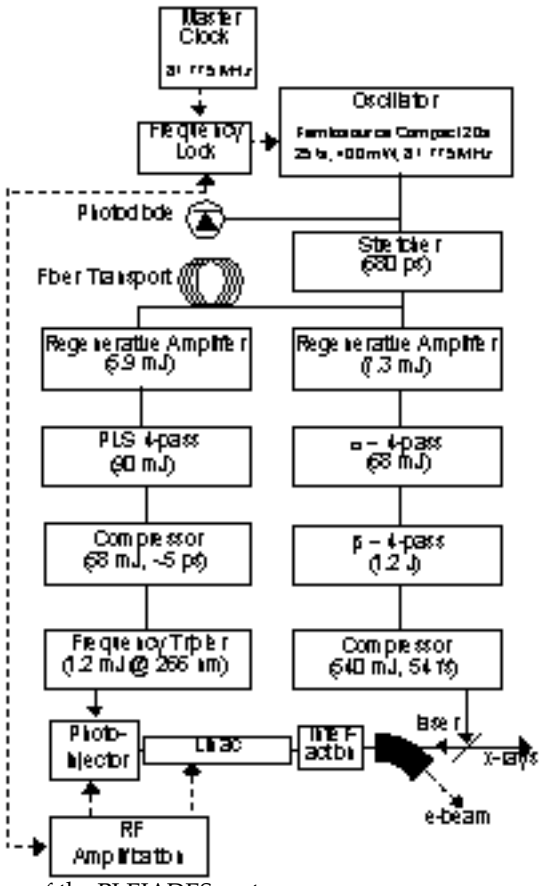

Figure 10 Block diagram of the PLEIADES system

Thus far, we have successfully demonstrated a flux of ~10^7 photons/shot, which corresponds roughly to a brightness of 10^{16} photons/mm^2/s/mrad^2/0.1% BW, at energies from 40-140 keV. The full results are presented in Chapter 4.

The PLEIADES facility requires the simultaneous integration of two laser systems and a new rf photoinjector with the existing 100-MeV Linear Accelerator at Lawrence Livermore National Laboratory (LLNL). A block diagram of the overall system is shown in Figure 10. The temporal overlap requirements necessary to produce Thomson x-rays mean the systems have to have less than 2 ps of temporal jitter (for a 90° interaction geometry) and less than 20 μm of spatial jitter at the interaction point.

Chapter 2 discusses the laser system used to generate the 500 mJ of ir light that is scattered off the electron beam to make the x-rays. Additionally, a potential upgrade to the system is presented: a hybrid chirped pulse amplifier (HCPA), which is capable of providing

much higher contrast laser pulses, useful if the laser is to also be used as a pump in a laser-pump/x-ray probe experimental set-up. Chapter 3 then discusses the electron system used, especially a potential option for a future Thomson source, an X-band rf photoinjector, which provides several benefits over current S-band technology. Chapter 4 presents the geometry of the interaction region as well as the results of the interaction experiments, allowing a test of the scattering theory presented in Section 1.2. Finally, Chapter 5 provides some future plans for the facility, including possible experiments, upgrades, and other uses.

Chapter 2. Laser Systems

There are two major components to a Thomson scattering source: the electron beam that provides the energy for the x-rays, and the high-intensity laser which provides the photons to carry away that energy. The laser subsystem is the subject of this chapter. The PLEIADES facility uses a titanium-doped sapphire (Ti:Sapphire)-based chirped-pulse-amplification (CPA) laser system, known by the name FALCON (originally standing for Femtosecond Accelerator Laser CONcept), to produce 500 mJ of compressed 820-nm laser light to scatter off the electron beam produced by the system discussed in Chapter 3. What drives the laser development is the nature of the Thomson scattering process. The fundamental issue is one of cross-section; the more electrons that see the maximum number of photons, the more x-rays will be produced. This drives maximization of the laser energy, minimization of the transverse spot size, and maximization of the interaction length. The only caveat is that the total laser intensity must remain low enough to keep $a_0<1$.

2.1 The PLEIADES Laser Facility

The PLEIADES Laser Facility consists of an ultra-short pulse front end oscillator and stretcher (which provides light for both the FALCON laser and the Photoinjector Laser System discussed in Section 3.2.1), the FALCON laser, and the transport and compression systems which carry the beam to the interaction region discussed in Section 4.1.2. Each of these are discussed in turn.

2.1.1 The Front End

The laser system begins with a mirror-dispersion-controlled[67], Kerr-lens mode-locked, Compact C20s Ti:Sapphire oscillator from Femtosource, which produces 30 fs pulses with a bandwidth of 37 nm centered at 818 nm (see Figure 11). This wavelength was chosen due to a large number of available dielectric optics designed for operation at 820 nm that were left over from a previous laser system. Reusing these optics for FALCON allowed significant cost-savings early on in the project. The laser puts out 450 mW of power with a repetition rate of 81.557 MHz

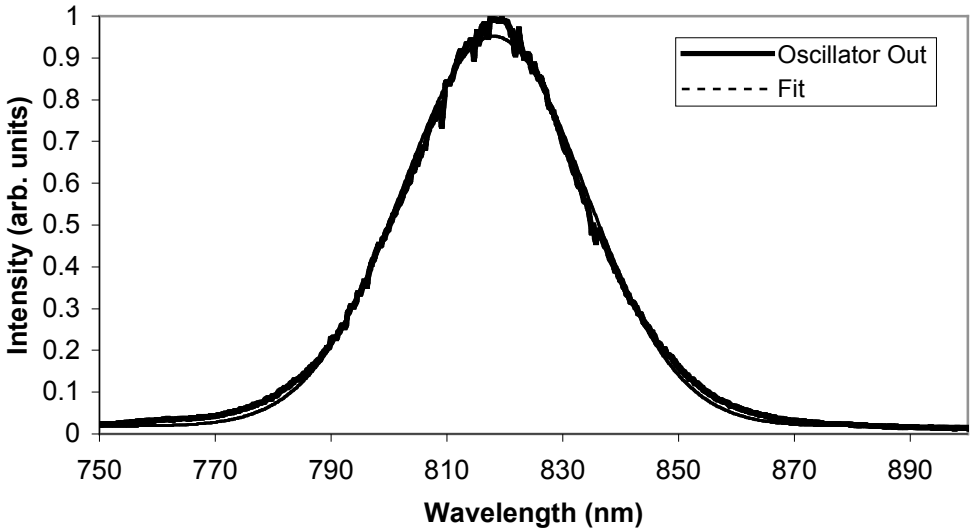

Figure 11 Spectrum of the Compact C20s oscillator that serves the PLEIADES Thomson source.

(the 35th subharmonic of the S-Band operational wavelength of the accelerator), which translates to 5.5 nJ per pulse. This oscillator is critical to the operation of the Thomson source as it provides the seed light for both the high-intensity scattering laser and the uv laser needed for the electron photoinjector, as well as serving as the master triggering signal for all the timing-sensitive systems.

To accomplish this latter function, two photodiodes monitor the output pulse train of the oscillator. One diode signal is split: half the signal is fed into an amplifier which frequency-filters it to produce a sinusoidal signal that is frequency multiplied in a phase-locked dielectric resonant oscillator to 2.8545 GHz (the operational frequency of the linear accelerator structure), and is sent to the rf amplification system. The other half of the signal is sent to a Time-Bandwidth CLX-1000 timing stabilizer. This box takes the measured oscillator pulse train and an 81.557 MHz crystal clock oscillator signal and keeps them phase locked. The feedback control is accomplished via a piezoactuator on the high-reflector end of the oscillator cavity to keep control over high-speed variations, along with a motorized translation stage under the same mirror to track longer term drifts. Because it is the oscillator pulse train that drives the rf equipment and not the clock oscillator, any errors the stabilizing box hasn't corrected for should still be tracked by the rf system, minimizing timing jitter problems. The second diode signal is sent into a SpectraPhysics

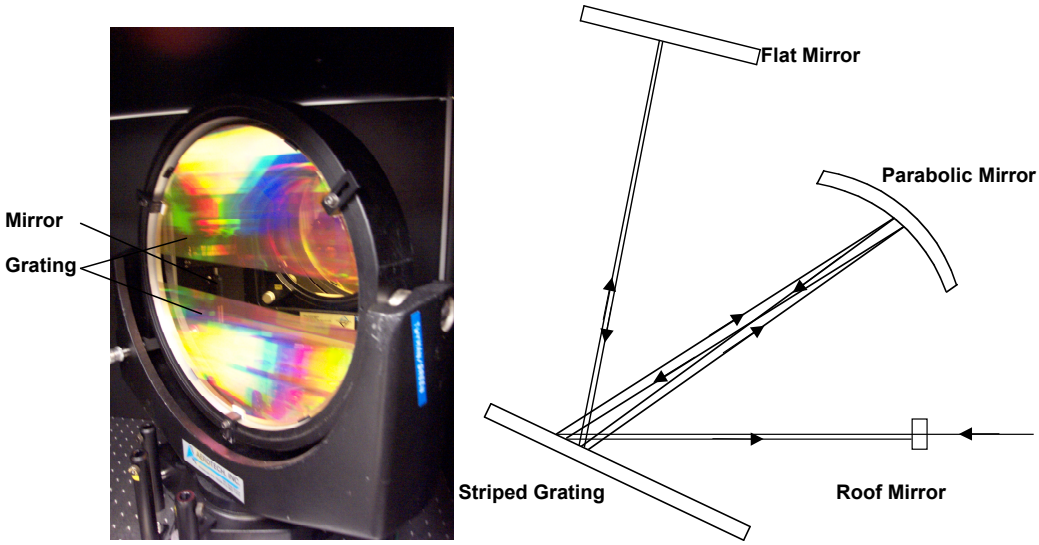

Figure 12 The parabolic-mirror based pulse expander layout.

SM-1 Synchronization Box, which takes the oscillator signal and a 10 Hz pulse train and generates a 10 Hz signal that is synchronized to the oscillator pulse train, which is then used as a trigger signal for the rest of the PLEIADES system. The jitter on this signal relative to the oscillator pulse is approximately 1 ns.

The pulse is then sent into a "aberration-free" all-reflective parabolic mirror based expander[68], diagrammed in Figure 12. This expander uses a unique custom grating which has a mirror stripe in the center. The beam enters the compressor, strikes the grating above the stripe, and diffracts towards a parabolic mirror. As the diffracted beam focuses off the parabola, it also travels downwards, and reflects off the mirror stripe and is directed towards the flat mirror. The flat mirror, which is located at the focus of the parabola, reflects the beam back towards the grating where it continues its downward motion, hits the mirror stripe and returns to the parabolic mirror. There the beam is recollimated and returned now to the lower half of the grating, where it is diffracted towards a roof mirror. This roof mirror shifts the beam height up an inch, and sends it back along the same path until the beam emerges from the compressor just above the input beam. The stretcher uses a 1480 line pair/mm grating, with an angle of incidence of 55°. After this expander, the stretched pulse length is 680 ps, as illustrated in Figure 13.

The stretched pulse train is then split with a dielectric beam splitter into two beams, with 30% of the light being coupled into a fiber to seed the photoinjector laser (see Section 3.2.1), and

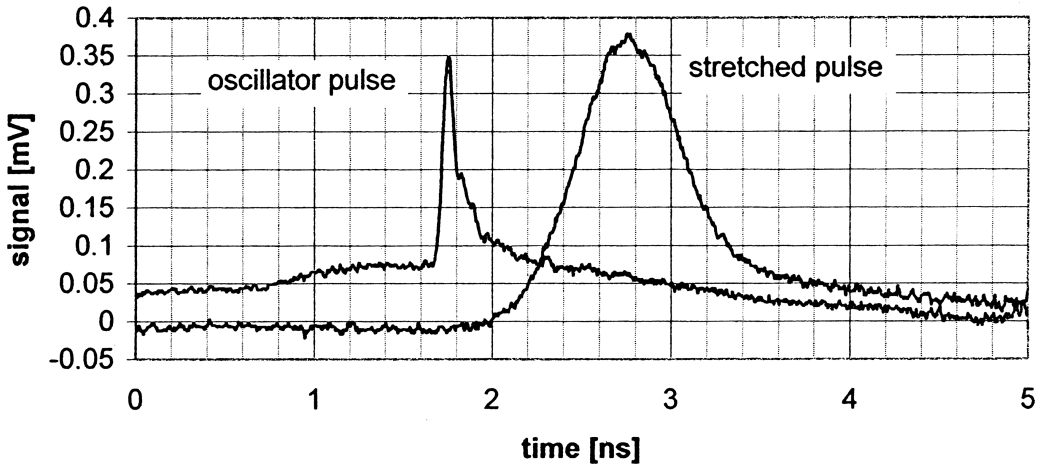

Figure 13 2 Ghz photodiode measurement of the stretched pulse length, showing a 680 ps pulse length. Also shown is a measurement of the oscillator pulse, which indicated the photodiode response speed.

the remaining 70% used to seed the FALCON laser. Because the same oscillator seeds both laser systems, minimal timing jitter between the systems is assured.

2.1.2 The FALCON Laser

The overall layout of the FALCON amplification system is shown in Figure 14. Following the beam splitter that separates the light for the uv laser and the main FALCON system, the pulse train is injected into a regenerative amplifier. This amplifier consists of a 2.4 m long linear cavity with two 1.5 m focal length concave end mirrors. The 10 mm diameter x 10 mm long Ti:Sapphire rod used as the gain medium is pumped by 45 mJ of 532 nm light from a frequency doubled SpectraPhysics GCR-190 Nd:YAG laser, producing 300 mJ of 532 nm light and running at 10 Hz. The *S*-polarized oscillator pulse train is injected into the cavity via reflection off a thin-film polarizing beamsplitter. This light will, in general, be sent right back out of the cavity reflecting off a second thin-film polarizing beamsplitter. The pulse to amplify is selected biasing a KDP-based pockels cell located between the two polarizers to its half-wave voltage, changing the polarization of the pulse to *P* and allowing it to pass through the second polarizer. The Pockels cell voltage is removed before the pulse returns to it, and the pulse is then trapped in the cavity. The pulse makes 9 round trips in this cavity before it reaches saturation with this pump energy, and has an energy of 7 mJ. To eject the pulse, the same pockels cell is again switched on,

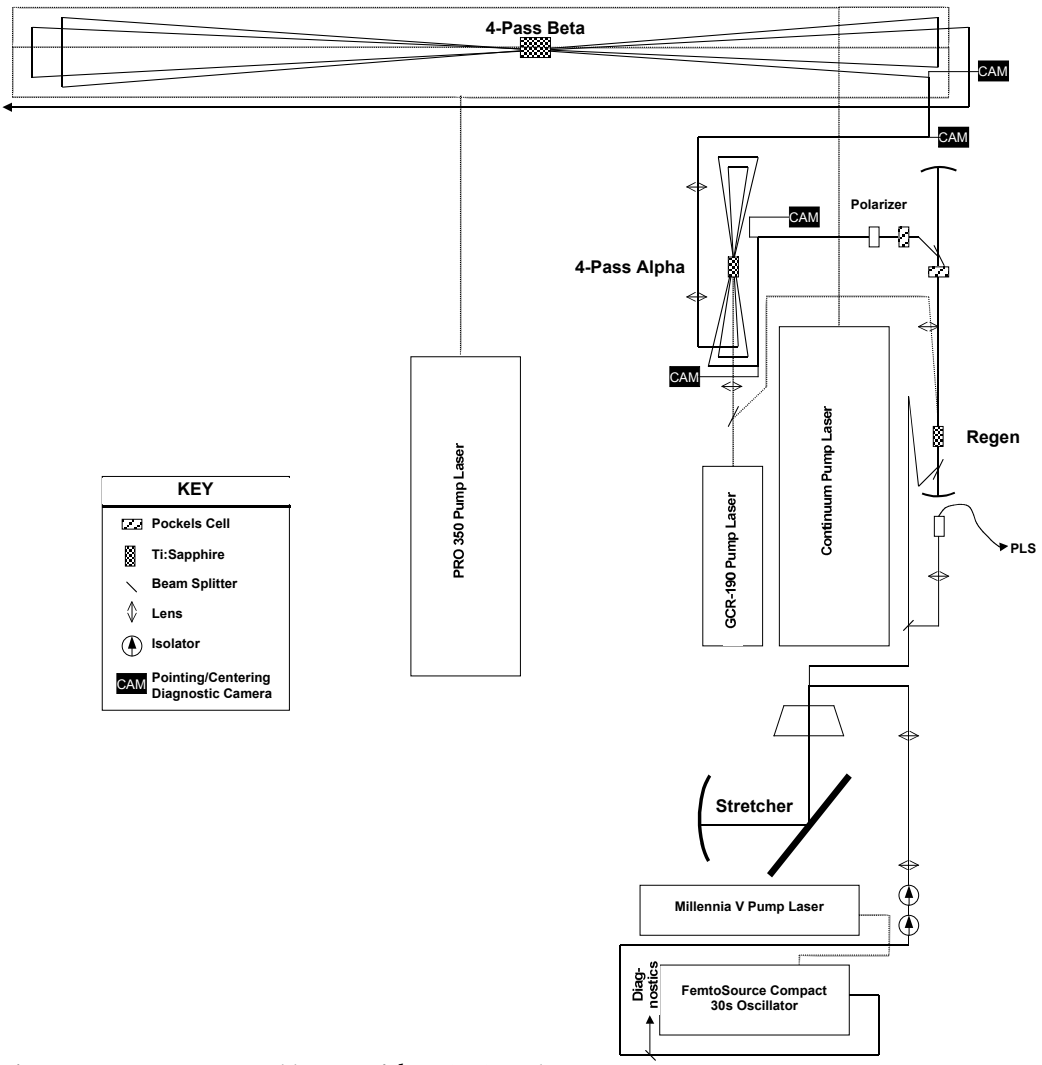

Figure 14 General layout of the FALCON laser system.

returning the polarization of the laser pulse to *S* and allowing it to reflect off the polarizer. Following the regenerative amplifier is a second pockels cell, a waveplate, and a Glan-Taylor polarizing cube, which are used to reject all the extraneous pulses from the oscillator and amplifier cavity, and leave the single amplified pulse. The final beam shape and spectrum are shown in Figure 15a. The $1/e^2$ spot radius is 0.98 mm x 1.04 mm, and the spectral FWHM is 24 nm.

Following the regenerative amplifier is the first of two power amplifiers. This amplifier, referred to as the "□-4-pass", is configured in a four-pass bow-tie geometry as depicted in Figure 14. The 25 mm diameter x 16 mm long Brewster cut Ti:Sapphire crystal is pumped with the 200

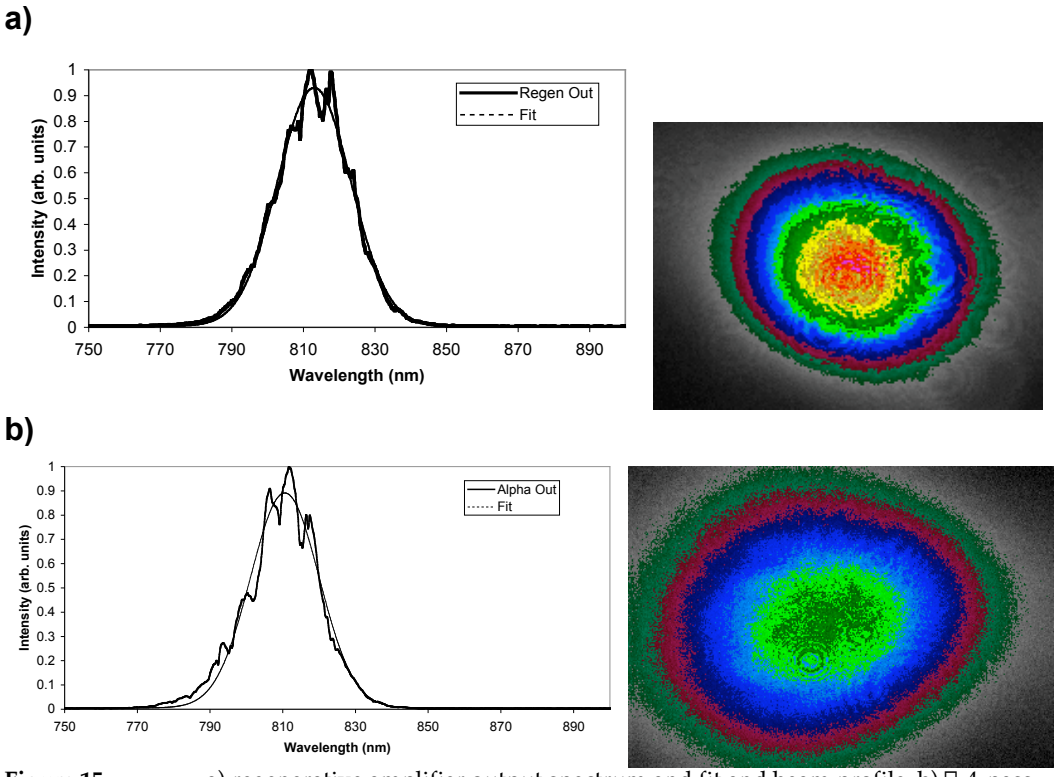

Figure 15 a) regenerative amplifier output spectrum and fit and beam profile. b) □-4-pass output spectrum and fit, and beam profile.

mJ of 532 nm light from the GCR-190 that is not used in the regenerative amplifier. The total gain of this amplifier is 9, giving a final output energy of 63 mJ. Figure 15b shows the beam profile (1.48 x 1.28 mm $1/e^2$ radius) and spectrum (22 nm FWHM) after this amplification stage. Considering the final application of this system, one major concern is the pointing stability of the laser. To generate x-rays, the laser will have to travel over 50 m, and still arrive at a spot 20 μm in diameter. To help minimize long-term drift, an automated pointing and centering system has been installed. Laser light leaking through two mirrors (as shown in Figure 14) is imaged into two cameras to provide pointing and centering reference images. LabView-based software monitors these images, and adjusts the beam pointing accordingly.

After the □-4-pass is a second power amplifier, the □-4-pass, This stage, like the □-4-pass, is a four-pass bowtie configuration. The 25 mm diameter x 25 mm long Ti:Sapphire crystal is pumped simultaneously by two different lasers. One is a SpectraPhysics PRO-350 frequency-doubled Nd:YAG system producing up to 1.5 J of 532 nm light, and the other is a Continuum frequency doubled Nd:YAG system which produces 1.2 J of 532 nm light. Both lasers produce

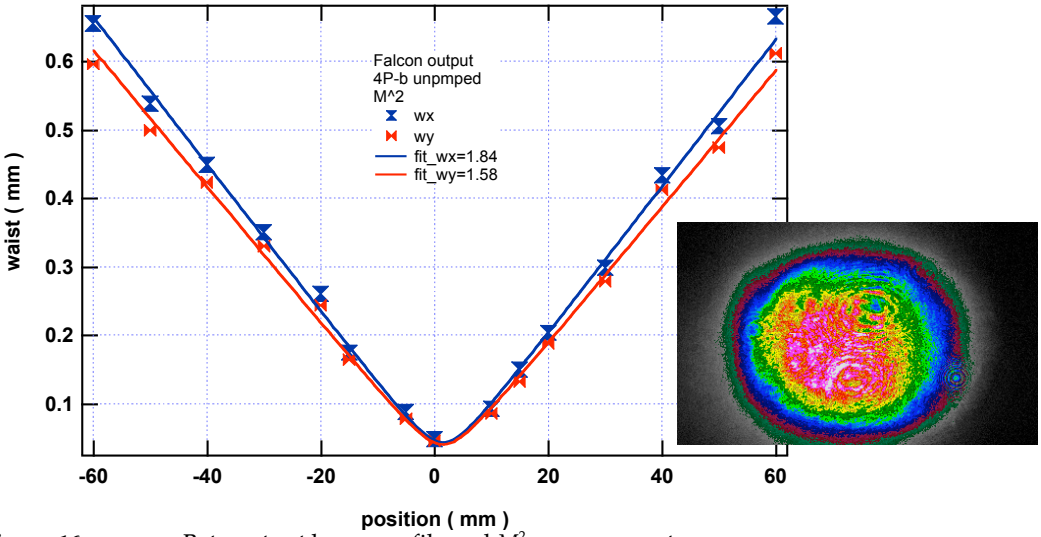

Figure 16 Beta output beam profile and M^2 measurement.

supergaussian beams which are relay imaged to the Ti:Sapphire crystal to maintain their quality, with a diameter of 11 mm. Both beams are split in two and each pumps the gain medium from both sides This helps to assure uniformity of the gain region in the crystal. Again, the incoming ir beam is monitored by the automated pointing and centering system to preserve, over the course of the operating day, the alignment of the laser through the amplifier.

2.1.3 Beam Quality

The overall gain of the □-4-pass is 20, giving a final energy output of 1.2 J. Figure 16 shows the final beam profile out of the amplifier. The $1/e^2$ beam radius is 35 x 37 mm after the expanding telescope. Because the nature and quality of the focal region of the laser is directly relevant for the scattering interaction, an M^2 measurement was made by measuring the beam waist, $w(z)$, as a function of position about the focal point. Fitting this curve to the beam propagation equation

$$w(z) = w_0\sqrt{1+\left[\frac{M^2(z-z_0)}{w_0^2}\right]^2} \tag{30}$$

gives a value for M^2, which gives a reliable measure of beam quality. (This quality measurement is very similar to the emittance of an electron beam, a parallel which will be discussed in more

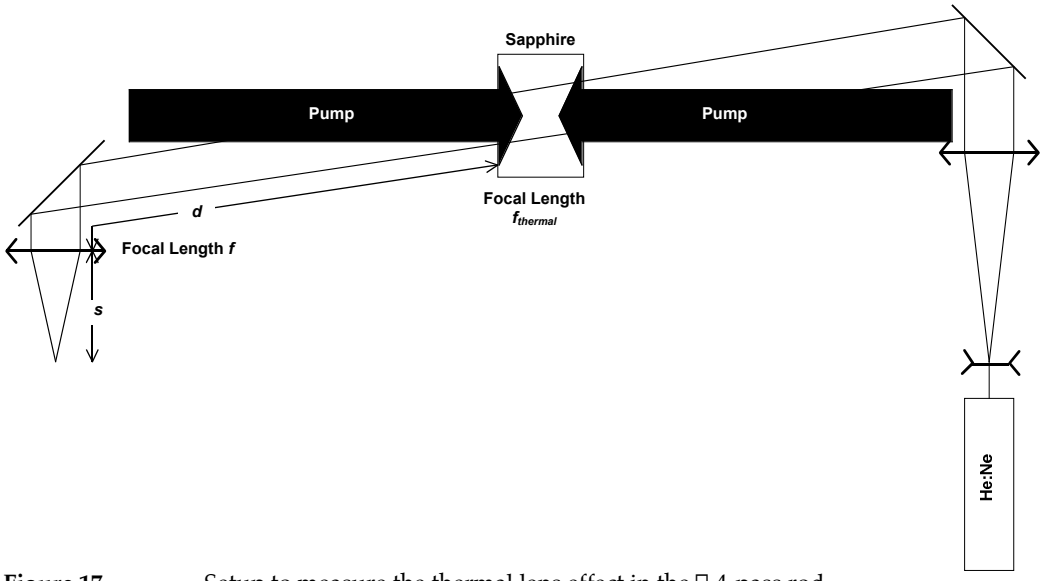

Figure 17 Setup to measure the thermal lens effect in the -4-pass rod.

detail in Section 3.1.1). The M^2 measurement of the beam waist is shown in Figure 16, and gives a value of 1.64 in the x direction and 1.58 in the y direction

Another factor that will affect the laser focus in the interaction region is the effect of thermal lensing in the -4-pass, There are three effects that contribute to the thermal lens in an end-pumped rod[69]. One is the temperature-dependant index of refraction of the gain medium. A transverse temperature gradient becomes a transverse index gradient, acting in effect like a lens. The second effect is the thermal expansion of the gain medium. Higher temperatures in the center of the rod result in the center expanding more than the edges, leaving a curvature to the rod that results in a lensing effect. The third effect results from thermal stresses induced in the rod, which translate to variations in the index of refraction via the photoelastic effect.

To examine the thermal lensing effect in this system, the setup shown in Figure 17 was used[70]. A He:Ne laser beam is enlarged to a size comparable to that of the ir beam to be amplified, collimated, and passed through the Ti:Sapphire crystal. This beam is then focused and the focal position noted. The crystal is then pumped, and the change in the position of the focal spot is measured. This chain of optics is modeled via simple ray-tracing matrices by

$$\underbrace{\begin{pmatrix} 1 & s \\ 0 & 1 \end{pmatrix}}_{\text{Space}} \underbrace{\begin{pmatrix} 1 & 0 \\ -\frac{1}{f} & 1 \end{pmatrix}}_{\substack{\text{Focus} \\ \text{Lens}}} \underbrace{\begin{pmatrix} 1 & d \\ 0 & 1 \end{pmatrix}}_{\text{Space}} \underbrace{\begin{pmatrix} 1 & 0 \\ -\frac{1}{f_{thermal}} & 1 \end{pmatrix}}_{\text{Sapphire}} \underbrace{\begin{pmatrix} 1 \\ 0 \end{pmatrix}}_{\substack{\text{Collimated} \\ \text{Ray}}} = \underbrace{\begin{pmatrix} 0 \\ x \end{pmatrix}}_{\substack{\text{Ray at} \\ \text{Focus}}}$$

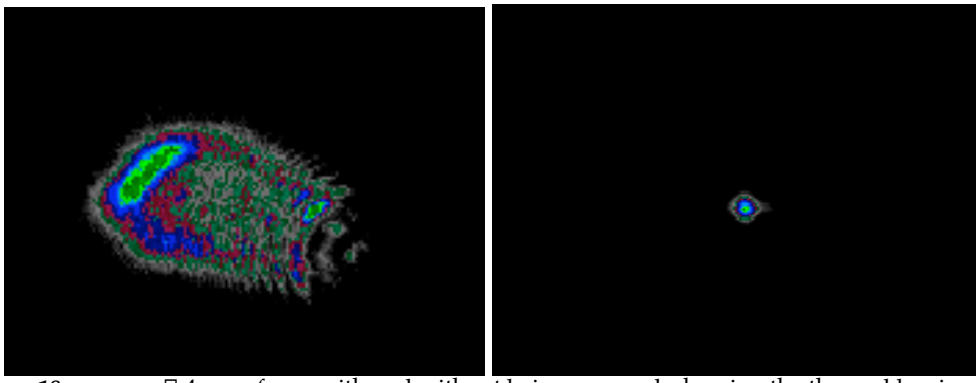

Figure 18 -4-pass focus with and without being pumped, showing the thermal lensing effect on the focus. In the pumped case, the pump lasers are mistimed to there is no gain.

Carrying out the matrix multiplication gives

$$\begin{bmatrix} 1 - \frac{s}{f} & d\left(1 - \frac{s}{f_{thermal}}\right) + s\left(1 - \frac{d}{f_{thermal}}\right) \\ -\frac{1}{f} & 1 - \frac{d}{f_{thermal}} \end{bmatrix} \begin{bmatrix} 0 \\ x \end{bmatrix}.$$

In the case of the unpumped sapphire, $f_{thermal}$ becomes infinite, and s becomes equal to f. Defining $\Delta s = f - s$, the change in the focal position as the thermal lens changes, an equation for $f_{thermal}$ can be found:

Table III — Values used in the thermal lensing calculation

K	Heat conductivity	46 W m^{-1} K^{-1} [71]
$\frac{\partial n}{\partial T}$	Thermal coefficient of refractive index	$1.2 \cdot 10^{-6}$ K^{-1} [71]
α_e	Coefficient of thermal expansion	$5 \cdot 10^{-6}$ K^{-1} [71]
n	Index of refraction	1.763 [71]
r_0	Rod radius	15 mm
L	Rod length	25 mm
w_p	1/e2 pump beam radius	3.25 mm
Q	Heat absorbed by rod	5.6 W

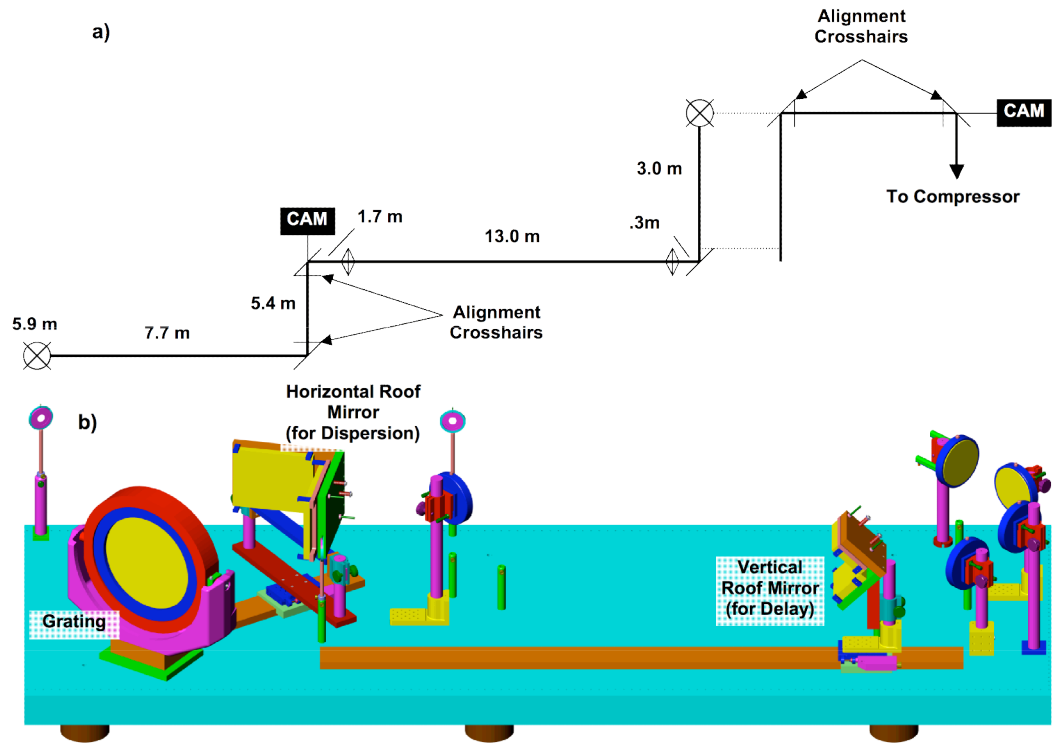

Figure 19 a) Schematic of the transport system to the compressor, showing the alignment references, and b) a 3D-CAD model of the FALCON compressor

$$\left(1-\frac{s}{f}\right)\left(1-\frac{d}{f_{thermal}}\right)-\frac{s}{f_{thermal}}=\left(1-\frac{f-(f-s)}{f}\right)\left(1-\frac{d}{f_{thermal}}\right)-\frac{f-(f-s)}{f_{thermal}}$$

$$=\frac{\Delta s}{f}\left(1-\frac{d}{f_{thermal}}\right)-\frac{f-\Delta s}{f_{thermal}}$$

$$=\frac{1}{f_{thermal}}\left(\frac{f_{thermal}\Delta s}{f}-\frac{d\Delta s}{f}-(f-\Delta s)\right)=0$$

$$f_{thermal}=\frac{f}{\Delta s}\left(\frac{d\Delta s}{f}+f-\Delta s\right)=d-f+\frac{f^2}{\Delta s}$$

Using a focusing lens with f=500 mm, and a distance from the sapphire rod of d=1400 mm, pumping with 1.06 J of energy showed the focus to move a distance of Δs=5.297 mm, corresponding to a thermal lens of $f_{thermal}$=48.1 m. The theoretical expectation for the thermal lens is given by[70]

$$f_{thermal}=\frac{K\pi w_p^2}{Q}\left(\frac{\partial n}{\partial T}+\frac{2\pi r_0(n-1)}{L}\right)^{-1}$$

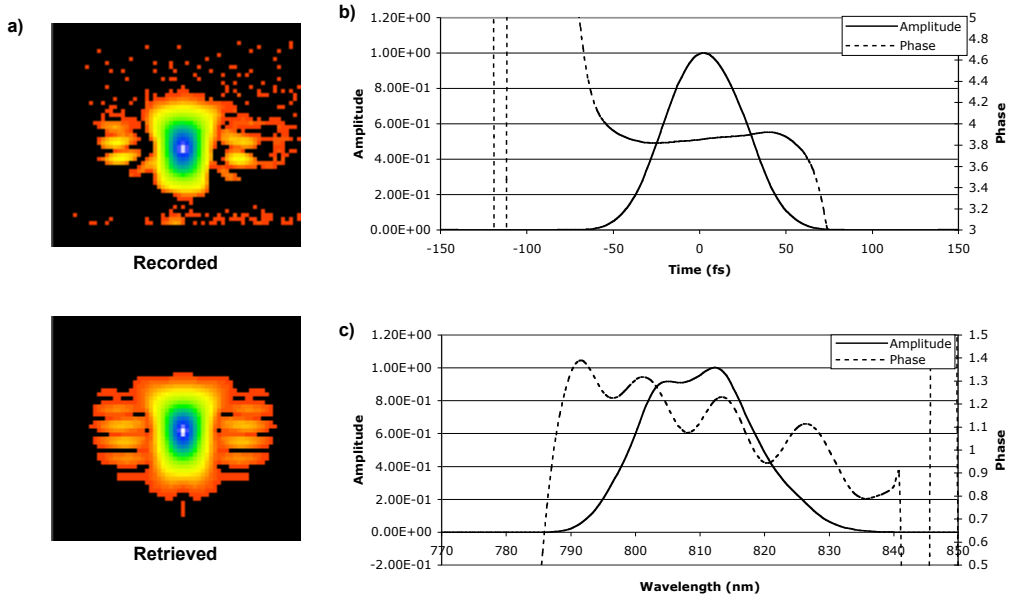

Figure 20 a) Recorded and retrieved GRENOUILLE traces of the FALCON compressor output. b) retrieved temporal amplitude and phase c) retrieved spectral amplitude and phase.

with the various constants and variables given in Table III. This predicts a thermal lens for the experimental set-up of $f_{thermal}$=47.2 m, and for the fully pumped FALCON system of $f_{thermal}$=20.5 m. Figure 18 shows the change in focus between a pumped and unpumped rod in the □-4-pass. In the pumped case, the pump lasers are mistimed, so they have a thermal effect on the rod, but there is no gain in the crystal.

Following the □-4-pass, the beam is up-collimated for transport to the pulse compressor. The laser is relay imaged 46.5 m to the compressor via a vacuum relay telescope as shown in Figure 19a. In order to align the laser through the transport system, four automated crosshairs were installed that could be inserted remotely into the beam. Two cameras view the leakage light through two of the mirrors to monitor the beam alignment, and four motorized mirror are used to manually adjust the beam path. The compressor itself is shown in Figure 19b, and it compresses the beam to 55 fs, as shown in the GRENOUILLE[72] data in Figure 20. The compressed pulse then propagates 20 m to the final focusing optics. The transmission through the transport and compressor is 45%, leaving up to 540 mJ available in the interaction region for Thomson scattering, as discussed in Section 4.1.2.

2.2 A Hybrid Chirped-Pulse Amplification System

There are essentially two ways to create or amplify a collection of coherent photons. The first, most common, and most well known, is through laser action. Here some gain medium, be it a solid (such as a titanium-doped sapphire crystal or neodymium-doped glass), liquid (dye lasers) or gas (He:Ne, Argon Ion, or excimer lasers) is given energy in the form of light, electricity, or even a chemical reaction, which creates a population inversion between a ground state and a metastable excited state. A photon of the right energy passing through this medium can then quantum mechanically trigger the release of this stored energy into additional, identical, coherent photons. This is the stimulated emission of radiation from which lasers take their name. However, there is an alternative.

2.2.1 Optical Parametric Amplification

The transfer of the energy to a gain medium can be bypassed entirely, and the energy can instead be passed directly to the desired beam. As and example, while a 808-nm laser diode, directed onto a Nd:YVO_4 crystal can create an inversion which can lead, through laser action, to the generation of a 1064 nm beam, that 1064 nm beam can be directed at a (properly oriented) KDP crystal to generate a 532 nm beam via nonlinear processes, where two 1064 nm photons interact to create a 532 nm photon through harmonic generation. By the same physical process, one beam can be amplified with light from a second beam via difference-frequency generation (DFG). Here, a high-photon-energy "pump" beam (wavelength λ_p) is mixed in a nonlinear crystal with a lower-photon-energy "signal" beam (λ_s). What is generated is an "idler" beam (λ_i) with photons of energy

$$\hbar\omega_p - \hbar\omega_s = \hbar\omega_i \quad \frac{1}{\lambda_p} - \frac{1}{\lambda_s} = \frac{1}{\lambda_i}.$$

For example, with a 532-nm pump and a 800-nm signal, a 1588-nm idler will be generated. More importantly, for each idler photon that is generated, another signal photon is also created, amplifying the signal beam.

Naturally, the catch of this direct conversion scheme is that it essentially requires the work of the laser amplification scheme to have already been done, because getting reasonable

efficiency out of nonlinear processes requires relatively high intensity coherent beams. However, once such a beam is available, the range of nonlinear processes and materials allows many regimes of operation that would otherwise be difficult to reach. Most notably, optical parametric oscillators and amplifiers can be made to function over the bulk of the light spectrum, from ir to uv, with proper selection of angles in the nonlinear media. Compare this with the need to find a gain material with a proper energy structure to lase at a given wavelength, and the benefits of the parametric process becomes obvious.

In addition to tunability, a parametric system can also have very wide gain bandwidths (crucial for ultrahigh intensity and short pulse applications). This feature led to the suggestion[73] that chirped pulses be amplified via parametric processes. This process is referred to as Optical Parametric Chirped Pulse Amplification (OPCPA). The amplification and subsequent compression of a pulse via OPCPA was performed in 1992[74]. A thorough study of the potential of OPCPA systems was performed[75], an it was concluded that, with current technologies, powers in excess of 10 PW and intensities greater than 10^{23} W/cm^2 are achievable.

There are several additional benefits that accrue from using OPCPA for amplification, which suggest that OPCPA might be an excellent candidate for replacement of regenerative amplifiers. First, the optical nonlinearities of some materials are high enough to allow gain on the order of 10^4-10^5 in just a single pass of a few cm of material. This would eliminate the complicated multiple-pass schemes to get large amounts of gain that necessitate regenerative amplifiers. The need to construct a cavity and switch the laser light into and out of it would be eliminated, removing considerable complexity in the system.

Second, in a cavity each time the pulse passes the switch-out point, a small (~1%) amount of light leaks out of the regenerative amplifier. This results in a train of pulses at the exit of the amplifier spaced typically several nanoseconds apart. As these pre-pulses propagate through the laser chain, they can be amplified by subsequent stages just as the main pulse is. For experiments where this beam will strike a target, these prepulses can have a significant impact on that target, by ablating or pre-ionizing it before the arrival of the main pulse, significantly affecting the physics of the main pulse interaction. The common solution to this problem is to use combinations of Pockels cells and waveplates to act as pulse slicers and improve the contrast

between the main pulse and the prepulse. In an OPCPA system, however, the only pulse that sees any amplification is the pulse coincident with the pump beam; the rest of the pulse-train is not amplified. The prepulse contrast then matches the gain in the OPCPA stage. Since gain is easily on the order of 10^5, this is already a three-order-of-magnitude improvement over the regenerative amplifier contrast. Furthermore, a scheme has been proposed[76] which could have essentially infinite prepulse contrast, known as cascaded optical parametric amplification (COPA). In this scheme, after the first stage of amplification, the signal beam is dumped and the idler is instead kept, which of course has only one pulse; the one corresponding to the arrival of the 532-nm light. This idler beam can then be remixed with the pump light in a second stage, and reconverted to the signal wavelength, only now with no pre- or post- pulses.

Of course, everything comes at a price, and the costs of the benefits of OPCPA over a regenerative amplifier manifest themselves as considerably more stringent pump beam requirements. Since light transfers directly into the seed beam from the pump in this system, with no "energy storage" mechanism, energy transfer is realized only when the two beams overlap in space and time. Conventional pulse stretchers generally produce stretched pulses of duration ~1 ns or so. Commercial Q-switched pump lasers produce pulses on the scale 8-10 ns. This mismatch in pulse length means most of the pump energy is wasted, never seeing the seed light, giving efficiencies on the order of 1-2%. This means that in order to get reasonable efficiencies out, a custom pump laser must be built to match the temporal profile of the stretched pulse. Efficiencies of up to 30% have been demonstrated[77] this way, however the need to build and operate a custom pump laser defeats the "simplicity" arguments for replacing the regenerative amplifier with an OPCPA stage.

There is, however, an alternative to the custom-pump-laser scenario. Once a commercial pump laser signal has been used in an OPCPA stage to amplify a signal beam, all the unused pump light (less surface reflections) is still available. This is in contrast to a laser amplifier where the pump light is absorbed by the gain medium, and if unused is lost to heating of the medium. This leftover pump light can be used to pump a laser amplifier, and traditional laser action can be used to further amplify the signal pulse. This unused light will have an unusual temporal structure, having been (hopefully) largely depleted for the duration of the signal pulse, but this

won't matter for pumping long-lifetime gain media, which simply integrates the energy. In essence, the canonical "regen+multipass amplifier" scheme becomes an "OPCPA+multipass", gaining the benefits of simplicity of set-up, high contrast prepulses, and no need for electroopics to do any pulse switching, without sacrificing efficiency. This scheme has been dubbed "Hybrid Chirped-Pulse Amplification", or HCPA[78].

The temporal demands of OPCPA on the pump laser also require the pump-laser beam be seeded to stabilize the pulse's temporal profile and eliminated beatings of the longitudinal modes of the cavity. Without seeding, the pump amplitude's temporal profile with be different with each shot, leading to large jitter in the amplified OPCPA energy. Also, because the energy is directly transferred from the pump beam to the signal beam, the pump beam profile is critical. Common tricks for homogenizing the pump beam profile in a gain medium such as splitting and inverting part of the beam, aren't feasible here. Furthermore, because a nonlinear process is involved, the pump profile variations will be transferred to the signal beam in an exaggerated form, with the variation depth amplified. Therefore it is imperative to have a very high quality pump beam.

2.2.2 Experimental System

The goal of this work was to demonstrate a terawatt-class HCPA laser system, including compression to the Fourier-transform limit of the pulse. More specifically, I wanted to compare the spectral phase introduced by the OPCPA amplifier setup to that of the regenerative amplifier, in the case of non-collinear, non-degenerate amplification. This is a study that hasn't been performed, and is crucial for demonstrating the viability of OPCPA systems to produce ultrashort pulses: if the OPCPA stage were to introduce unusual spectral phase effect that could not be compensated for, short pulses would be unproducable. To do this, a comparison of pulses from a regenerative amplifier and an OPCPA amplifier, both going through the same multipass amplifier, was performed. The ultimate goal here is to determine the feasibility of using the HCPA system to replace the regenerative amplifier and -4-pass of the FALCON laser altogether.

The setup used is shown in Figure 21. The same oscillator, pulse stretcher, and regenerative amplifier discussed in Sections 2.1.1 and 2.1.2 were used. After the pulse slicer at the

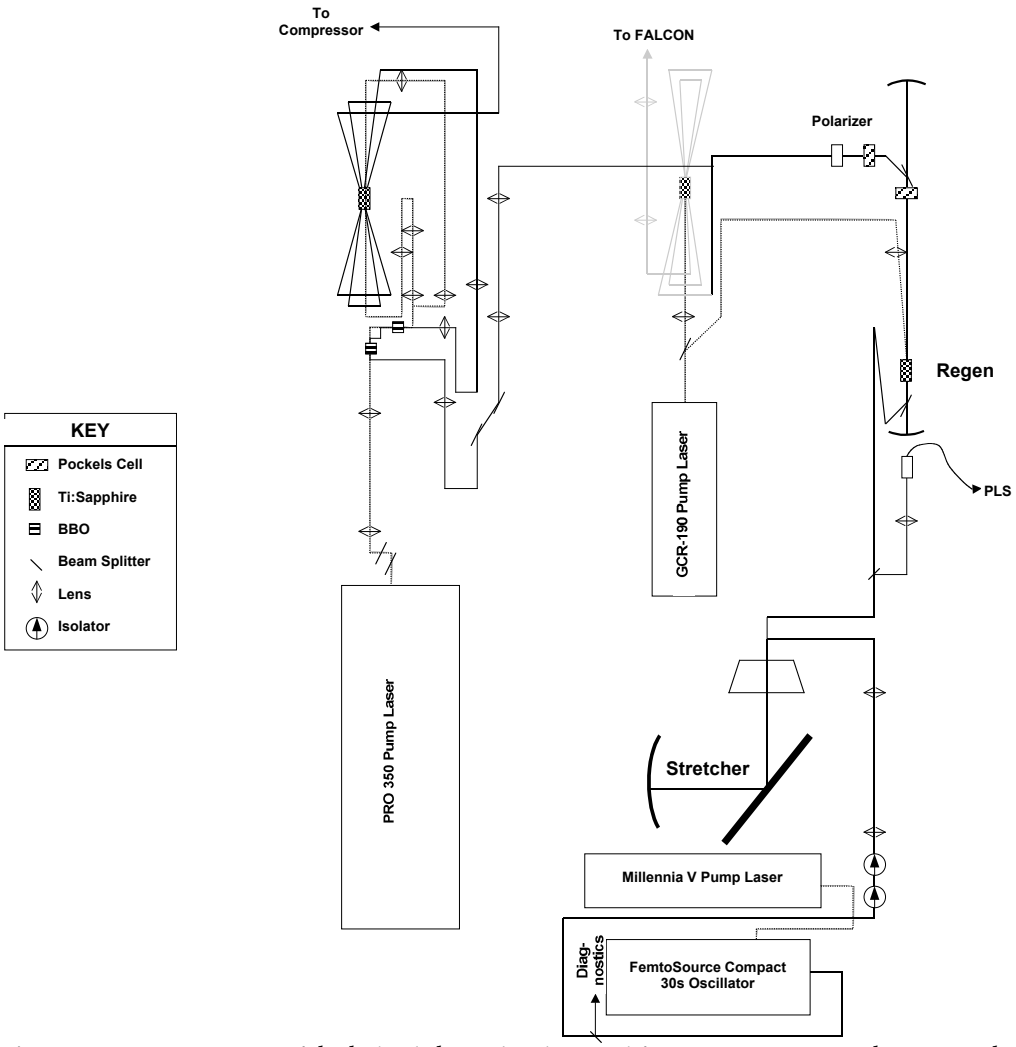

Figure 21 Layout of the hybrid chirped-pulse amplification system. Note that it uses the same front-end components as the FALCON laser system (Figure 14).

regenerative amplifier exit, a flip-mirror was used to divert the light from the main FALCON beamline to the experimental OPCPA setup. This beam is down-collimated with a reducing telescope to give a beam that is 2.5 mm FWHM. This beam is then sent through a waveplate and off a pair of polarizing beamsplitters to allow for adjustment of the seed energy going into the OPCPA stage.

35 mm of β-barium-borate (BBO) material is needed to give enough gain length to get a ~1 nJ seed pulse to an energy of ~1 mJ. In order to maximize the overlap between the pump and signal beams over the length of the material, two crystals are used: one is 10 x 10 x 20 mm, the other is 10 x 10 x 15 mm. This allows the two lengths to be aligned independently for maximum gain. The

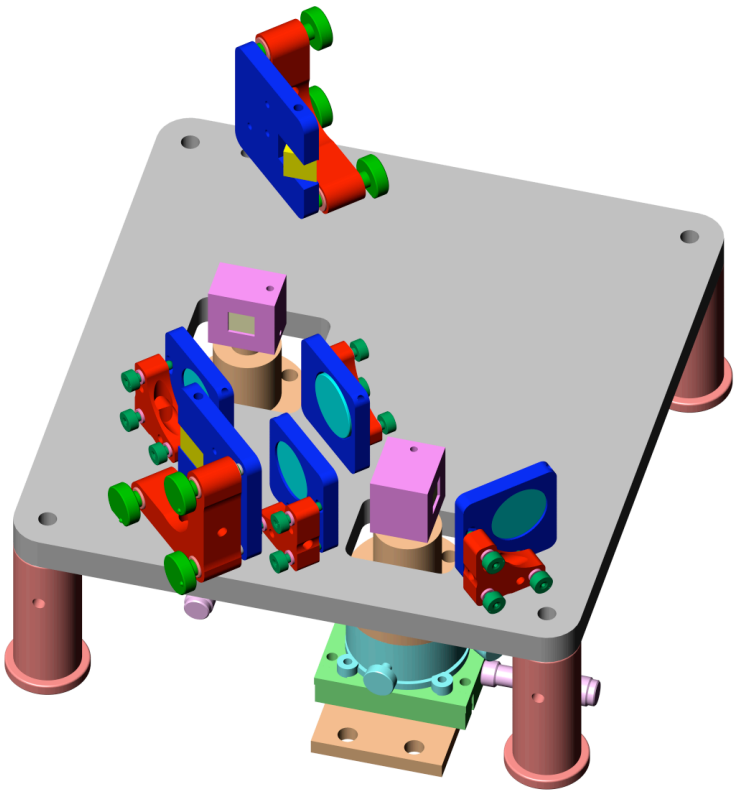

Figure 22 The layout of the OPCPA amplifier table. This setup allows the crystals to be brought close enough together to avoid having to relay the green pump light between the two crystals.

system will be pumped by the supergaussian beam of the SpectraPhysics GCR PRO-350 laser mentioned in Section 2.1.2. Because the quality of the pump beam profile is imaged directly onto the amplified beam, it is important to have a uniform pump profile; therefore, the supergaussian beam must be relay imaged to the BBO crystals. There are then two choices: relay the beam to the center of the first crystal, then relay it again to the center of the second, or relay to the midpoint between the crystals. In the interest of simplicity, the latter option was chosen, which then requires the two BBO crystals be placed as close together at possible, while still allowing independent alignment. A particularly compact scheme, shown in Figure 22, was designed using a custom plate to hold the optics as close together as possible by eliminating the need for tablespace to clamp them down. This also allows the size of the rotation stages under the BBO crystals to not dictate the spacing of the mirrors by creating a bi-level optical bench.

Shown in Figure 22 are the two BBO crystals, both of which are cut at 23.8° to allow phase matching of the 532 nm, 810 nm, and 1550 nm light waves in a Type I geometry (i.e. the 810

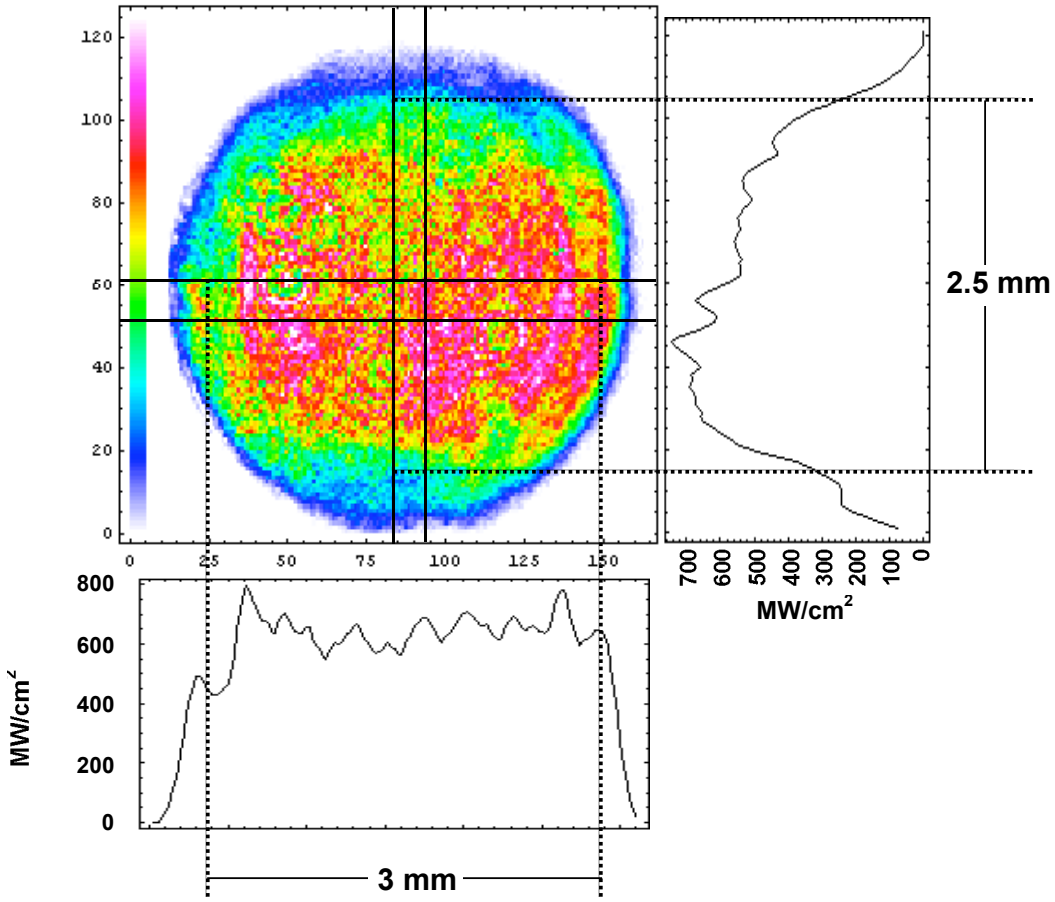

Figure 23 The pump beam profile in the OPCPA stage. The profiles are averages over the 10-pixel region about the centroid indicated by the boxes on the profile.

and 532 nm light have the same polarization, which gives the maximal spectral bandwidth). The pump and signal beam will interact with an external angle of 3.73° to give broad gain bandwidth centered around 850 nm. The green pump light is down-collimated to be 3 mm x 2.5 mm in the two crystals, and is shown in Figure 23. The smaller size in the vertical dimension is due to inefficient frequency doubling in the vertical direction in the pump laser. The green pump energy is 280 mJ, giving a pump intensity of ~680 MW/cm^2. It passes through two dichroic beamsplitters on either side of the first crystal before being turned with a right angle prism. It then passes through a third dichroic beamsplitter before the second crystal and is then bent once more by a right angle prism.

The temporal profile of the pump laser pulse is illustrated in Figure 24. Because of the unstable resonator configuration of the pump laser, there is a radially dependant variation of the

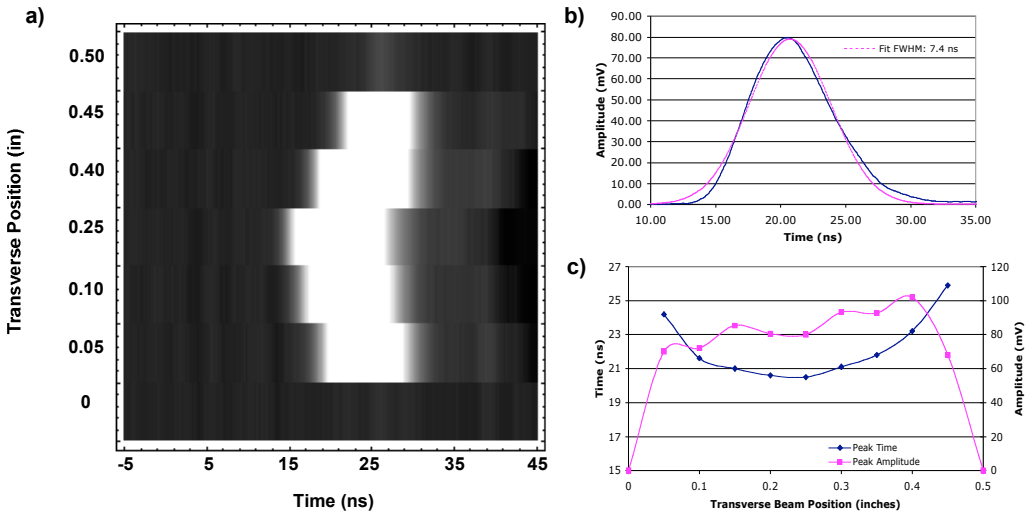

Figure 24 Pump laser temporal profile. a) laser intensity as a function of time and transverse position (note the position axis is not linear). b) Plot of the 0.25" position temporal intensity with fit. c) the delay of the pump peak and the amplitude as a function of transverse position.

buildup time. The temporal profile of the pump pulse was measured as a function of position across the beam and the resultant data is shown in Figure 24a. The delay and amplitude of the pump pulse are plotted in Figure 24c. The pulse peak in the center of the pulse arrives almost 4 ns ahead of the peak in the edges. The net effect of this pulse shape is that the pump beam size in the time slice where the signal pulse is present is significantly smaller than the time-integrated profile shown in Figure 23, which then means the Poynting vector and non-collinear walk-off will cause the two beams to stop mixing sooner than would otherwise be expected from the measured beam size. The pulse length at the center of the pump beam, shown in Figure 24b, is 7.4 ns.

The seed beam reflects off the two dichroic mirrors to pass through the first crystal, then off the third to pass through the second crystal. The 3.73° noncollinear angle is chosen to be in the vertical plane in the first crystal so the walk-off between the pump, seed, and idler beams due to the noncollinear angle doesn't add with the Poynting vector walk-off of the pump, but is instead in the perpendicular direction. In the second crystal, the non-collinear angle is in the horizontal plane for convenience in separating the pump beam (which reflects off a right angle prism) and the signal beam (which passes beside the prism). In the first crystal, the seed beam FWHM is 0.83 x 0.88 mm (Figure 25). This small size gets the intensity of the seed beam up, increasing the conversion efficiency, and helps keep the seed beam within the envelope of the pump beam for

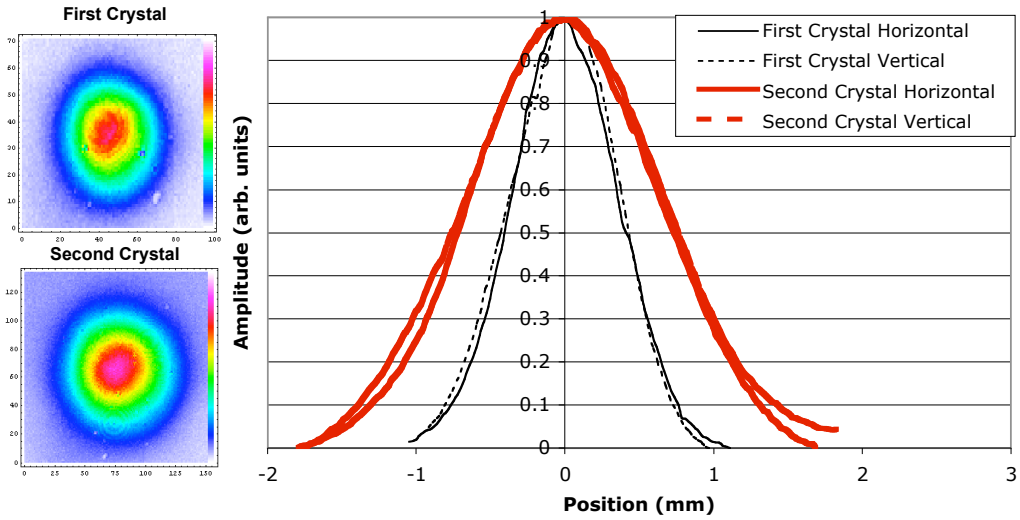

Figure 25 Profiles of the OPCPA seed light (regenerative amplifier output) at the first and second BBO crystals, and column- and row- sums of the profiles. The FWHM of the beam in the first and second crystal is 0.86 mm and 1.51 mm respectively.

the whole length of the longer crystal. In the second crystal, however, a larger beam size of 1.48 x 1.53 mm is used. This larger size is needed to minimize the effects of local pump depletion that would result if all the energy were extracted from a small area of the pump profile. Because the second crystal is shorter, the walk-off over the length of the crystal isn't as significant an effect. To get these two different beam sizes in the two crystals, an expanding beam is used to seed the OPCPA. A 289 mm focal length lens focuses the seed beam before the first crystal, so that in the beam is a reasonable size at each of the two crystals. The beam is then collimated by a 451 mm focal length lens, giving a final beam size of 2.03 x 2.04 mm FWHM for the seed beam at the OPCPA exit.

Following the OPCPA stage, both the remaining pump light and the amplified signal beam are sent to a 4-pass Ti:Sapphire amplification stage. The pump light, after being picked off with the right-angle prism, is split into two equal-energy beams, and relay imaged to the Ti:Sapphire crystal from either side as shown in Figure 21. Splitting the beam both makes its transport to the crystal easier, in terms of avoiding damage fluences on mirrors away from relay planes, and allows for more uniform pumping as any asymmetries in the pump beam profile are smoothed over by the inversion of the profile along the horizontal axis due to the opposing propagation directions. The pump energy arriving at the rod sums to 168 mJ after losses in both

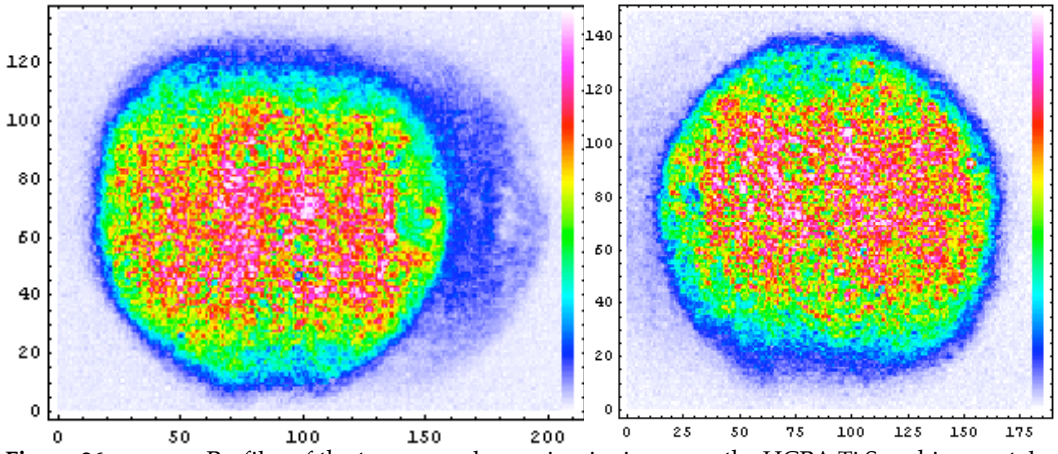

Figure 26 Profiles of the two pump beams impinging upon the HCPA Ti:Sapphire crystal.

the OPCPA stage and transport . The pump energy measured leaving the crystal is 18.8 mJ, leaving a total absorption of 89.2%. The pump beam profile at the Ti:Sapphire rod is shown in Figure 26, and has a diameter of 3.4 x 2.7 mm FWHM. The seed beam profile at the Ti:Sapphire crystal depends on the OPCPA or regenerative amplifier stage, and will be discussed in Section 2.2.3.

Following the 4-pass amplifier, the beam is sent to a pulse compressor for recompression to the frequency bandwidth limit. This is compressor uses a single 1480 line pair/mm grating and two roof mirrors to simulate the traditional four grating strikes; the general geometry is the same as shown in Figure 19b for the FALCON compressor. The angle was set based on a model of the spectral phase through the whole system. The stretcher grating and incidence angle are dictated by the needs of the FALCON laser system, and were not adjustable to optimize the pulse compression for the HCPA system. Given the stretcher geometry and the amount of material in the system, and starting with an assumption of 20 fs bandwidth in the pulse, with the regenerative amplifier operating in its standard 9-round-trip mode, the best compressed pulse achievable would be 52.1 fs. This is limited by fourth and fifth order phase errors that result from the amount of material in the laser system. If the number of trips in the regenerative amplifier is taken to be a variable, the model suggests using 40 round trips would allow compression down to 23.5 fs. The compressor was set up at the correct angle for this shorter compression, with an angle of incidence of 58.05°. To choose the right number of round trips, GRENOUILLE retrievals of the compressed pulse phase were made as a function of number of round trips in the

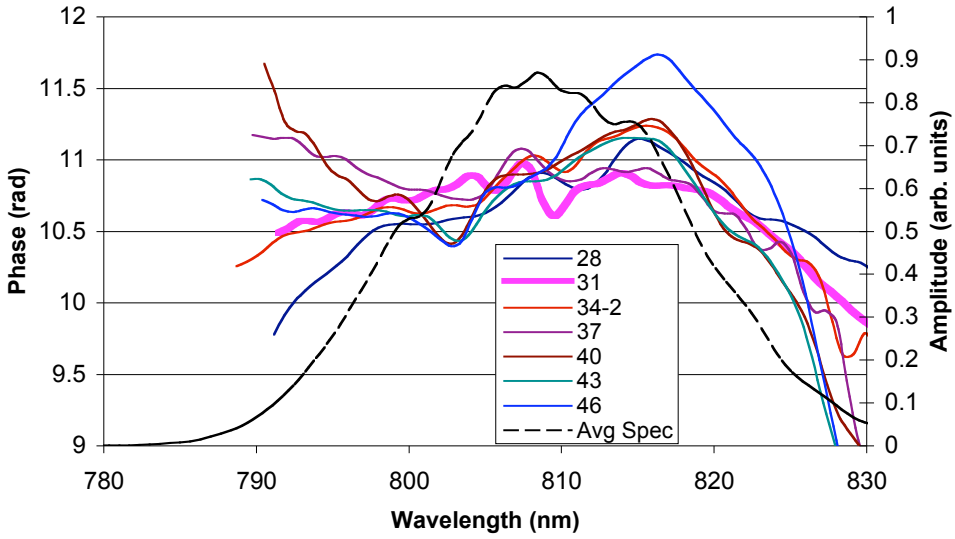

Figure 27 Spectral phase of compressed regenerative amplifier pulses as a function of round trips in the regenerative amplifier. 31 trips, the thick line, is the flattest of the 7 traces.

regenerative amplifier, adjusting the grating separation each time to minimize the pulse length. The results, shown in Figure 27, show that the optimal number of regenerative round trips with this compressor alignment. The downside of adding trips to the regenerative amplifier is that the output energy is significantly lower. With 9 round trips, the amplifier produces ~7 mJ. With 31 round trips, however, only ~800 μJ are produced. With the regenerative amplifier running with it's optimal number of round trips, the compressed pulse length is 80 fs, with a significant cubic phase.

2.2.3 Phase Comparison with a Standard Regenerative Amplifier

The first step in comparing the regenerative amplifier and OPCPA based systems is the measurement of the regenerative amplifier performance. The BBO crystals in the OPCPA stage are rotated away from the phase-matching axis so the regenerative amplifier beam and the pump beam can pass through them without mixing. This allows the to systems being compared to be as equivalent to each other as possible in terms of path length and material. Because the regenerative amplifier output is so low at the 31 round-trip setting, the beam size is reduced by a factor of two with a down-collimating telescope before going into the 4-pass amplifier. This will

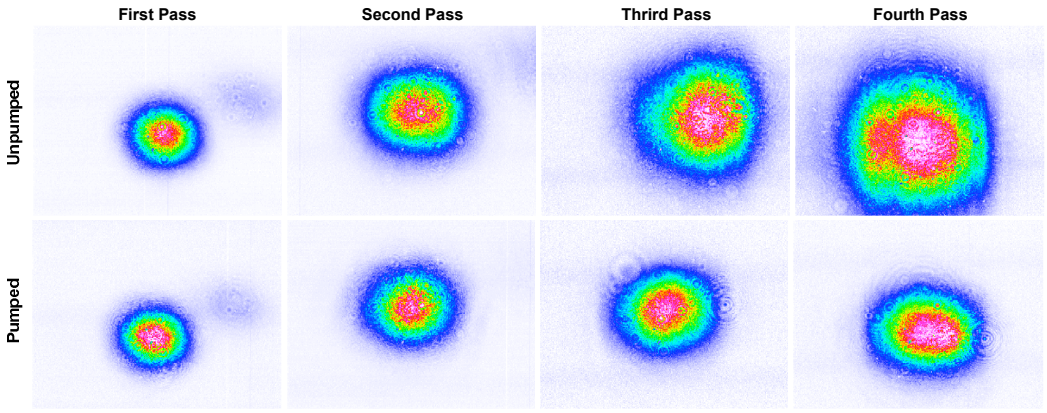

Figure 28 Beam profiles after each pass through the four pass. The seed beam is diverging going through the amplifier, but thermal lensing and gain guiding keep the amplified pulse close to collimated.

ensure all the regenerative amplifier light sees large gain in the Ti:Sapphire crystal. Figure 28 shows the unamplified and amplified beam profiles after each pass through the crystal. The input energy is 350 μJ in a 1.5 x 1.3 mm FWHM spot, and the energy after each pass is 1.3 mJ, 3.7 mJ, 9.5, mJ, and 18 mJ, respectively. The exit beam diameter is 2.5 x 1.7 mm FWHM. Because the seed light is so low in energy, the regenerative amplifier was returned to 9 round trips so the 4-pass could be seeded with 1 mJ of light. The output energy with both 1 mJ and 1.5 mJ input energy is 55 mJ, and the output energy drops as the seed drops below 1 mJ. This implies that the 4-pass amplifier is saturating at 55 mJ, giving a conversion efficiency from the pump laser of 36%. This low percentage is a result of the small seed profile relative to the pump profile that was used to maximize the under-saturated gain in the 31 round trip case.

The amplified regenerative amplifier light was sent to the compressor and the grating separation was adjusted to minimize the pulse length. Figure 29 shows the retrieved spectral and temporal profiles for four samples, showing the stability of the spectral phase, as well as the measured and retrieved GRENOUILLE traces of one of the samples. The measured pulse length is 61.2 fs, with a bandwidth of 15.76 nm which corresponds to a minimum pulse length of 60.4 fs, meaning the pulse is close to the transform limit.

After successful amplification and compression of the regenerative amplifier light, the OPCPA stage was activated. The seed beam at the exit of the OPCPA stage is shown in Figure 30a. As the gain was turned up, an unexpected effect was observed, as shown in Figure 30b. The first crystal, where the pump and seed beams are crossing in a vertical plane, amplifies light in a

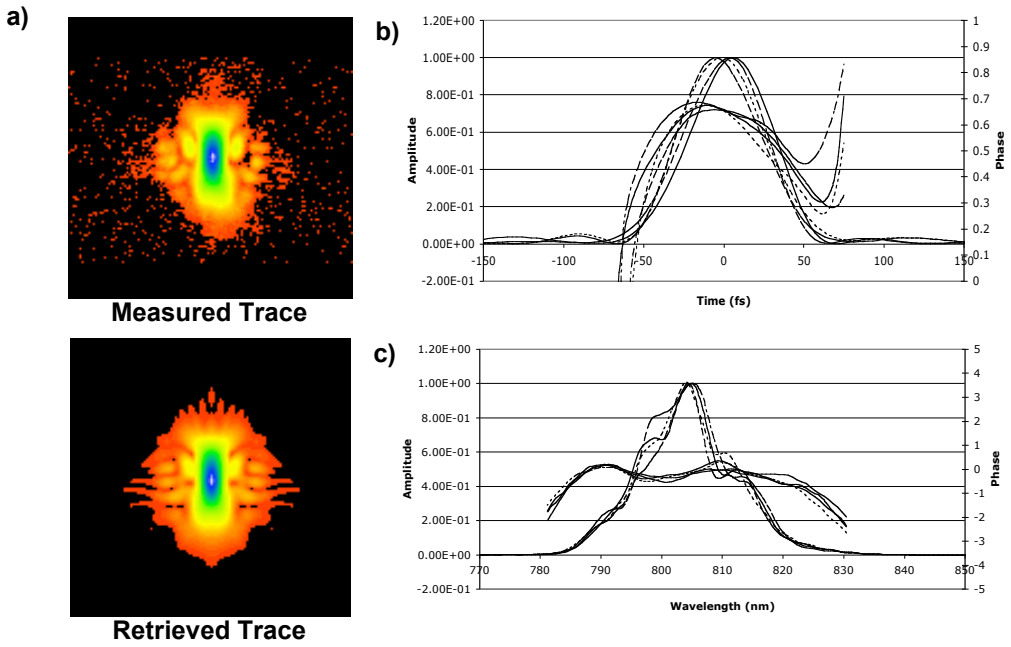

Figure 29 a) measured and retrieved GRENOUILLE traces of the amplified regenerative amplifier signal. b) retrieved temporal amplitude and phase. c) retrieved spectral amplitude and phase

long, narrow strip in the horizontal direction. As the crystal is rotated in the horizontal plane, this narrow strip moves up and down. Similarly, in the second crystal where the beams cross in the horizontal plane, the light is amplified in a long, narrow strip in the vertical direction, and as the crystal is rotated in the horizontal plane, this line moves left and right. It is possible that the divergence angle of the beam, going from a diameter of 0.8 mm to a diameter of 1.5 mm between the crystals exceeds the angular acceptance of the crystal, so the walk-off between the pump, signal, and idler beams is too great to allow amplification outside that narrow strip. This means that much of the seed light sees no gain, and a smaller seed pulse, with the full energy in the region that produces gain in both crystals, would be better for the system. With full gain, we get the profile shown in Figure 30c, where 2 nJ of seed energy has been amplified to 0.5 mJ, for a total gain of $10^{5.3}$, which is adequate for seeding the 4-pass stage.

The amplified beam from the OPCPA is considerably smaller than the seed signal was, and is also diverging. This beam is collimated with a 790 mm focal length lens. The beam profile going into the 4-pass amplifier is shown in Figure 30d, and Figure 30e shows the beam leaving the 4-pass amplifier with a final energy of 25 mJ. This beam is then sent to the compressor and

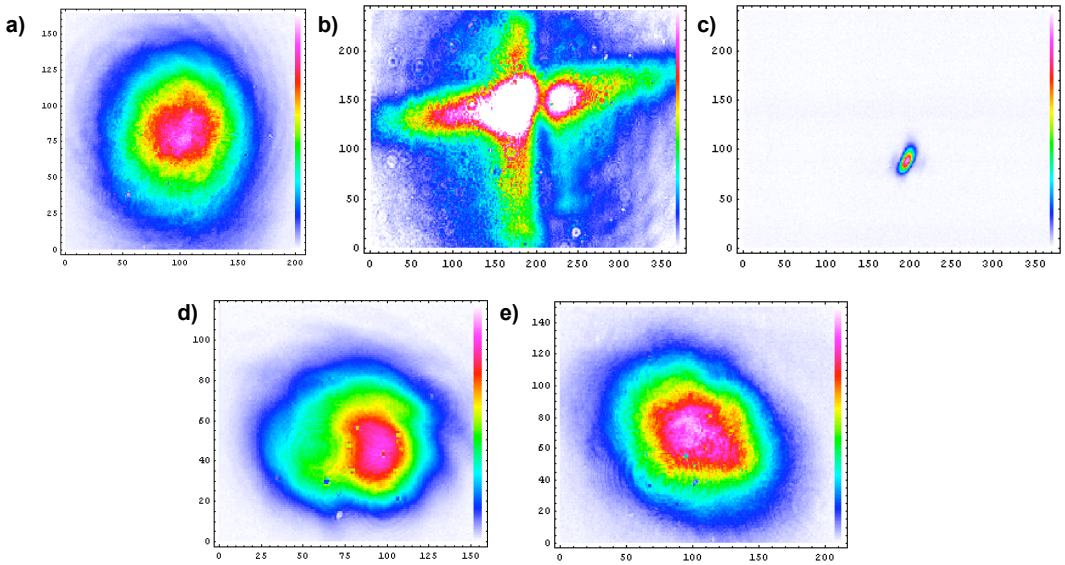

Figure 30 Profiles of the OPCPA system. a) seed profile at the output. b) small amount of gain, showing result of a phase-match error (see text). c) fully amplified OPCPA beam. d) OPCPA beam at 4-pass rod. e) 4-pass output with OPCPA seed.

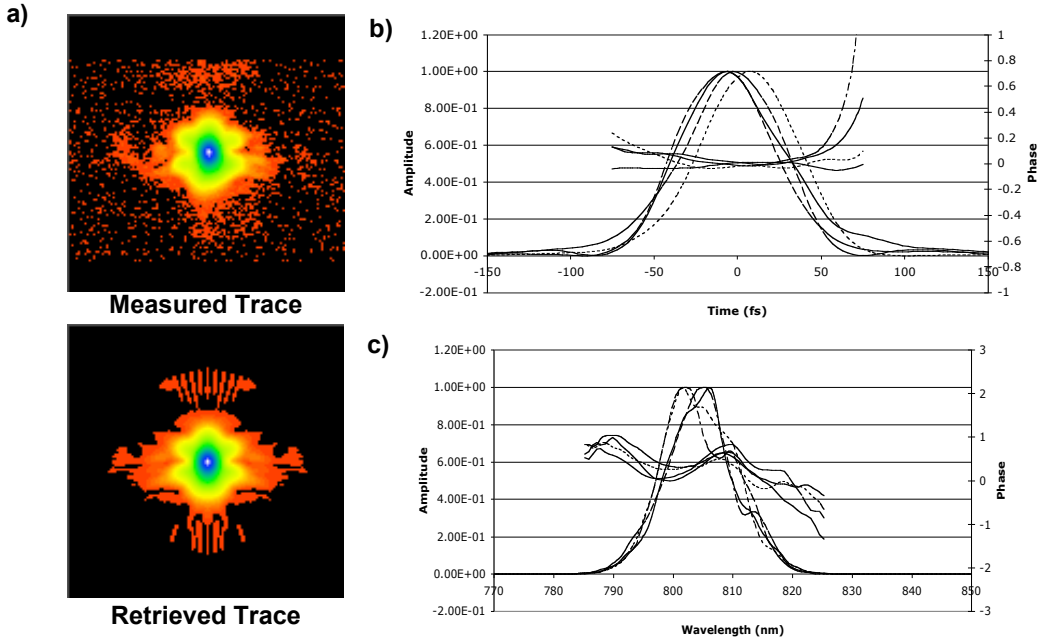

Figure 31 a) measured and retrieved GRENOUILLE traces of the amplified OPCPA signal. b) retrieved temporal amplitude and phase. c) retrieved spectral amplitude and phase

measured with the GRENOUILLE. The phase retrieval data is shown in Figure 31. The retrieved pulse width was 70 fs, and the retrieved bandwidth was 13.23 nm, which can support pulses as short as 71 fs. Again, this compressed pulse is near the transform limit.

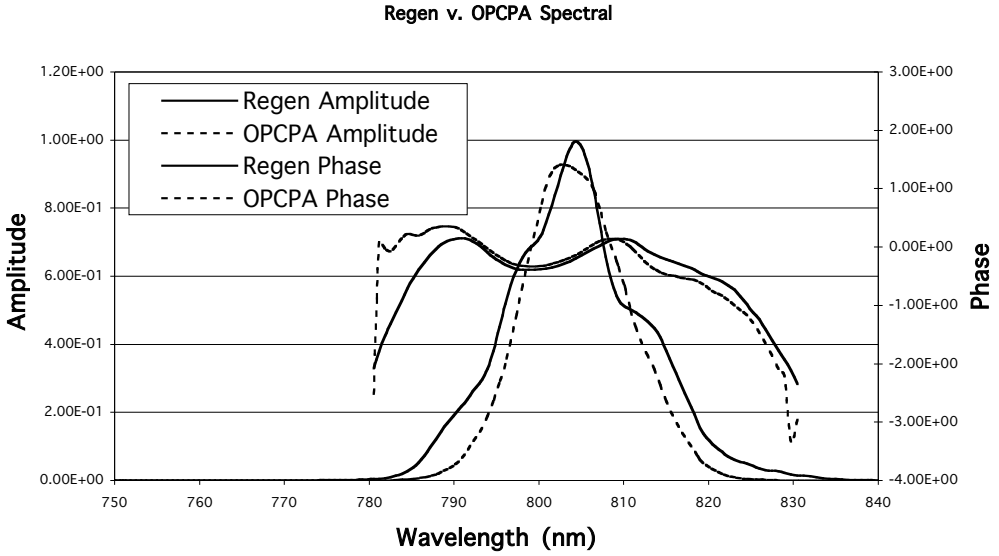

Figure 32 OPCPA and regenerative amplifier based systems spectral phase comparison.

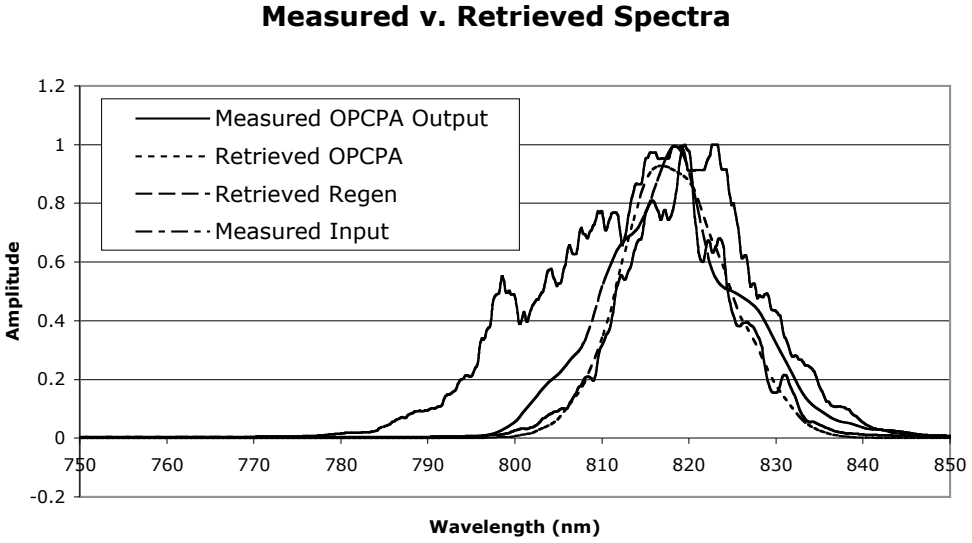

Figure 33 Input, measured, and retrieved spectra from the OPCPA and regenerative amplifier systems.

A direct comparison of the retrieved spectral phases of the OPCPA and regenerative amplifier signals is shown in Figure 32. The retrieved data shown are the averages of the data shown in Figure 29c and Figure 31c. The close similarity of the retrieved phases shows that no unusual, or uncompensatible, spectral phase is introduced by the OPCPA process.

Looking at Figure 33 shows that for both the regenerative amplifier and OPCPA light, the final spectrum is considerably narrower than what went into the system, a result of gain narrowing in the 4-pass crystal. Also, the total power was reduced, due partly to the large losses in the pump laser passing through the OPCPA stage, the low pump absorption of the Ti:Sapphire rod in the 4-pass, and the low seed energy. The fact that only 36% conversion efficiency in the saturated amplifier was observed indicates that the mode seeding the 4-pass might be less than optimal.

The improvements that could be made on this system include: changing the divergence angle of the seed beam in the OPCPA to reduce the effect observed in Figure 30b and improve the OPCPA gain, adjusting the OPCPA alignment to maximize the output bandwidth, and improving the mode-matching into the 4-pass amplifier. A potential upgrade would be to increase the pump power in the 4-pass by sending some green light around the OPCPA stage (the damage threshold of the dichroic mirrors limits the pump fluence) or by increasing the pump size in the OPCPA crystals (increasing the energy while keeping the same fluence), and try to get higher gain. However, the HCPA system has been demonstrated to perform as well as a regenerative amplifier, while not requiring any electrooptical components, and using a much less complex set-up.

Chapter 3. Electron Sources

The second half of a Compton scattering source, complementing the laser of Chapter 2, is the relativistic electron beam. Since the x-ray beam that is produced is strongly dependant on the electron beam parameters, as emphasized in Section 1.2.2.3, it is imperative to have a high quality electron beam. Simply looking in terms of the most relevant figure of merit for an x-ray source, the brightness [in units of photons·s^{-1}·mm^{-2}·$mrad^{-2}$·(0.1 % bandwidth)$^{-1}$], demonstrates this. Brightness increases with smaller spot size, so a tight focus is desired (the "mm^{-2}" term). However, because of the low Thomson scattering cross-section (σ_T = 6.65 x10^{-25} cm^2), a high charge is necessary within that small focal spot to get the scattered photon number up (the "photon" term). It is also important to have a short x-ray pulse both to maximize the brightness (the "s^{-1}" term) and to make time-resolved measurements with the x-rays. Finally, the analysis in Section 1.2.2.3 shows that the divergence of the electrons at the focus dominates the relative bandwidth of the x-rays (the "(0.1% bandwidth)$^{-1}$" term), as well as contributing to the divergence of the source (the "$mrad^{-2}$" term). This means then that low emittance is required. The optimal means to produce such an electron bunch is with a device known as an rf photoinjector.

3.1 RF Photoinjectors

Compact, high-gradient (> 100 MeV/m) rf photoinjectors capable of producing relativistic (> 5 MeV) electron beams with extremely low emittance (< 1 π-mm mrad), high charge (1 nC), and subpicosecond duration, are currently being developed[79-83] for a variety of applications ranging from the Next Linear Collider (NLC) to compact, pre-bunched free-electron masers[84].

3.1.1 Some Beam Physics Basics

Before the benefits of photoinjectors are explained, some introductory beam physics is required to understand the concept of *emittance*, which is the main indicator of the quality of an electron beam. The linearized equation of motion for an electron in a beamline is[85]

$$u''(s) + k(s)u(s) = 0 \tag{31}$$

where $u(s)$ represents the particles displacement from the from the ideal particle path in either the x or the y direction, and s is distance along that ideal particle path. For a beamline with no bends (i.e. a straight linear accelerator, which is what is of interest here), s is equivalent to z and u is equivalent to x or y. The function $k(s)$ represents the beam optics (dipole, quadrupoles, etc.) along the beamline. Since what is of interest here is an understanding of the nature of an electron beam focus, where the magnetic fields are zero, the details of $k(s)$ are not important. A general solution to (31) is

$$u(s) = \sqrt{\varepsilon}\sqrt{\beta(s)}\cos\left[\phi(s) - \phi_0\right] \tag{32}$$

subject to the two conditions on β and ϕ (found by substituting (32) into (31))

$$\tfrac{1}{2}\left(\beta\beta'' - \tfrac{1}{2}\beta'^2\right) - \beta^2\phi'^2 + \beta^2 k = 0$$
$$\beta\beta' + \beta\beta\phi' = 0$$

Defining two auxiliary functions

$$\alpha(s) = -\frac{1}{2}\beta'(s)$$
$$\gamma(s) = \frac{1 + \alpha(s)^2}{\beta(s)} \tag{33}$$

we can use (32) and its derivative to eliminate the phase function $\phi(s)$, leaving a differential equation in β that yields a constant of the motion,

$$\gamma u^2 + 2\alpha uu' + \beta u'^2 = \varepsilon, \tag{34}$$

known as the Courant–Snyder invariant. This equation describes an ellipse in u-u' space with area $\pi\varepsilon$. The particle under study travels down the beamline tracing this ellipse (according to the value of $\phi(s)$), while the shape of the ellipse is evolving according to the values of $\beta(s)$, $\alpha(s)$, and $\gamma(s)$, which are commonly known as the "betatron functions".

Although this specifically describes the motion of a single particle, classical mechanics shows it is applicable to the beam as a whole as well. $u'(s)$ can be related directly to the transverse and longitudinal momentum of the particle via

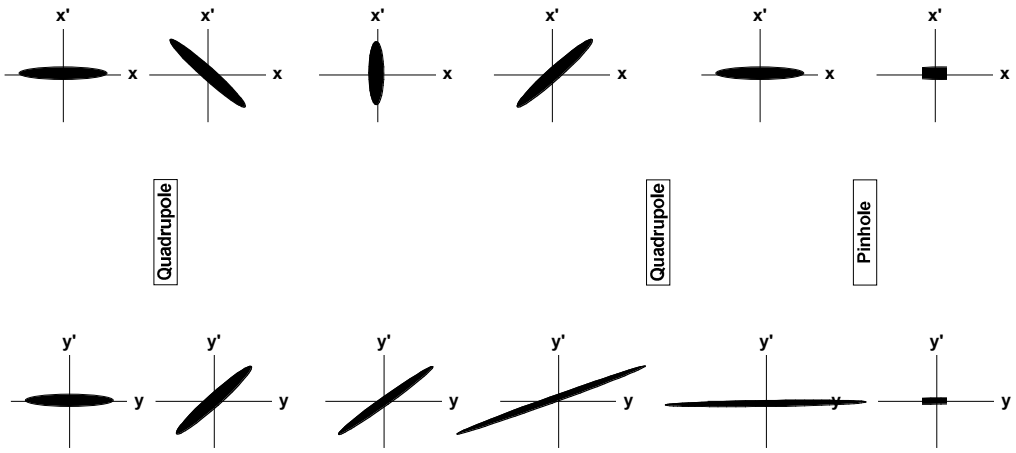

Figure 34 A schematic example of the meaning of emittance. The upper and lower rows of plots show the x and y phase spaces as a function of position along the sample beamline shown in the middle. The area of the ellipses are the x and y emittance. The area is constant until the beam is clipped (charge is removed).

$$u'(s) \equiv \frac{du}{ds} = \frac{\frac{du}{dt}}{\frac{ds}{dt}} = \frac{p_u}{p_z}, \tag{35}$$

where p_u is the particle's transverse momentum and p_s is the particle's longitudinal momentum. This is therefore an ellipse in phase space as well. Liouville's theorem, which requires phase space density remain constant under conservative forces, tells us that if an ellipse is chosen that includes all the particles, it will always include all the particles. That ellipse can provide a metric for the phase space of the beam as a whole. The value ε for this ellipse is the beam "emittance", and gives a general indicator of the beam quality. Practically, the emittance is usually presented in terms of an rms value, given by

$$\varepsilon_x = \frac{1}{N}\sqrt{\left(\sum_{i=1}^{N} x_i^2\right)\left(\sum_{i=1}^{N} x_i'^2\right) - \left(\sum_{i=1}^{N} x_i x_i'\right)^2}$$

Figure 34 gives an illustration of this concept of phase space and constant emittance. We start with a "collimated" beam, where the spread in transverse momentum is low and the size is large. A quadrupole magnet then adds a position dependant momentum to the bunch: in the x dimension, particles on the positive side get a negative momentum, and the particles on the negative side get a positive momentum; in the y dimension, the opposite happens with particles with a positive position getting positive momentum and negative position getting a negative

momentum. As this beam propagates, the momentum spread causes the size of the bunch in x to shrink to a focus, then reexpand, while the y size simply expands. A second quadrupole undoes the momentum kick of the first quadrupole. The area of the phase space ellipses shown in the figures is the emittance in the x and y axes. Note that the area of the ellipse stays the same, until the beam is clipped by the pinhole; if charge isn't conserved, neither is emittance – this is one way to improve beam quality, at the expense of charge. Generally, smaller emittance beams are "better", in the sense that they make smaller spots without as much divergence. The benefit of a low emittance can be seen for a Thomson source, which requires both a small spot size and a low divergence to maximize brightness.

Because of the relationship between $u'(s)$ and momentum in (35), if an electron beam is accelerated so p_s increases while p_u remains (ideally) the same, the emittance of the electron beam actually shrinks because $u'(s)$ shrinks. Therefore, it is common to define a normalized emittance

$$\varepsilon_{nx} = \beta\gamma\varepsilon_x$$

which is in general conserved even during acceleration. This normalized emittance is the general figure of merit for the quality of a particle beam.

Returning to the betatron functions, their evolution depends on the magnetic field parameters at that point in space. In a drift section, where there is no magnetic field, they evolve as[85]

$$\begin{aligned} \beta(s) &= \beta_0 - 2\alpha_0 s + \gamma_0 s^2 \\ \alpha(s) &= \alpha_0 - \gamma_0 s \\ \gamma(s) &= \gamma_0 \end{aligned} \tag{36}$$

where β_0, α_0, and γ_0 are the respective values at the starting point s=0. By always taking the maximum spatial extent of the beam phase-space ellipse, a beam envelope can be mapped out with

$$r(s) = \sqrt{\varepsilon}\sqrt{\beta(s)} \tag{37}$$

We are now ready to quantitatively discuss the focus of the beam. At the focal point, $s_f \equiv 0$,

$$\sigma \equiv r(0) = \sqrt{\varepsilon}\sqrt{\beta(0)} \quad \beta_0 \equiv \beta(0) = \frac{\sigma^2}{\varepsilon}$$

where σ is the rms beam size at the focus. Because the beam is at a focus, $r(s)$ is, by definition, at a minimum, and by extension β is as well. Therefore $\beta' = d\beta/ds = 0$. Using (33) then, $\alpha_0 = 0$ and $\gamma_0 = 1/\beta_0$. Plugging these three values into the first equation of (36) gives

$$\beta(s) = \beta_0 + \frac{s^2}{\beta_0}$$

which shows how the beam envelope propagates near a focus. To define the length of the focal region, in a parallel to the Rayleigh range of a laser, we choose to look at the distance in which the beam area grows by a factor of 2, or the radius grows by a factor of $\sqrt{2}$. So:

$$\begin{aligned} r(s_l) &= \sqrt{2}\sigma \\ \sqrt{\varepsilon}\sqrt{\beta(s_l)} &= \sqrt{2}\sqrt{\varepsilon}\sqrt{\beta_0} \\ \beta(s_l) &= 2\beta_0 \\ \beta_0 + \frac{s_l^2}{\beta_0} &= 2\beta_0 \\ s_l &= \beta_0 \end{aligned}$$

So the value of the betatron function at the focus gives a measure of the length of a focal region, which can be used to help select the interaction focusing design.

In summary, for a Thomson interaction the three relevant beam propagation parameters are the emittance, ε, the focal spot size, σ, and the value of the betatron function $\beta(s)$ at the focal point, β_0, which will be referred to here simply as the "beta function". These all directly parallel laser parameters. The laser propagation equation from Chapter 2 is

$$w(z) = w_0\sqrt{1 + \left(\frac{M^2 z}{\pi w_0^2}\right)^2} \tag{30}$$

While the electron beam propagation equation is

$$r(z) = \beta_0\sqrt{1 + \left(\frac{z}{\beta_0}\right)^2}.$$

So, we can make the equivalences:

$w_0 \leftrightarrow \beta_0$	spot size
$\beta_0 \leftrightarrow z_r$	focus range
$\varepsilon \leftrightarrow \frac{\lambda M^2}{\pi}$	beam quality

bearing in mind when looking at quoted numbers that laser beam values generally are quoted in $1/e^2$ radii and electron beams in rms values.

3.1.2 Thermionic Cathodes v. Photoinjectors

Traditionally, the electron source for linear accelerators has been a thermionic cathode. This device operates by heating a cathode material (e. g. tungsten) to allow electrons to escape, and applying a DC electric field to accelerate the freed electrons. Conversely, in an rf photoinjector system, the photoelectric effect is used to liberate the electrons from the cathode, and an rf field is used to accelerate them. The question is which source to use for a Thomson scattering system; the answer turns out to be fairly straightforward: photoinjectors.

The first feature to examine is pulse length. One of the terms in the x-ray brightness is s^{-1}, i.e. the x-ray pulse length. The duration of the x-ray burst is directly correlated to the x-ray bunch length in a head-on scattering geometry. Therefore, a minimal electron bunch length is required. In a thermionic system, electrons are produced and accelerated for as long as the DC voltage is applied, which can only be as short as a few ns (it is limited by the capacitance of the cathode and grid). In a photoinjector, electrons are only produced for the duration of the uv laser pulse, which can be as short as a few tens of fs. There are tricks that can be used to shorten the bunch length of a thermionic beam, such as using buncher cavities or magnetic chicanes to compress the bunch length, but both these systems have adverse effects on the electron transverse emittance and energy spread, which is bad for a Thomson source, as discussed below.

The next important parameter is the beam emittance. As was discussed in section 1.2.2.2, the emittance of the beam has a significant impact on the produced x-ray pulse. Emittance comes into play in the photoinjector decision most directly due to space-charge considerations. Naturally, a bunch of electrons sitting in vacuum is not going to want to stay in a bunch; the electrostatic fields between the electrons causes a repulsive force, which then increases the emittance by increasing the size and momentum spread of the bunch. This isn't a problem with relativistic beams for the parameter space relevant for this experiment because at relativistic energies the electrons effectively have more mass, so the resultant acceleration from the force is less (in the lab frame), or the electrons are much further apart and therefore the repulsive forces

are much weaker (in a frame co-moving with the bunch; either viewpoint works). Therefore, to keep emittance to a minimum, it is important to accelerate the bunch as quickly as possible to relativistic energies. In a thermionic gun, the accelerating voltage is limited to less than 1 MV. In a photoinjector, accelerating gradients of over 100 MV/m are achievable, allowing rapid acceleration of the bunch before space-charge-induced emittance growth becomes significant. Also, because of this large gradient, much higher peak currents can be generated, again a benefit for Thomson scattering with the very low cross section.

The fact that the electron bunch in a photoinjector is coupled to the laser pulse allows for tight synchronization between the injection of the electrons and the phase of the accelerating rf. At 2.86 GHz (S-Band), 1° of rf phase is 0.97 ps. A laser pulse of this length is easy to achieve, allowing all the electrons to see the same accelerating gradient. This minimizes the overall energy spread of the beam, giving photoinjectors another benefit over thermionic beams. Unrelated to beam quality considerations, the laser synchronization to the electrons during their production at the front end of the linac allows easier synchronization of the laser and electron beam at the scattering end of the accelerator (one of the most difficult parts of operating a Thomson source) by using coupled laser systems for the photocathode and scattering light as discussed in Section 2.1.

Photoinjectors of course have some downsides; generally the total amount of charge available is limited by the quantum efficiency of the cathode material, coupled with its laser damage threshold. More significantly however is that a photoinjector requires a dedicated uv laser system to generate the electrons, which makes it exceedingly more complicated than to operate than a thermionic cathode. However, the performance required for a bright Thomson scattering source dictates the choice of a photoinjector for electron beam production.

3.1.3 Theory of Operation

The concept behind the operation of an rf photoinjector is relatively straightforward. Both the S-Band gun of Section 0 and the X-Band gun of Section 3.3 are based on having one full cell, half an rf wavelength long, and one partial cell (approximately one quarter of an rf wavelength). In the X-Band gun, it's based on a 1.5 cell design from Brookhaven National

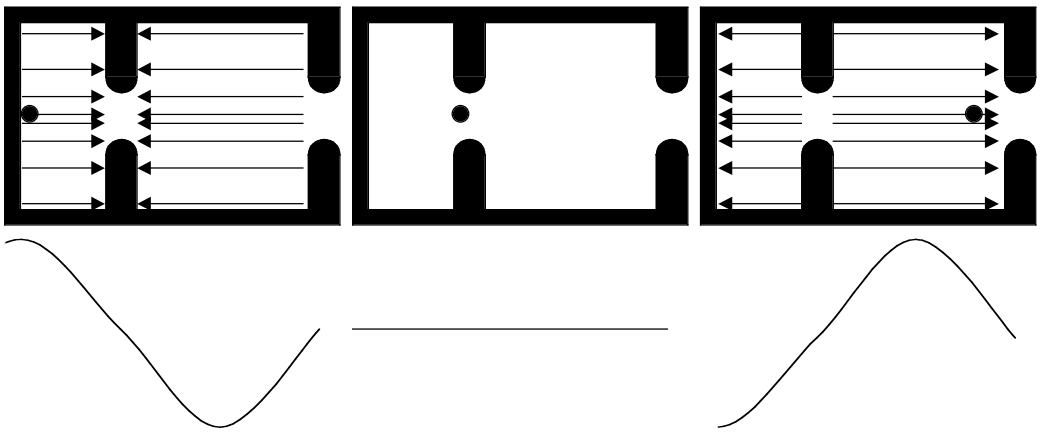

Figure 35 A diagram showing how an electron bunch is accelerated in a 1.5 cell standing wave rf photoinjector. Three different times are shown. The dot is the electron bunch, the lines represent the electric field in the gun, and the bottom row shows the electric field strength as a function of axial position in the gun.

Laboratory and UCLA[86], scaled down to run with a higher rf frequency. For the S-Band gun, it's a revised version of the same design with a slightly larger first cell (a 1.6 cell gun)[79]. In either case, however, the same general beam physics applies.

Figure 35 shows how the acceleration is accomplished. RF power is coupled into the gun cavity in what is referred to as "π-mode", where the phase of the rf fields in the two cells are exactly 180° apart (as opposed to the "0-mode", where the two cells run in the same phase). A pulse of uv light, with an energy just exceeding the work function of the cathode material (copper in both guns discussed here), strikes the cathode and frees electrons. These electrons see the electric component of the rf field, as shown in Figure 35, and are accelerated. The timing of the arrival of the uv pulse is set so that the electron bunch reaches the aperture between the two cavities as the field drops to zero, and the sign of the fields is changing. This minimizes the effects of field nonlinearities in the region of the aperture. Now the electron is in the second cell, and the sign of the electric field has changed so this field can accelerate the electron further. More full cells can be added in the same way to optimize the beam parameters for specific applications. For our purposes, and since we already have an rf accelerator to boost the energy further, one full cell is sufficient.

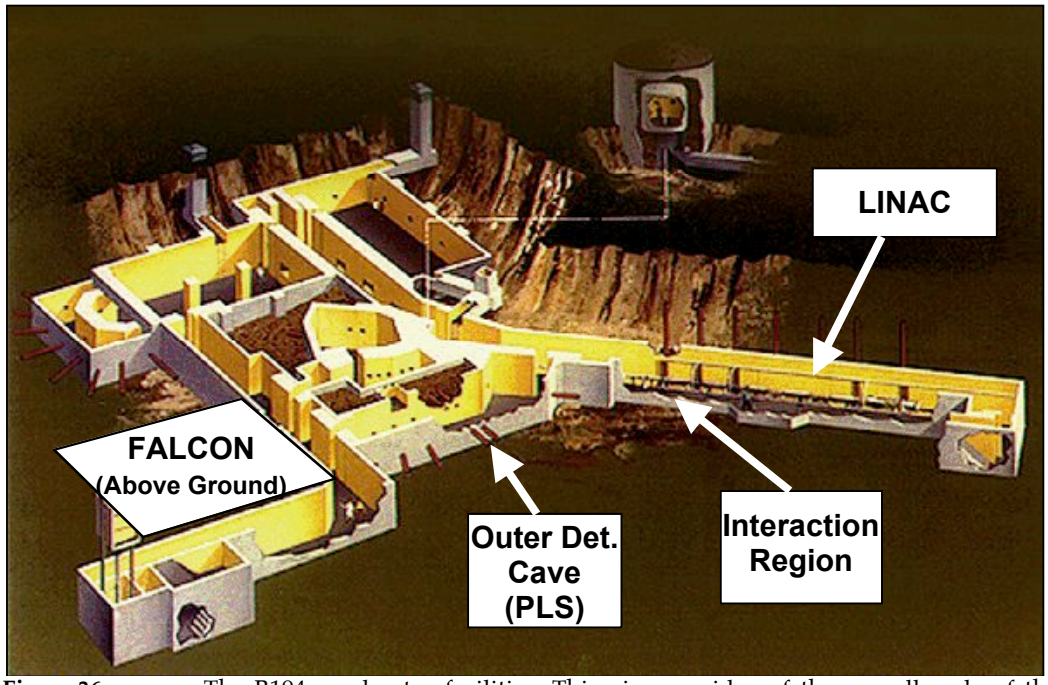

Figure 36 The B194 accelerator facilities. This gives an idea of the overall scale of the system, and the long lengths needed to transport the laser beam.

3.2 The PLEIADES Linear Accelerator Facility

The electron beam that is used for these experiments is produced at the LLNL 100-MeV linear accelerator[87] (linac), which has been substantially upgraded to meet our emittance and timing jitter requirements, as discussed in Section 3.2.2, with the installation of a new photoinjector on the accelerator as an alternative to the preexisting thermionic injector. Installation of a photoinjector required significant modifications to the existing linac beamline, and the installation of a uv laser system to drive the photocathode.

3.2.1 The Photoinjector Laser System

The Photoinjector Laser System (PLS) was installed as close as practical to the linear accelerator, in an area referred to as the "Outer Detector Cave" (see Figure 36). This area was designed to hold detection equipment for nuclear physics experiments that were part of the original uses of this accelerator system. This area was not temperature controlled (with swings of several degrees during the day, and several tens of degrees over the course of the year) and very dusty, both of which are unacceptable for laser operation. To correct this, a temperature

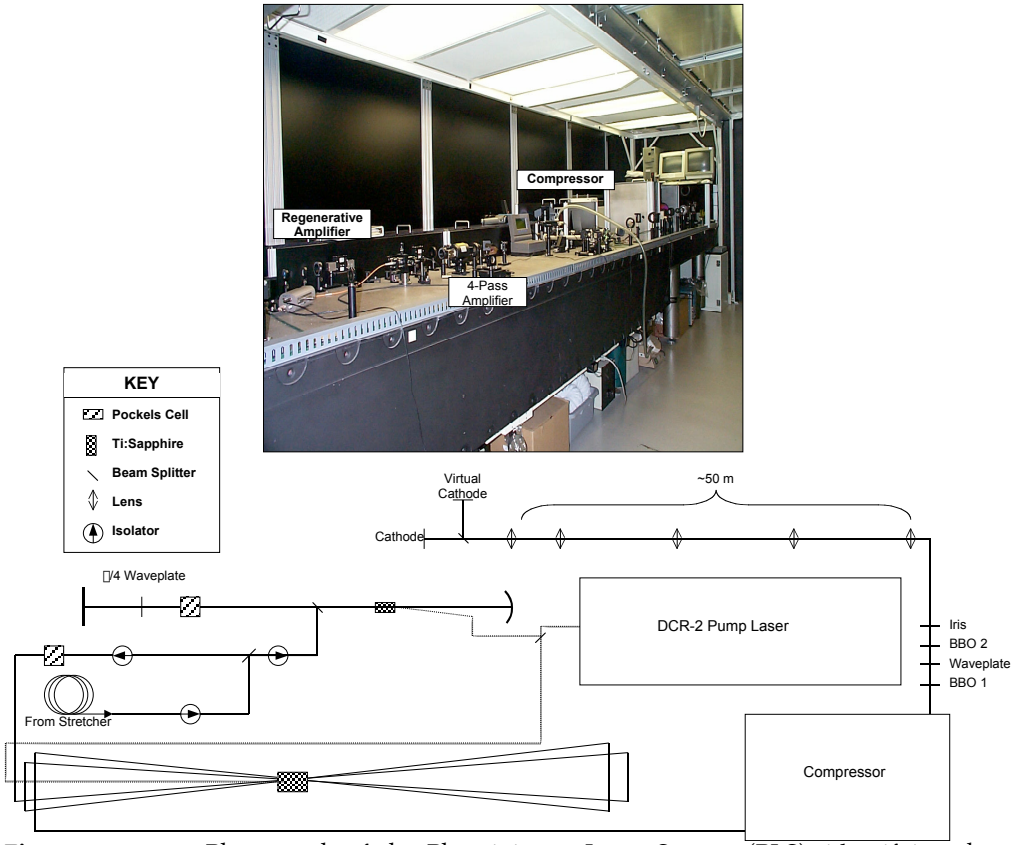

Figure 37 Photograph of the Photoinjector Laser System (PLS), identifying the main components, and the general layout of the PLS. Not all components are shown, and the drawing is not to scale

controlled hutch was built to enclose the laser system, and HEPA filters added to help minimize the air particulates. This structure has allowed successful operation of the PLS laser in the adverse accelerator environment.

3.2.1.1 Amplification and Relay

Figure 37 shows the general layout of the PLS. The PLS is seeded through a 50-meter, single-mode fiber with 30% of the light from the main oscillator pulse, as discussed in Section2.1.1. Care must be used when propagating a broadband laser pulse through this much material; this is addressed in Section 3.2.1.2. After coupling and transport losses, the seed light has an average power of 7.3 mW, or 90 pJ per pulse, which is coupled into a linear regenerative amplifier cavity. The Ti:Sapphire crystal in this amplifier is pumped with 50 mJ of 532-nm light from a SpectraPhysics DCR-2 laser. The end mirror leakage of this amplifier is monitored with a

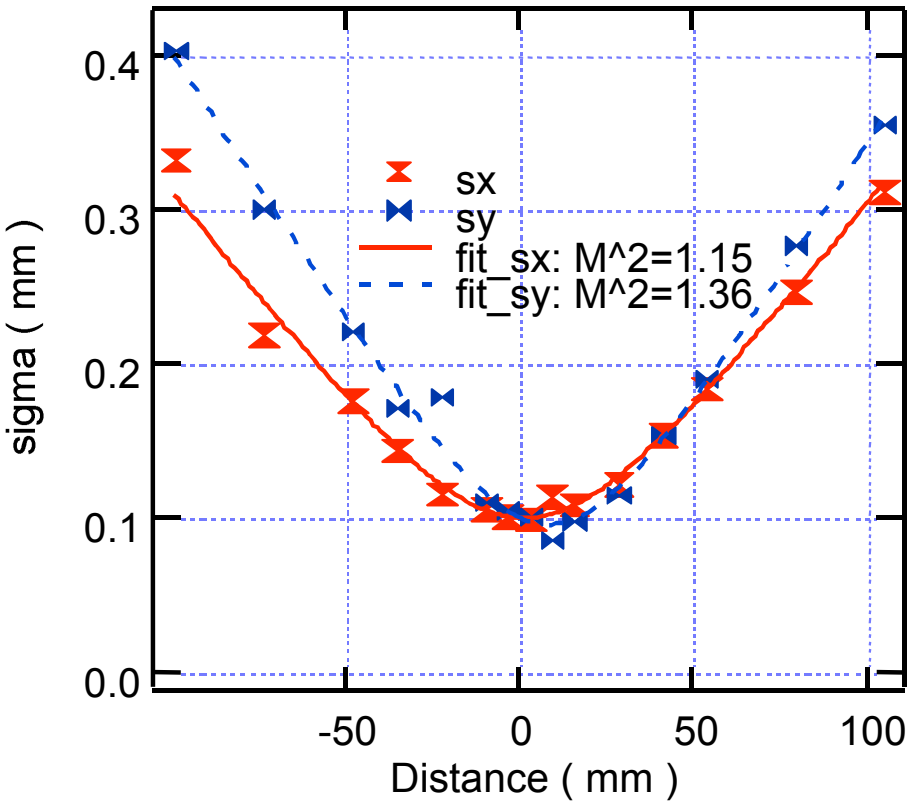

Figure 38 M^2 measurement of the PLS laser.

fast photodiode, which provides the trigger timing for the streak camera systems discussed in Sections 3.2.1.2 and 4.2. This system produces 5.9 mJ ir pulses at 10 Hz. Following the regenerative amplifier is a bow-tie configuration 4-pass power amplifier, similar to the two discussed for the FALCON system in Section 2.1.2. The Ti:Sapphire crystal is pumped with the 280 mJ of laser light from the DCR-2 that is not sent to the regenerative amplifier, and amplifies the cavity output up to the 90 mJ level. This 4-pass amplifier has a pointing and centering system to align the light entering it, as discussed in Section 2.1.2 The measured M^2 of the laser is 1.15 in the *x* axis and 1.36 in the *y* axis, as shown in Figure 38.

The light from the 4-pass is then sent into the pulse compressor, which is discussed more fully in the next section. Following compression, the pulse is frequency-doubled in a Type I BBO crystal, then tripled in a second Type I BBO crystal to 269 nm. A waveplate is used between the harmonic crystals that rotates the polarization of the second harmonic 90° while leaving the fundamental in the same polarization to set up the sum-frequency mixing to get 3 light.

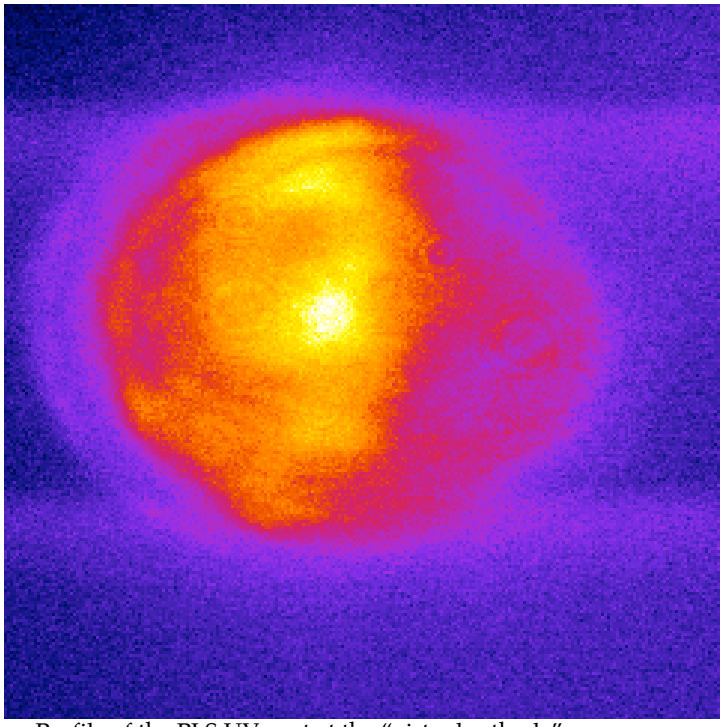

Figure 39 Profile of the PLS UV spot at the "virtual cathode"

Generally, about 1.2 mJ of uv light is available; however, to prevent damage to the cathode in the photoinjector, the system is often turned down to provide only about 380 μJ of light at the tripler output. This uv pulse is clipped with an aperture to a diameter of 2 mm to provide a hard-edged uv spot, which improves the emittance of the photoinjector. The aperture plane is relay imaged ~50 m to the photoinjector cathode. A small quantity of the uv light is extracted from the beam via an uncoated wedge, and the profile and energy are monitored continuously at the "virtual cathode", which is a plane the same distance from the final lens as the photoinjector cathode. An image of the UV spot is shown in Figure 39

3.2.1.2 Compression

As mentioned in the previous section, propagating the laser pulse through 50 meters of optical fiber poses a problem for the recompression of the laser pulse to its Fourier transform limit. This comes from residual cubic phase from the fiber that is uncompensated in the compressor. The spectral phase can be expanded in powers of as

$$\begin{aligned}\phi(\omega) &= \phi(\omega_0) + \frac{1}{1!}\frac{d\phi(\omega)}{d\omega}\bigg|_{\omega=\omega_0} + \frac{1}{2!}\frac{d^2\phi(\omega)}{d\omega^2}\bigg|_{\omega=\omega_0} + \frac{1}{3!}\frac{d^3\phi(\omega)}{d\omega^3}\bigg|_{\omega=\omega_0} + \cdots \\ &= \phi^{(0)} + \phi^{(1)} + \phi^{(2)} + \phi^{(3)} + \cdots\end{aligned} \tag{38}$$

where the derivative terms correspond to what are often called the linear, quadratic, cubic, etc. phase terms. For an ideal transform-limited pulse, the spectral phase should be flat; i.e., not a function of frequency. This means all the terms beyond the first one in (38) should go to zero. In practice, making all the terms go to zero is nearly impossible, but with careful design of the stretcher and compressor, it is generally possible to minimize the values of up to the quartic phase.

A problem in trying to flatten the spectral phase occurs when the amount of material in the system becomes too large. Following Kane[88], the phase function of dispersive material is given by

$$\phi(\omega) = \frac{n(\omega)L\omega}{c}$$

with L being the length of the material. Taking the ratio of the cubic phase to the magnitude of the quadratic phase gives

$$\frac{\phi^{(3)}}{\left|\phi^{(2)}\right|} = \left(\frac{\omega}{6c}\right)\left[3 + \omega\frac{d^3n}{d\omega^3}\left(\frac{d^2n}{d\omega^2}\right)^{-1}\right]$$

Similarly, for a standard grating pair compressor the phase is

$$\phi(\omega) = \frac{\omega}{c}G\cos\theta_d$$

with G being the perpendicular grating separation and θ_d being the diffraction angle (relative to the grating normal). Again taking the ratio of cubic to quadratic phases, we get

$$\frac{\phi^{(3)}}{\left|\phi^{(2)}\right|} = \frac{\omega}{2c}\left(\frac{1+\sin\theta_d\sin\theta_i}{\cos^2\theta_d}\right) \tag{39}$$

For a fused silica fiber (note that waveguide dispersion effects are being neglected), we can use the Sellmeir equation to calculate the dispersion[89]:

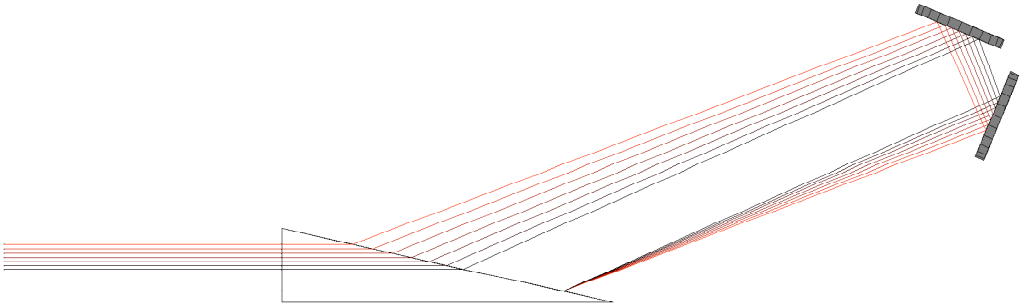

Figure 40 Layout of a single-grism pulse compressor. A roof mirror would typically be used to change the beam height and return the beam along the same path to recombine the different frequencies spatially.

$$n(\lambda) = \sqrt{1 + \frac{B_1 \lambda^2}{\lambda^2 - C_1} + \frac{B_2 \lambda^2}{\lambda^2 - C_2} + \frac{B_3 \lambda^2}{\lambda^2 - C_3}}$$

$$B_1 = 6.961663 \cdot 10^{-1} \qquad B_2 = 4.076426 \cdot 10^{-1} \qquad B_3 = 8.974794 \cdot 10^{-1}$$
$$C_1 = 4.67914826 \cdot 10^{-3} \qquad C_2 = 1.35120631 \cdot 10^{-2} \qquad C_3 = 9.79340025 \cdot 10^{1}$$
$$(\lambda \text{ in } \mu\text{m})$$

which gives a ratio of

$$\frac{\phi^{(3)}}{\left|\phi^{(2)}\right|} = 0.27187 \text{ fs}$$

for 820 nm light. Note from the form of (39) that this term will always be positive. This means that the compressor will not be able to compensate for the cubic phase of the material. To properly compensate for both the quadratic and cubic phases, the ratio in (39) must be -0.27187 fs.

A solution to this is the use of a grism pair[88]. A "grism" is a transmission grating written onto the face of a prism, as shown in Figure 40. The addition of a material with a non-unitary index of refraction changes (39) to

$$\frac{\phi^{(3)}}{\left|\phi^{(2)}\right|} = \frac{\lambda}{2\pi c}\left[\frac{1 + n_p \sin\theta_d \sin\theta_i}{\cos^2\theta_d}\right] \tag{40}$$

where n_p is the index of refraction of the prism material. Now, this term is no longer obligated to be positive, and careful choice of diffraction angle will allow for cubic compensation of the fiber. Specifically, if BK7 is used for the prism, and an incidence angle of 77.4° is used, (40) gives us

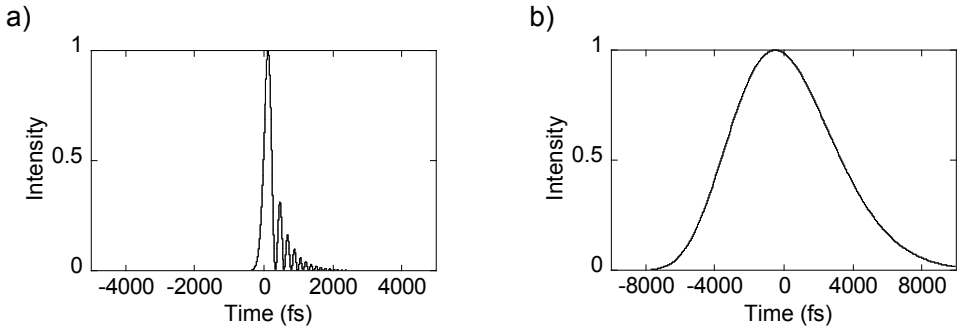

Figure 41 Temporal profiles of compressed pulses sent through 50 m of fused silica fiber. a) fully compressed (0 fs^2 quadratic phase), showing the limiting effects of the cubic phase ($6 \cdot 10^6$ fs^3). b) partially compressed to 7 ps ($-3 \cdot 10^5$ fs^2 quadratic phase) with the same cubic error.

$$\frac{\beta^{(3)}}{\left|\beta^{(2)}\right|} = 0.27057 \text{ fs},$$

which almost exactly compensates for both the cubic and quadratic phase added by the fiber. To exactly cancel the cubic phase, the grating separation will have to be 45.97 cm which, given our laser bandwidth, will require a 4" short side on the grism, and an 18.3" grating length, which was not available to us. Fortunately, in the end the need for this was avoided by electron beam considerations.

Simulations of the electron beam in the photoinjector show that the best quality beams (in terms of energy spread and emittance) occur when using laser pulses with pulse lengths of a few ps to produce electrons from the photocathode. The lower limit is a result of the Coulomb repulsion of the electrons, which are initially created at rest. As the laser pulse gets shorter, the electron density increases until the repulsive forces start overwhelming the accelerating forces and causes the beam to spread and emittance to grow. The upper limit is set by the frequency of the accelerating rf. If the pulse is longer than a few degrees of rf phase, there is an increase in the energy spread of the beam, as electrons see different accelerating gradients. As the pulse continues to get longer, it eventually starts releasing electrons that aren't accelerated at all, wasting uv energy. Additionally, the electron, and therefore the x-ray, pulse duration is determined largely by the uv pulse length, so that is also a consideration in selecting the pulse length.

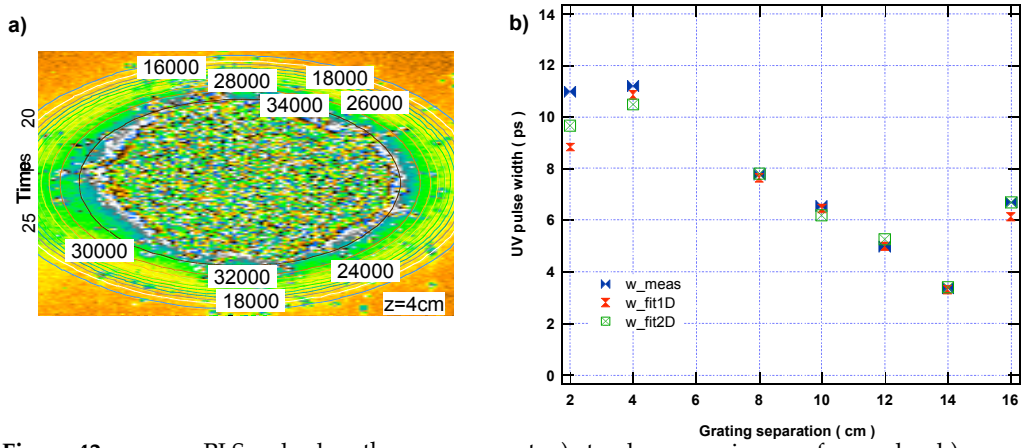

Figure 42 PLS pulse length measurement. a) streak camera image of uv pulse. b) uv pulse width as a function of compressor grating separation The pulse widths at each data point are determined using a 2D Gaussian fit (w_fit2D), a 1D Gaussian fit to a lineout of the image (w_fit1D) and the width at half the average value of the top of the lineout of the pulse (w_meas).

To create this few-picosecond pulse, the PLS laser is not fully compressed to the transform limit, leaving a slightly chirped pulse. Because the pulse is not being fully compressed, the quadratic phase dominates the residual cubic phase from the fiber. Figure 41a shows a fully compressed pulse, with the residual cubic error from the fiber. The cubic phase results in a train of pulses. Figure 41b shows the same pulse, but compressed to only 7 ps. The cubic phase leads to an asymmetry on the pulse shape, but that is a relatively insignificant effect for the purposes of the electron beam.

The pulse is left at a pulse length of approximately 7 ps. A streak camera with 300 fs resolution[90] was used to measure the pulse duration as a function of grating separation. Figure 42a shows a streak camera image with 2D supergaussian fit contours. Figure 42b shows the measured pulse width as a function of grating separation.

3.2.2 The Linear Accelerator

The rf photoinjector used to produce the electron beam for PLEIADES is based on a 1.6-cell standing wave geometry[91], as discussed in Section 3.1.3. A drawing and photograph of the gun is shown in Figure 43. A pulse of S-band (2.8545 GHz) rf input with 7-MW peak power and 3-μs pulse length produces a peak standing wave electric field of up to 100 MV/m that accelerates the electrons to 5 MeV in a distance shorter than 10 cm. Recall that this S-band signal

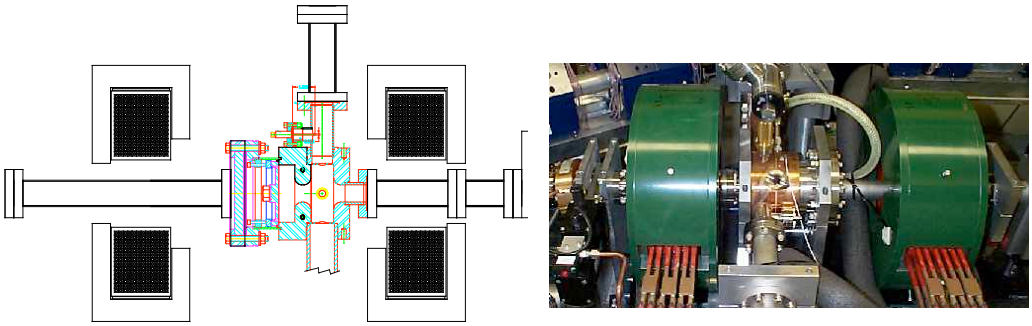

Figure 43 A drawing and photograph of the PLEIADES S-Band rf photoinjector

is generated by frequency upconverting a 81.557 MHz signal drawn from the laser master oscillator pulse train, monitored with a photodiode, and amplifying it to the 7MW level. Focusing solenoids are employed in the photoinjector to preserve the transverse emittance[92] of the electron beam immediately off the cathode and to help match the electron beam into the accelerating sections by compensating for the naturally diverging electron beam typical of photoinjectors[86]. Currently, the gun is being operated with a more conservative accelerating gradient of 80 MV/m to avoid any possible damage due to electrical arcing. This lower gradient also leads to lower quantum efficiency on the photocathode due to the Schottky effect, where the presence of a electric field at the surface of a material lowers the work function of that material.

The electron bunch charge is determined by the pulse parameters of the PLS laser and the quantum efficiency of the photocathode. The 266-nm laser pulse is imaged to a 1-2-mm spot on a copper photocathode near the rf field peak, and electrons are produced (during current operation) with a quantum efficiency of approximately 8×10^{-6} electrons/photon, which yields an electron bunch charge between 250 – 350 pC. Because of the Schottky effect, the quantum efficiency of the cathode is a function of the phase of the accelerating rf field when the uv pulse arrives. The charge coming out of the photoinjector is continuously monitored by an integrating current transformer and that measurement coupled with the continuous uv energy measurement yields a shot-to-shot effective quantum efficiency. This QE is then used as a feedback variable for an rf phase shifter. By shifting the rf phase to keep the QE of the gun constant, long term phase drifts in the rf amplifier chain can be corrected, maintaining optimal electron beam production.

Figure 44 Photograph of the B194 linear accelerator system.

The electron bunch length is a function of the laser pulse duration, bunch charge, and accelerating voltage, and is typically a few picoseconds long. Because the PLS, which is directly responsible for initiating the electron bunch, and FALCON are seeded by the same oscillator, the timing of the electron beam is synchronized to the laser pulse that is to be scattered.

The beam generated by the photoinjector is coupled into the pre-existing 100-MeV linear accelerator, where it is accelerated to energies ranging between 40 and 90 MeV in four of the five truncated SLAC-type traveling wave accelerating sections in the system, each capable of producing up to 30 MV of acceleration. Only four of the five sections are used because of the need to maintain the high-current thermionic beam capability of the linac system. Coupling of the photoinjector to the linac was done by moving the preexisting thermionic injector and one of the linac sections a few meters further upstream, and installing a set of dipole magnets to bend the thermionic beam around the photoinjector, as shown in Figure 45. One accelerator section is needed to get the energy of the beam high enough (make the beam “stiff” enough) that emittance growth isn’t a problem (either from space charge effects or from the dipole magnets)

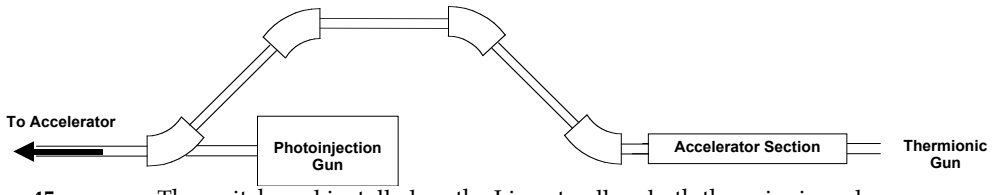

Figure 45 The switchyard installed on the Linac to allow both thermionic and photoinjector guns.

After passing through the interaction area, the electron beam is deflected by a 30°-bend dipole magnet. This dipole serves as a spectrometer, yielding a measurement of the electron energy and energy spread, and also separates the e-beam from the scattered x-rays, which propagate in the same direction as the electrons. Following the dipole, the electron beam is absorbed in a Cu electron dump that is calibrated and provides a measure of the electron bunch charge. The electron dump is housed in a 10-cm-thick lead enclosure to minimize the effect of bremsstrahlung on the diagnostics.

3.3 A Higher-Frequency Gun

In this section, a new higher-frequency gun is tested as a potential replacement for the S-Band gun used on PLEIADES. A detailed theoretical and computational study of the scaling of rf injector beam performance with frequency has been performed[93], with the conclusion that X-band represents an optimum balance between beam quality and accelerated charge and should reach very high brightness. Going to higher frequencies offers some advantages. For example, the emittance of the beam has been shown[93] to scale with the rf wavelength, so higher frequency means lower emittance, and therefore better x-rays. Also, experimental efforts have shown[94] that the accelerating gradient a photoinjector structure can support scales with frequency as

$$E = 220\left[f\left(GHz\right)\right]^{\frac{1}{3}}\ \mathrm{MV/m}$$

meaning more acceleration can be done more quickly, further improving the emittance of the beam.

We have developed an X-band (8.547 GHz) rf gun, based on the 1-1/2 cell, S-band Brookhaven National Laboratory (BNL) design[95]. The details of the design of the gun are discussed elsewhere[96,97]. Basically, the BNL design was scaled down by a factor of three, in

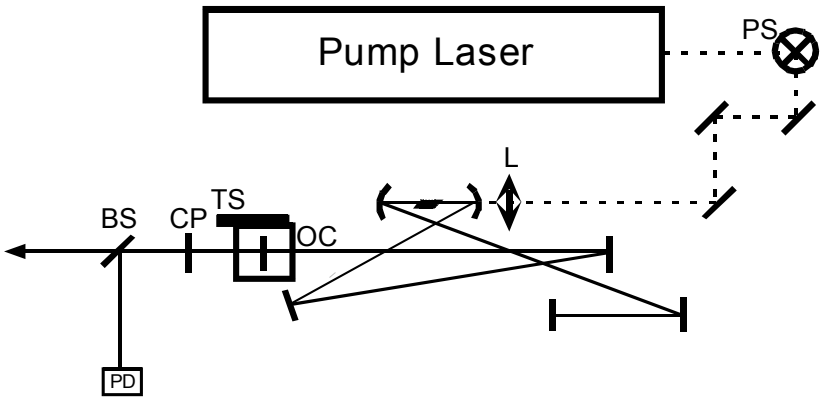

Figure 46 The Ti:Al_2O_3 laser oscillator layout. All components are mirrors unless labeled: PS-periscope, L-focusing lens, OC-output coupler, CP-compensating plate, BS-beam splitter, PD-photodiode, TS-translation stage. The solid line is the 800 nm oscillator beam, the dashed line is the 532 nm pump beam.

proportion to the wavelength of the X-Band klystron that was available. A preliminary version of the gun (Gun 0) was initially tested in 1997 but had several mechanical problems. However, some useful results were obtained which allowed the construction of an improved Gun I. Here, the results of commissioning that gun are presented.

3.3.1 Laser System

The laser system used to illuminate the photocathode is a commercial chirped-pulse amplification (CPA) system, consisting of an oscillator, a grating stretcher, a regenerative amplifier, a grating compressor, and a frequency tripler. The system is based entirely on diode pumped solid-state laser (DPSSL) technology, which provides the stability needed to illuminate the photocathode reliably. The oscillator is a Ti:Sapphire (Ti:Al_2O_3)-based FemtoSource PRO commercial system from Femtolasers Produktions GmbH, capable of producing pulses as short as 10 fs via Kerr-lens mode-locking[98]. These pulses are produced using the technique of mirror-dispersion-control[99], where the dispersion introduced by the thin Ti:Al_2O_3 crystal is compensated for in the dielectric coating on the mirrors. The layout of this system is shown in Figure 46. This oscillator is pumped by a 5W CW, 532 nm beam produced by the intracavity frequency-doubled, diode-pumped, Nd:YVO_4 Millennia V Laser from Spectra-Physics. Since 10 fs pulses are not needed for this application, are difficult to create and maintain, and will be unavoidably lengthened in the amplifier used, the oscillator is operated without the final compensation optics,

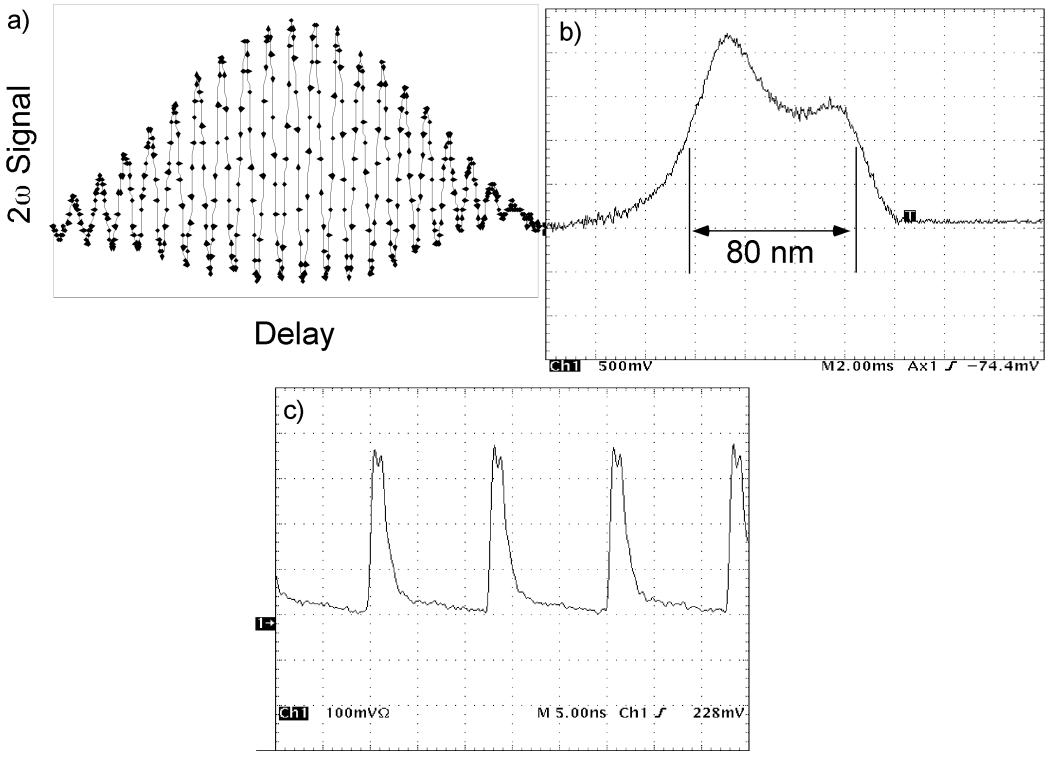

Figure 47 a) autocorrelation trace, b) spectrum, and c) output pulse-train as measured on photodiode of the Ti:Al2O3 oscillator (5 ns/div)

yielding a slightly chirped pulse that is 15 fs in duration. The pulse duration is measured with an interferometric autocorrelator where the pulse is interfered with a time-delayed copy of itself in a nonlinear optical medium. As the time delay is changed, an interference pattern is produced corresponding to the pulses second harmonic autocorrelation (Figure 47a), and the number of fringes in this pattern, coupled with the wavelength of the light, can be used to determine the temporal pulse width. This pulse has a bandwidth of > 70 nm centered around 800 nm (Figure 47b).

The oscillator was assembled with the output coupler mounted on a translation stage; using this set-up, the repetition rate of the oscillator can easily be adjusted between 79.120 MHz and 79.155 MHz without interfering with the Kerr-lens mode-locking process. This system doesn't have the feedback loop described in Section 2.1.1 to keep the frequency locked to a master clock, and so was able to drift over the course of a day. In order to properly synchronize the laser with the rf in the gun, the oscillator cavity length was adjusted to produce a repetition rate of

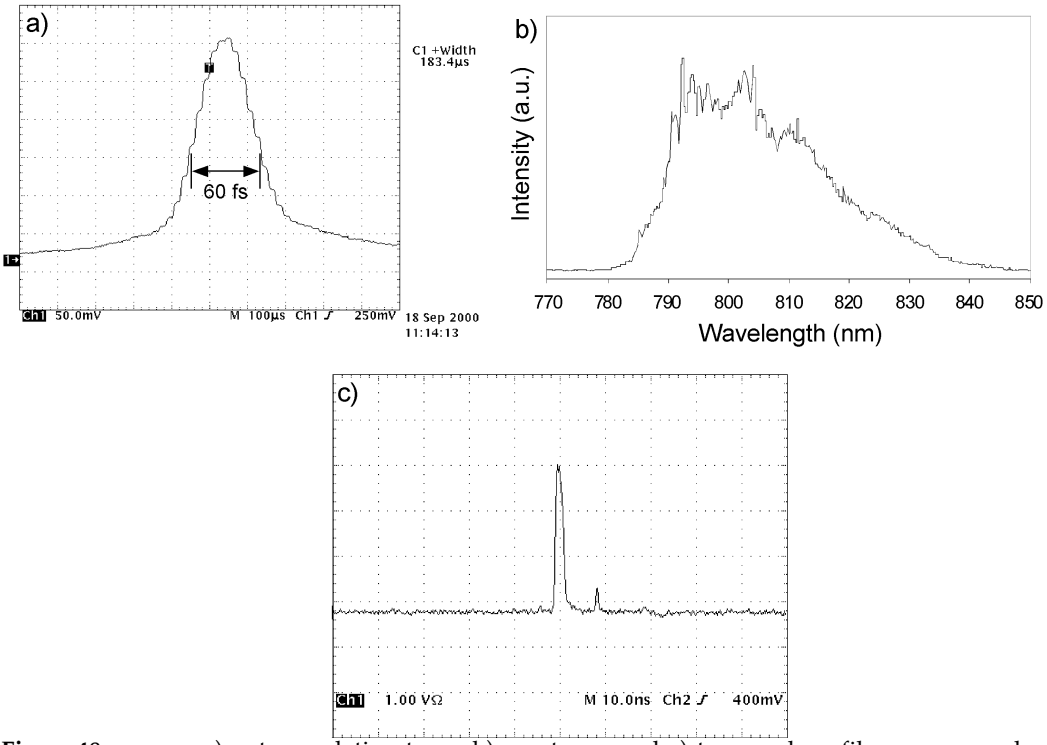

Figure 48 a) autocorrelation trace, b) spectrum, and c) temporal profile as measured on photodiode of one pulse as it exits the regenerative amplifier system (10 ns/div).

79.138 MHz (the 108th subharmonic of the optimal gun operating frequency of 8.457 GHz). The resulting oscillator output pulse train is shown in Figure 47c.

The output of the oscillator is then coupled into a sub-50 fs, 1 kHz Spitfire system from Positive Light, which includes a grating stretcher, a Ti:Al_2O_3 regenerative amplifier, and a grating compressor. The regenerative amplifier crystal is pumped by a 7 W-average power, 1 kHz, Q-switched, diode-pumped Nd:YLF Evolution Laser from Positive Light. This system, as configured, selects a pulse from the 79.138 MHz pulse train and amplifies it to an energy of 0.4 mJ, with a duration of 60 fs and an overall repetition rate of 1 kHz. The output pulse is longer than the input pulse because the spectrally dispersed input beam in the stretcher is wider than the retroreflecting mirror in the system and therefore the bandwidth is clipped down to 25 nm, resulting in a larger minimum pulse length. Figure 48 shows the output spectrum of the Spitfire, the corresponding autocorrelation trace as measured with the single-shot autocorrelator also produced by Positive Light, and the output pulse as measured with a photodiode. The second small pulse corresponds to a portion of the first pulse that was not completely switched out of the

regenerative cavity after amplification and made an extra trip through the cavity; this pulse does not interfere with the operation of the photoinjector, as it is frequency tripled with very low efficiency.

The amplified pulse is directed into a frequency tripler produced by Spectra-Physics. This specific tripler design uses two β-Barium Borate (BBO) crystals for second- and third-harmonic generation. This converts the incoming ir beam to 266 nm, which corresponds to the work function of copper at low fields. To compensate for the walk-off between the ir and the blue in the first crystal, a strongly birefringent crystal is used, which synchronizes the two beams temporally before injection in the tripling crystal. Using this system, uv pulses with 6 μJ of energy are routinely produced. Due to fluctuations in the duration of the output pulse of the Spitfire, the intensity of the uv pulse varied between 5 and 7 μJ on a time scale of a few seconds. These fluctuations seem to be related to instabilities, e.g. from air currents, in the compressor section of the Spitfire.

The uv beam is then injected onto the photocathode at 3 degrees from normal incidence using a custom-made high-vacuum "Y" piece attached to the output face of the gun (see Figure 53). The straight arm of the "Y" is the photoelectron beamline The 3-degree arm is sealed with a Suprasil window, which has good transmission at 266 nm. In order to align the laser down the beam pipe properly, a lamp was placed against the beamline to illuminate the copper photocathode, which diffusely reflected some of the light down the "Y". Two apertures were then placed such that the cathode could clearly be seen through both of them, and the laser was subsequently passed through the apertures.

3.3.2 RF System and e^- beamline

The master source of the rf signal for the X-Band photoinjector is, as was true for the S-Band photoinjector, the pulse train from the uv drive laser; the jitter performance of this scheme is discussed in Sections 3.3.3 and 3.3.4.6. A photodiode monitoring the 79.138 MHz oscillator pulse train sends this signal, after moderate filtering to make the signal more sinusoidal than shown in Figure 47c, to a phase-locked dielectric resonant oscillator (PDRO), which scale the frequency up by a factor of 108, producing a 8.547 GHz signal. The PDRO has an input frequency

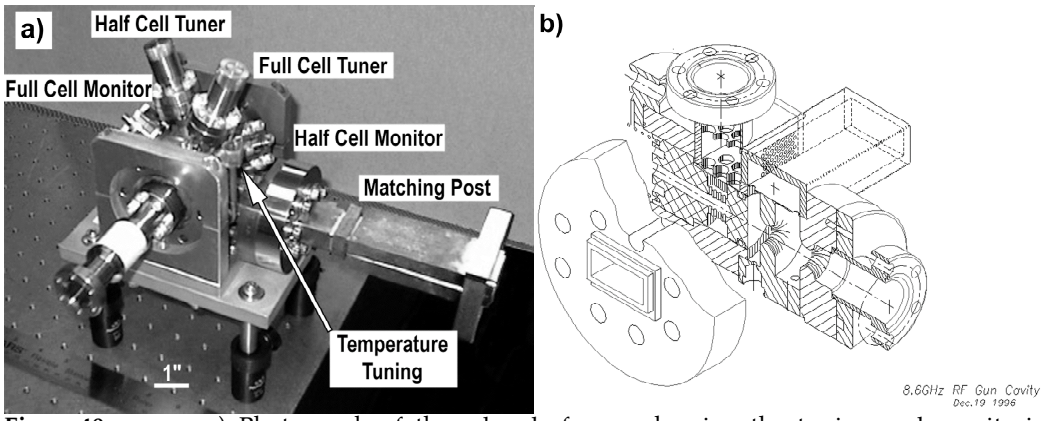

Figure 49 a) Photograph of the x-band rf gun, showing the tuning and monitoring features, b) CAD model of the gun

range of ±50 MHz, yielding the frequency tuning required for proper conditioning of the high-power rf gun. This 8.5 GHz signal is then sent to a 1 kW traveling wave tube amplifier (TWTA), followed by a Stanford Linear Accelerator Center (SLAC) SL-3 Klystron[100] capable of producing up to 19 MW of rf power in 1-2 μs square pulses, at up to a 50 Hz repetition rate. The power is measured by using a precision thermistor head for the average power, and a fast (< 600 ps rise-time) rf diode for determination of the pulse duration. For the present experiments, the klystron runs at 20 Hz with a 250 ns rf pulse, to allow for higher gradients in the gun without rf breakdown problems.

The heart of the rf system is a high-Q (4,274 measured) X-Band rf gun, shown in Figure 49. The 1-1/2 cell design yields good rf and electron beam characteristics, as summarized in Table IV; however, the π-mode magnetic coupling scheme employed in this design is quite sensitive to mechanical tolerances. In particular, achieving critical coupling in the structure requires a very

Table IV — 1.5 cell theoretical beam parameters

Beam Energy	5.7 MeV
Coupled RF Power	16 MW
Bunch Charge	0.1 nC
Normalized Emittance	0.7 π-mm mrad
Energy Spread	0.25%
Bunch Duration	0.9 ps FWHM Gaussian
Laser Spot Size	0.67 mm FWHM Gaussian
Optimal Injection Phase	65°

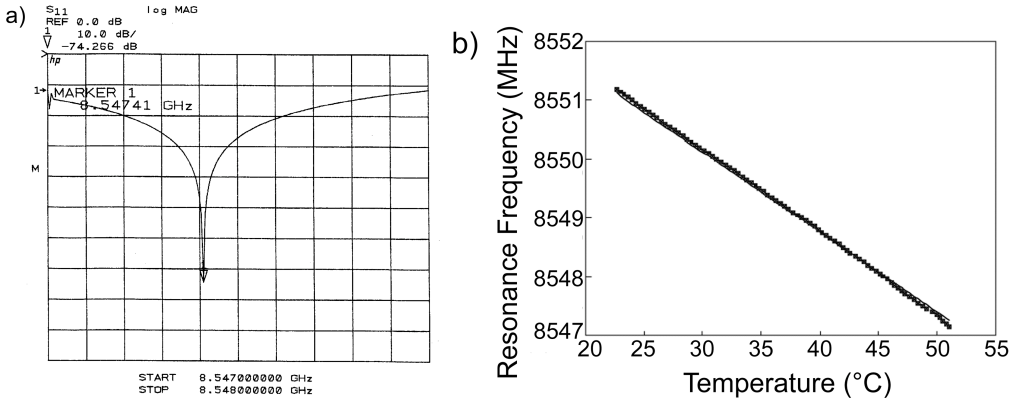

Figure 50 a) Gun power reflection as a function of frequency. The horizontal axis runs from 8.547 GHz to 8.548 GHz with each division being 100 kHz, and the vertical axis runs from 0 to -100 dB with each division being 10 dB. b) Gun resonance frequency as a function of temperature. The line is the theoretical prediction (Eq. 41) and the points are measured values.

high degree of precision in the design and fabrication of the coupling holes between the WR-90 waveguide, which carries the rf power to the gun, and the half and full cells; in practice, the small mechanical shifts induced by the brazing process require a post-brazing tuning mechanism to compensate for these effects. In the present case, a custom tuning post piece was fabricated by SLAC to ensure that the peak of the gun resonance is properly correlated with the maximum of the SL-3 rf power tuning curve. This tuning of the rf gun coupling is supplemented by two independent tuners for the half and full cells, and the overall resonant frequency of the system can be temperature-tuned once balanced, π-mode critical coupling is achieved.

The main steps of the gun tuning procedure are as follows: first, using a network analyzer, the full cell is tuned slightly above the desired operation frequency; second, we merge the half-cell resonance for balanced π-mode operation; finally, the operation frequency is reached by heating the structure. The reflection from the X-band gun, after the tuning procedure described above, is shown in Figure 50a. In this case, the resonant frequency is f = 8.547 GHz, the reflected wave is -74.266 dB below the input signal, and the -3 dB bandwidth of the resonance is 4 MHz, which corresponds to a Q-value of 4,274. The gun temperature-tuning curve is shown in Figure 50b, and is found to be in agreement with the theoretical prediction based on a cylindrical pillbox model of the gun[101]. The TM_{010} resonant frequency is given by $f_{010} = \frac{c}{2\pi}\frac{\pi'_{01}}{a}$ where a is the cavity radius and π'_{01} is the first root of the zeroth-order Bessel function; using the linear

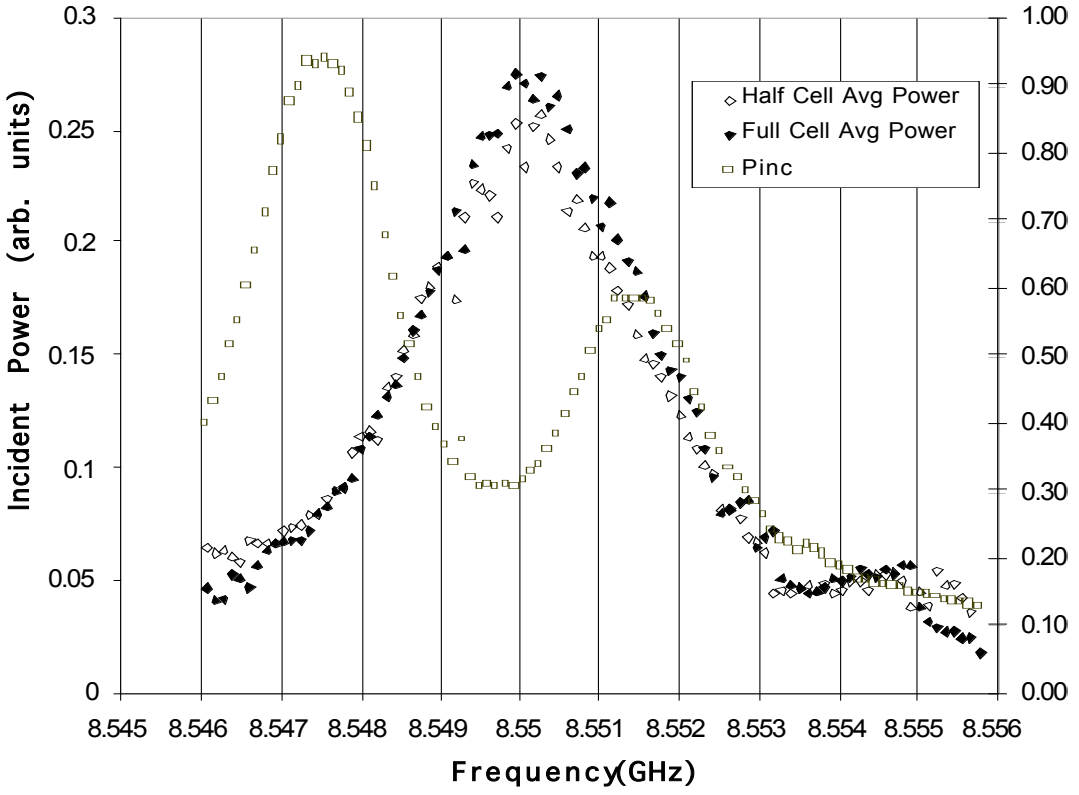

Figure 51 Power incident upon the gun (P_{inc}), and the power in the half and full cells of the gun as measured by the monitor probes and normalized to the incident power.

coefficient of thermal expansion for Copper, α=1.6 x 10^{-6} °C^{-1}, the slope of the frequency shift can be calculated to be -136 kHz/°C as follows:

$$\Delta f = \frac{df}{da}\frac{da}{dT}\Delta T = -\alpha f_{010}\Delta T. \qquad (41)$$

The corresponding linear shift is also shown in Figure 50b.

The next experimental step involves repeating these measurements *in situ*, with the full rf signal. Magnetic pickup loops are located within the half and full cells and are designed with very low coupling parameters in order to avoid perturbing the rf fields in the accelerating structure and causing rf breakdown. Their calibration procedure is straightforward: the gun is tuned to obtain a hard resonance in either the half or the full cell and the power coupled into the structure is obtained by measuring both the incident and reflected power. The crystal detectors are calibrated at the same frequency with a CW rf source, a frequency counter, and a power meter using a precision thermistor head. The half-cell monitor coupling parameter is thus found

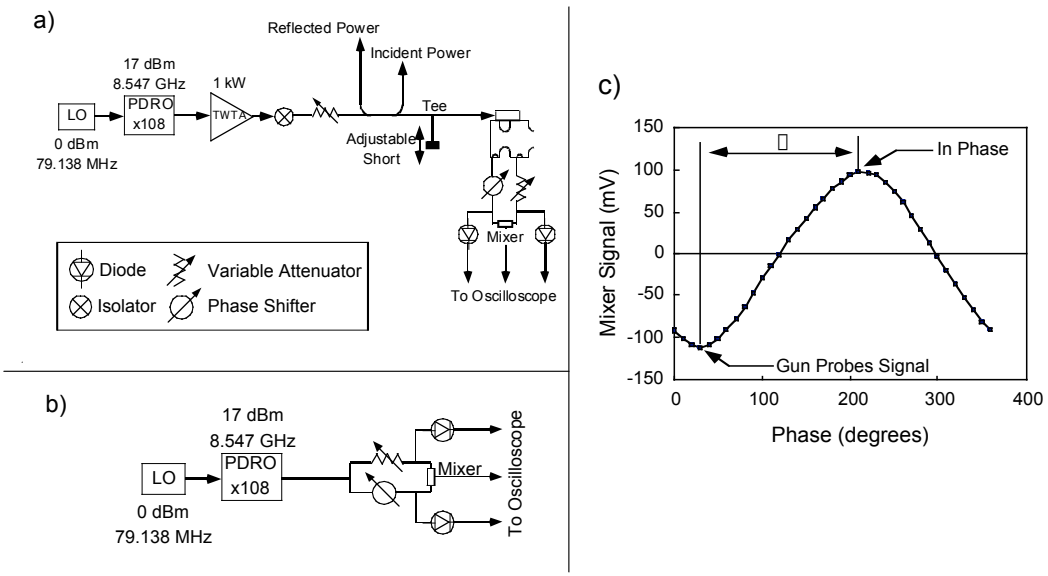

Figure 52 Schematic of a) the interferometer set-up used to check the relative phases of the half and full cells of the gun, and b) the set-up used to calibrate the interferometer. c)The calibration curve of the interferometer, showing the mixer signal as a function of phase shifter phase setting. Setting the phase shifter to give a maximal result during calibration yields a minimal result when measuring the gun, indicating a π phase shift between the two cells.

to be -57.4 dB, while the full cell monitor couples -46.9 dB of the incident power. The power coupled in the half and full cell are shown in Figure 51 as functions of the frequency and normalized to the input power. The difference in power between the half and full cell corresponds to a 3% variation in terms of the rf fields, and shows balanced excitation of the gun.

At this point, the most critical remaining step is to verify that the mode excited in the gun is the proper accelerating π-mode. The experimental set-up is shown in Figure 52a. First, an absolute calibration of the X-band interferometer is performed by splitting the incident power from the PDRO with a tee (Figure 52b): the power on each arm is first balanced with a precision attenuator, and the mixer response is measured as a function of the phase shifter settings, as shown in Figure 52c. The frequency chosen for the calibration corresponds to the frequency at which critical coupling is achieved. We then set the interferometer at the phase giving the maximum positive output signal (210°, in this case), and replace the tee with the gun probe outputs. Note that the orientation of the loops is carefully controlled for these phase measurements; in addition, both probes have exactly the same microwave path length. Again, the interferometer power is balanced, and we observe a mixer output signal with maximum

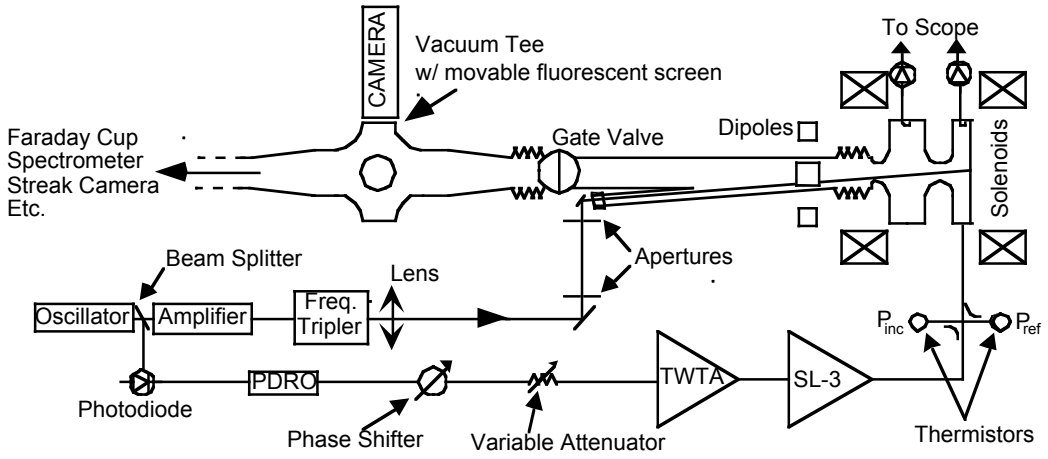

Figure 53 A schematic of the overall experimental setup, showing the rf system and the electron beamline.

amplitude and negative polarity; this shows that the relative phase of the gun field monitors is shifted by 180°, as compared to the reference signals provided by the tee in the calibration described above. Thus, balanced π-mode excitation has been demonstrated; in addition, we have varied the tuning of the half and full cells and the operation frequency around these parameters and found that we could not excite the 0-mode, which indicates that π-mode coupling conditions are quite robust, as designed. Two solenoids, aligned to yield antiparallel magnetic fields and a null on the photocathode, are used to extract the beam from the gun, as was done with the S-band gun in section 3.2.2.

The beamline used for the experiment is shown in Figure 53. Following the extraction solenoids mentioned above is a pair of orthogonal dipole magnets that are used to steer the beam and center it on the detectors. The beam passes through a gate valve which can be closed to allow easy changes to the beamline to accommodate different measurements. For most of the measurements, the gate valve was followed by a vacuum tee with a fluorescent screen which could be moved in and out of the beam. Off to one side was a video camera to capture the fluorescence from the screen. Different experimental setups were deployed following the tee: to measure quantum efficiency, a 50 Ω-matched Faraday cup is used; for the beam energy and energy spread measurements, a magnetic spectrometer is attached. A quartz window placed at the end of the beamline allows the use of either a streak camera for beam duration and timing jitter measurements or an rf detector system (as discussed in section 3.3.4.7) to study coherent

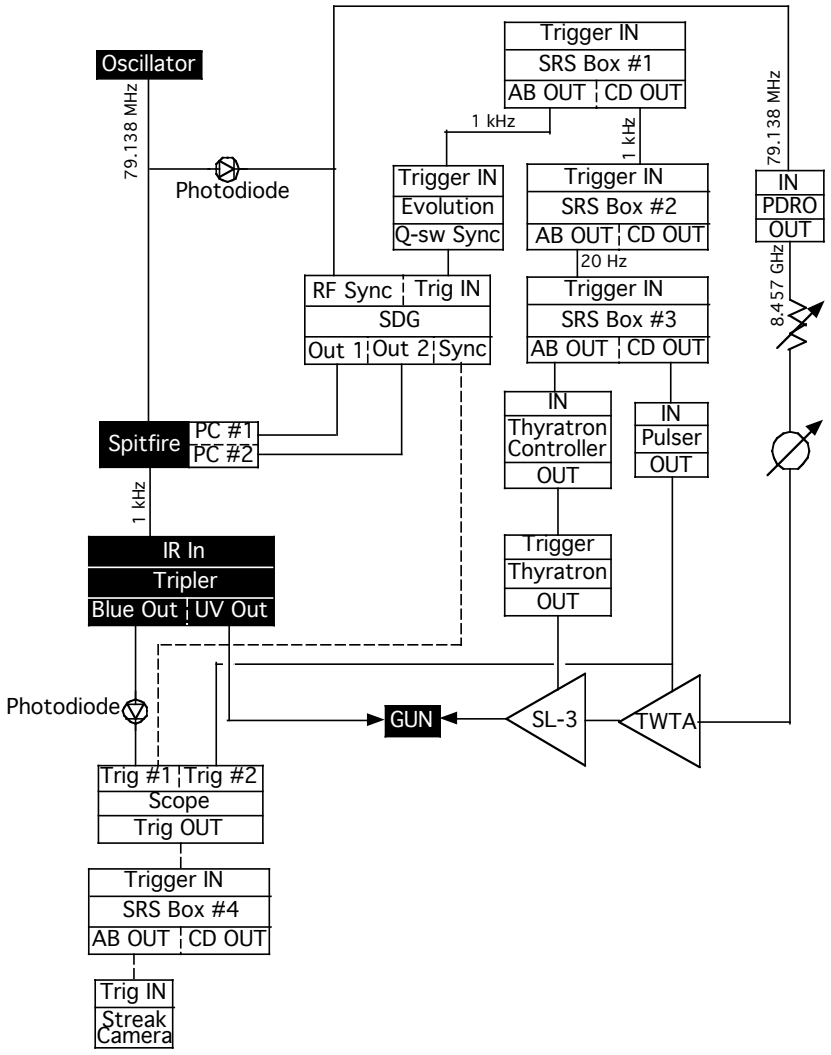

Figure 54 Diagram of trigger, laser, and rf signals in the entire experimental set-up. Black boxes are laser elements, white boxes are electronic elements. SRS Boxes are Stanford Research Systems DG535 Delay Generators, SDG is the Positive Light Synchronization and Delay Generator, PC is Pockels Cell. See text for full description.

synchrotron radiation. For the emittance measurement, another vacuum tee with a tantalum plate with various sized holes and a 1 m beam pipe was placed between the gate valve and the fluorescent screen, as discussed in section 3.3.4.4.

3.3.3 Timing

In order to produce a photoelectron beam reliably, it is essential to illuminate the photocathode within a very narrow temporal window, extending about one degree off the optimal rf phase. At the operating frequency of 8.547 GHz, this requirement translates to a timing

accuracy of approximately 3 ps. The overall timing system used is shown in Figure 54. The gray boxes represent laser components and the white boxes represent electrical components. This system solves the three main problems of timing: 1) producing the photoelectrons at the proper rf phases, 2) properly timing the laser and rf fields in the gun, and 3) measuring quantities associated with a 20 Hz system that are synchronized to a 1 kHz event.

The 79.138 MHz pulse-train from the oscillator is sampled with a photodiode; this signal is then fed into the PDRO, which raises the frequency by a factor of 108 yielding a 8.547 GHz signal that is precisely locked in phase with the laser pulses. This signal then goes through a variable attenuator to control the power in the gun, and a phase-shifter to adjust and optimize the timing of the laser pulse and the rf phase. This signal is subsequently gated and amplified by both the TWTA and the klystron before injection into the gun.

In order to ensure that the uv laser pulse arrives in the gun while the TWTA and klystron are energized, a master clock is used. The 1 kHz timing signal originates from a Stanford Research Systems Pulse and Delay Generator DG535 (an "SRS Box") which is capable of outputting two different, arbitrary pulses with a specified precision of 5 ps. The SRS Box (hereafter referred to as SRS Box #1) is free-running at 1 kHz. One of the two output pulses is used to trigger the Q-switching of the regenerative amplifier pump laser. When Q-switching occurs, a pulse is sent to a synchronization and delay generator (SDG). The SDG compares the 1 kHz Q-switch signal to the 79.138 MHz photodiode signal mentioned above. When the pump laser fires, the next pulse from the photodiode triggers three output signals with user-defined delays. Two of these signals are used to control the two Pockels cells in the regenerative amplifier, and the third can be used to trigger an oscilloscope.

The second output pulse from SRS Box #1 is sent to SRS Box #2, which divides the 1 kHz signal down to 20 Hz; the 20 Hz signal then controls SRS Box #3. The first pulse from the third box triggers the thyratron controller, which fires the thyratron and thereby determines when the klystron electron beam is on. The second pulse from SRS Box #3 triggers a pulse generator, which is used to create the pulse that gates the TWTA and determines the timing and duration of the rf signal in the klystron and rf gun. Therefore, by adjusting SRS Box #3, the rf signal can be

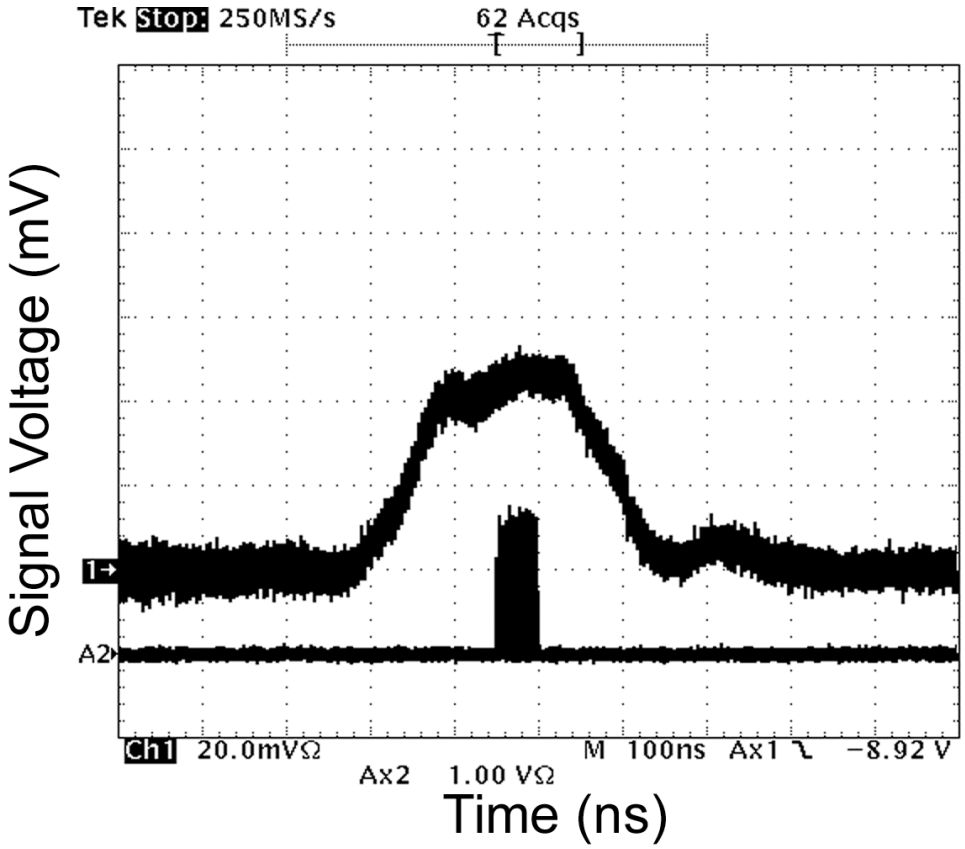

Figure 55 Several overlain traces demonstrating the size of shot to shot laser arrival time jitter. The upper trace is the full cell power measured by the monitoring probe, and the lower trace is the signal from a photodiode measuring the laser. The horizontal scale is 100 ns/div, and the vertical scale is in arbitrary units.

optimally synchronized relative to the klystron electron beam, and by adjusting SRS Box #1 the laser can be properly timed relative to the rf in the gun.

In order to take measurements of the photoelectron beam, a trigger for the oscilloscope that is synchronized to the laser is required; however, not all of the uv laser pulses (at 1 kHz) will occur concurrently with accelerating fields in the gun (at 20 Hz). Therefore, a logic gate is used on the oscilloscope to trigger only when there is both a laser pulse and a gate pulse to the TWTA. This trigger signal is also output from the scope and used to fire the streak camera for measurements. An additional SRS Box allows fine tuning of the timing of the streak image.

Once the timing of the system is properly set, the shot-to-shot timing jitter needs to be studied. This involves both a measure of the jitter between events and the master clock, and the relative jitter between two events that require simultaneity. There are two pairs of events for which the amount of jitter is crucial: the arrival of the uv laser pulse and the timing of the rf pulse

in the gun, and the arrival of the uv laser pulse and the phase of the rf in the gun. The former is easily studied by comparing the signals on an oscilloscope (see Figure 55). There is about 50 ns of jitter in the arrival of the laser relative to the rf pulse. This is most likely a result of the random selection of one of 4 pulses (spaced 12 ns apart) by the SDG in starting the timing cycle of the regenerative amplifier. However, since the gun is filled with a fairly uniform rf power for approximately 150 ns, that jitter is not very significant. The latter form of jitter (laser timing versus rf phase), is more difficult to measure, and is discussed in Section 3.3.4.6.

3.3.4 Measured Properties

The photoelectron beam is optimized by examining Faraday cup measurements and the image of the beam on a phosphor screen; adjustments can be performed by varying the laser injection phase, the rf power energizing the gun, or the magnet focusing strength. A current of 25-50 A is used in the extraction solenoids mentioned above, which corresponds to a magnetic field strength in the 1-2 kG range. Additionally, the amount of power in the gun chosen for measurements is 1-2 MW, which was selected because, at this level, a high-quality electron beam is produced, and dark current is minimal.

In measuring the various relevant quantities of the electron beam, a fairly large amount of random fluctuation was noticed. It is believed that most of this was due to instabilities in the intensity and pointing of the laser system. Additionally, the timing jitter between the rf phase and laser injection was larger than the optimal 0.3 ps threshold, which also degraded the shot-to-shot beam quality significantly. In gathering these data, with the exception of the charge and Schottky values, single-shot measurements were performed to capture some of the cleaner events; therefore these numbers represent an optimal beam which was not continuously generated.

3.3.4.1 Dark Current

Before discussing the photoelectron beam characteristics in detail, a few words concerning dark current are in order. At power levels in excess of 100 kW, dark current was detected with the Faraday cup. The dark current is a strong function of the electric field at the photo-cathode surface, and (from the Fowler-Nordheim equation[102]) varies exponentially with

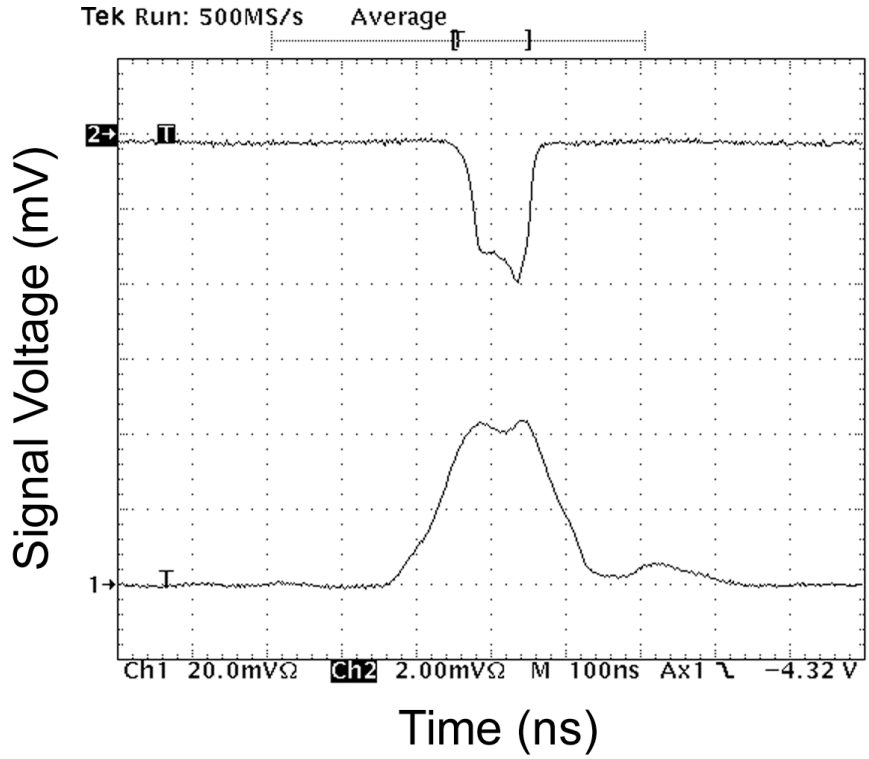

Figure 56 Faraday cup measurements of dark current. The upper trace is the dark current signal with a cathode gradient of 125 MeV/m, showing a current of ~70 μA, and the lower trace is the power in the full cell of the gun. The horizontal scale is 100 ns/div and the vertical scale is 2 mV/div for the upper trace and 20 mV/div for the lower.

the electric field at the photocathode. The dependence of the field-emission current with the applied field at the cathode appears very clearly in Figure 56: during the ramp-up of the rf power in the gun, the exponentiation of dark current is evident; furthermore, the small rf power fluctuations observed in the gun are translated into comparatively larger variations in the dark current.

In practice, one must carefully rf- and vacuum-condition the photoinjector to help minimize field emission, which produces a weak beam that can generates background x-rays via Bremsstrahlung and erode various surfaces in the rf structure through direct electron bombardment, as well as secondary electron emission and potential avalanche breakdown initiated by the dark current. Furthermore, in more complex structures, the large number of emitting surfaces subjected to high rf fields can result in the emission of different dark current beams, which can severely limit the operation of the device and the detection and characterization of the photoelectron beam. For the experiments described here, however, dark

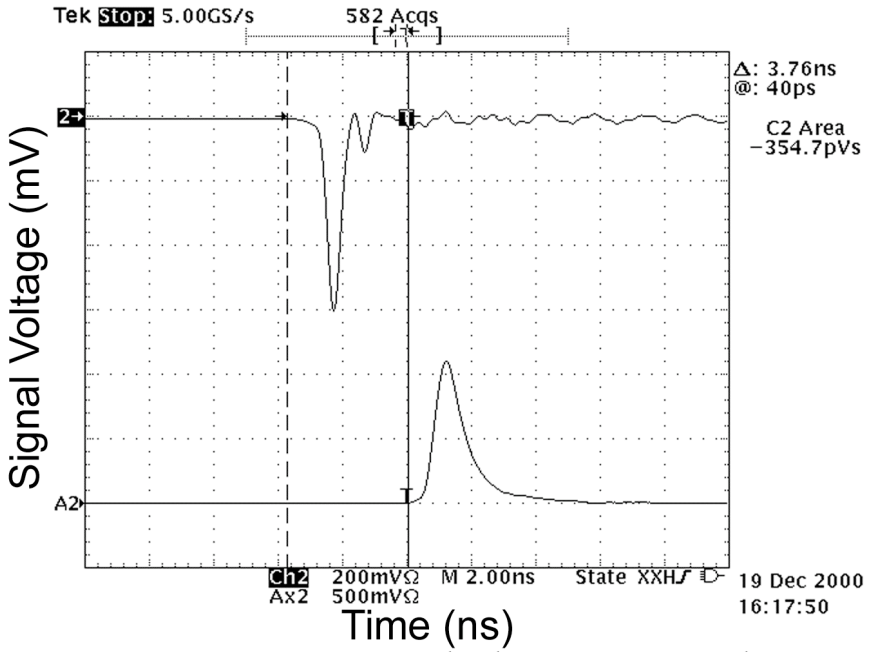

Figure 57 Faraday cup measurement of the photoelectron current. The upper trace is the photoelectron signal from the faraday cup, and the lower trace is the laser signal from a photodiode. The horizontal scale is 2 ns/div, and the vertical scale is 200 mV/div for the upper trace and the 500 mV/div for the lower.

current proves to be a minimal problem when compared with breakdown at the aforementioned matching post required to achieve critical coupling, which limited the power coupled into the gun to approximately 3 MW with a 150 ns flat-top rf pulse; this corresponds to an average accelerating gradient of 80 MeV/m, and a peak rf field at the cathode surface, E_0 = 183 MV/m Typical operation was achieved in the 1-2 MW range, corresponding to cathode fields of 106 to 150 MV/m, with output beam energies varying between 1.425 MeV and 2 MeV.

3.3.4.2 Quantum efficiency

The first measurements of the photoelectron beam were made using a Faraday cup matched into 50 ohms. Taking the signal from the Faraday cup, the area under the signal voltage curve and Ohm's law can be used to determine the total charge in the beam. Figure 57 shows both the uv laser pulse that creates the electron bunch and the Faraday cup signal used to determine the charge. The fact that the laser appears to arrive after the electron beam is merely a result of different signal cable lengths; in addition, it is noted that the photodiode signal does not reflect the actual laser uv pulse duration, the diode response time is too slow. This particular

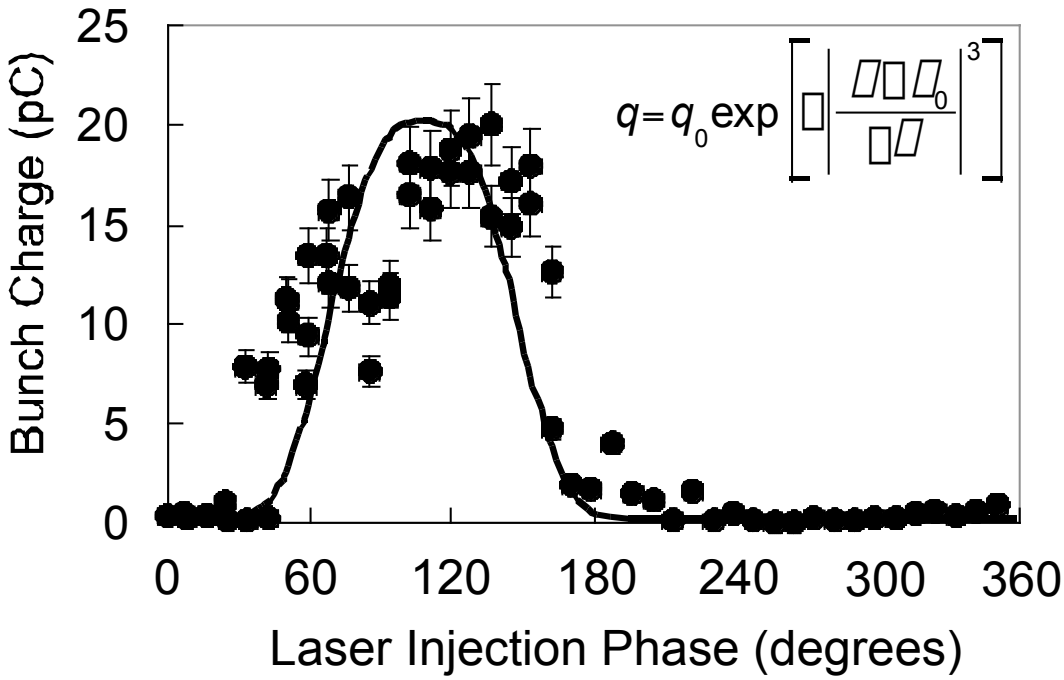

Figure 58 Measured bunch charge versus rf phase when the laser is injected, showing the Schottky effect. The dots are the actual data, and the line is the fit to the supergaussian with equation shown. [This fit merely matches the shape of the data, compare with Figure 62]

measurement yields a total charge of 25 pC. Given the input energy of the uv laser as 6 μJ, this yields a quantum efficiency for copper of 2×10^{-5}. The linearity of the bunch charge with the laser energy was verified experimentally between 0 and 25 pC. The aforementioned shot-to-shot variations occurring at 20 Hz can be partially eliminated by averaging over several shots; good results were obtained by averaging for 5 s over 100 shots. Furthermore, given the high rf field at the cathode and low laser energy used in the measurement, the beam current is not limited by space charge.

The second measurement performed with the Faraday cup was a study of the phase dependence of the charge. The rf phase relative to the laser was varied over 360 degrees, which has two consequences; first, it affects the energy of the beam because it influences the timing of the acceleration of the charge; this means that, for most injection phases, there will be no beam because either the fields do not accelerate the electron bunch, or accelerate it back into the photocathode. This effect alone results in the form of the data presented in Figure 58. The supergaussian fit to the data is not chosen to calculate any beam parameters, and instead merely

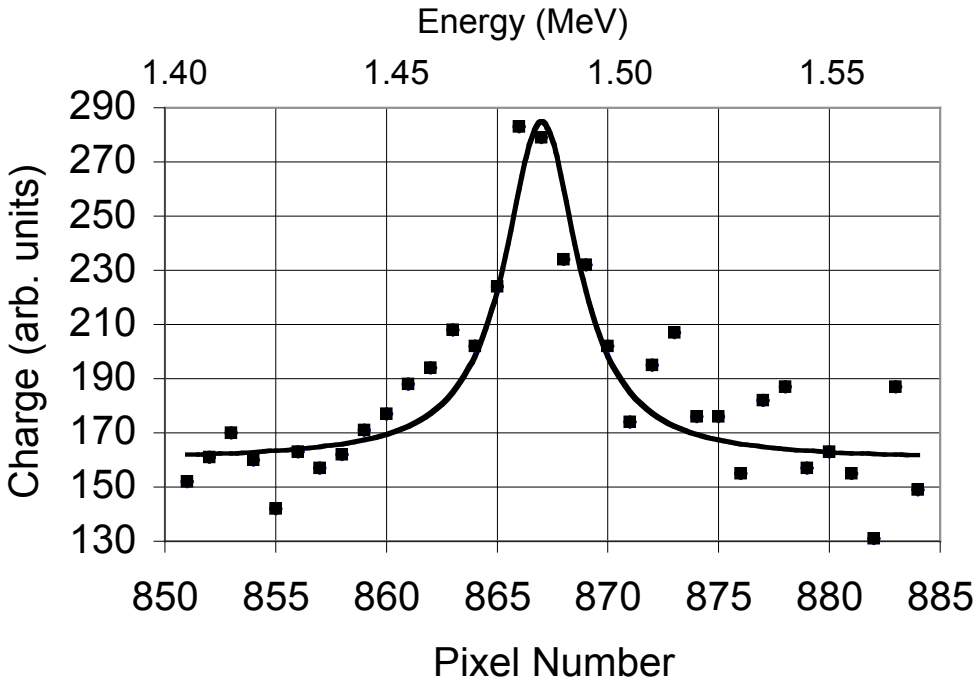

Figure59 Energy spread of the photoelectron beam as measured by the electron spectrometer. The energy spread is about 1.8%

represents the general shape of the data, which is used to compare to the shape of the coherent synchrotron data in Section 3.3.4.7. There is no physical motivation for the equation used. The second effect is that by varying the phase, the electric field strength at the photocathode when the uv laser pulse arrives changes. A higher field results in an enhancement of the quantum efficiency (the Schottky effect). When the laser is synchronized with the peak of the rf cycle, more photoelectrons are produced and the final beam charge is higher. Although variation of the effective quantum efficiency with the rf phase is illustrated in Figure 58, and the expected slope on the top of the curve is hinted at, the large fluctuation in the data from the aforementioned instabilities prevents conclusive observation of the Schottky effect.

3.3.4.3 Beam energy and energy spread

To measure the energy and energy spread of the electron beam, an electron spectrometer[103] is used. The instability of the beam and the small (1 mm diameter) entry aperture on the spectrometer made coupling electrons into the device a challenging task. As a quick

solution, a 2 Hz triangular wave was applied to one of the steering dipoles, creating a horizontal scan of the beam across the spectrometer aperture and ensuring that, on at least some shots, clean energy measurements could be recorded. A field of 0.73 kG (3 A current) was used and the image produced by the deflected electrons on the phosphor screen was recorded on Polaroid film. These images were optically scanned at 600 dots per inch (dpi) resolution into a computer and saved as eight-bit grayscale TIFF (Tagged Image File Format) files. The distances between reference points on the image, which correspond to small lights in the spectrometer phosphor, is known. Hence, one can obtain a spatial scaling factor by directly measuring the distance between the reference points on the photographs, and their equivalent dimensions in the experiment.

Using the magnetic field strength and the parameters given in [103], the energy of the beam was determined from the location of the image of the entrance slit to be 1.47 MeV, and the width of a spot gave a relative energy spread of $\Delta\gamma/\gamma_0$ = 1.8±0.2% FWHM (see Figure 59). The dispersion in the magnetic energy spectrometer can be evaluated as follows: the transverse velocity of the electrons is given by

$$v_\perp = c\beta_\perp = \omega_c r = \frac{eB_\perp}{\gamma m_0} r \tag{42}$$

where $B_\perp$ is the applied magnetic field and r is the radius of the electron trajectory in the dipole magnet. Differentiating (42), and using the normalized momentum, we have

$$\Delta u = \frac{\Delta p}{m_0 c^2} = \frac{eB_\perp}{m_0 c^2} \Delta r \tag{43}$$

for a field of 0.73 kG, the dispersion is 42.7 m^{-1}. As the beam energy is measured at 1.47 MeV, and a pixel on the recorded energy spectrum corresponds to 0.4 mm, we find that the 4-pixel FWHM spectrum has a momentum spread Δu = 0.068 which corresponds to a relative energy spread $\Delta\gamma/\gamma$ = 1.8%, since $\gamma^2 = 1 + u^2$.

3.3.4.4 Beam emittance

To measure the beam emittance, direct examination of the beam divergence is made. First, a phosphor screen was used to determine the size of the electron beam (Figure 60a), which

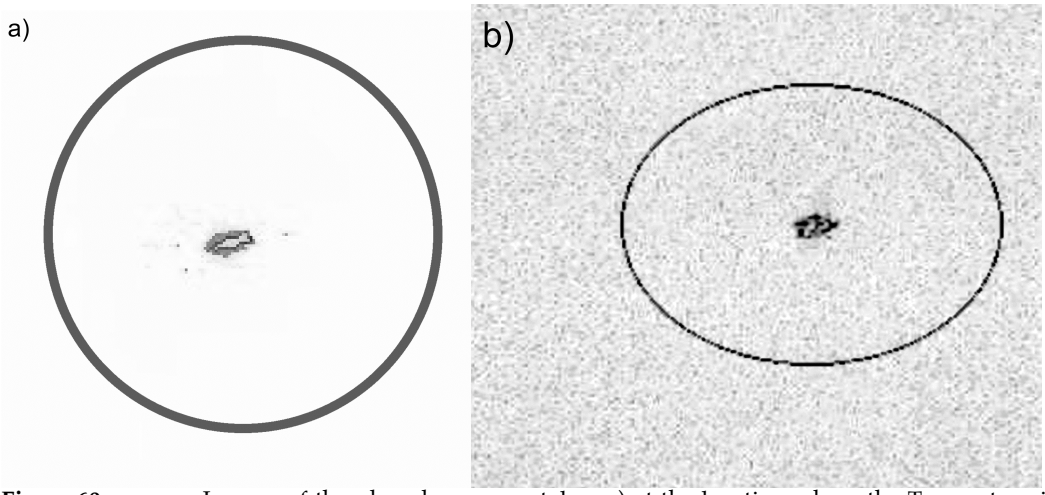

Figure 60 Images of the phosphor screen taken a) at the location where the Ta aperture is placed, and b) a meter downstream from the Ta aperture. The circles represent the edge of the phosphor screen which is 19 mm in diameter. The oblong shape of b) results from looking at the screen at a 45∞ angle of incidence.

was found to be 1.68 mm in diameter. This screen is then replaced by a thin tantalum (Ta) plate, with three holes of diameter 0.25, 0.5, and 1 mm. Placing this plate in the beam path will completely stop the beam. The 1 mm-hole is centered on the beam to allow a small sample of the electron beam, with known diameter, to pass. The phosphor screen is placed 0.997 meter away from the Ta plate. The size of the electron beam at the phosphor is measured to be 1.84 mm, as shown in Figure 60b.

Because the spot started with a diameter of 1 mm from the hole in the Ta, this means the edge divergence of the beam is 0.84 mrad, while the maximum core divergence, for on-axis electrons, is 1.84 mrad. Since the charge of this bunch is sufficiently small, space-charge effects on the emittance are negligible, and this divergence is a direct reflection of the transverse momentum spread of the beam. The transverse phase space of the beam can then be mapped by moving the Ta aperture and measuring the corresponding divergence angles. Using this technique, and limiting the count to 90% of the bunch charge, the normalized emittance of the beam is found to be $\varepsilon_n \approx 1.65$ mm mrad at 25 pC of charge. This is an excellent number, especially in view of the relatively low beam energy and absence of emittance compensation; furthermore, it is in good agreement with PARMELA simulations as presented in Table IV.

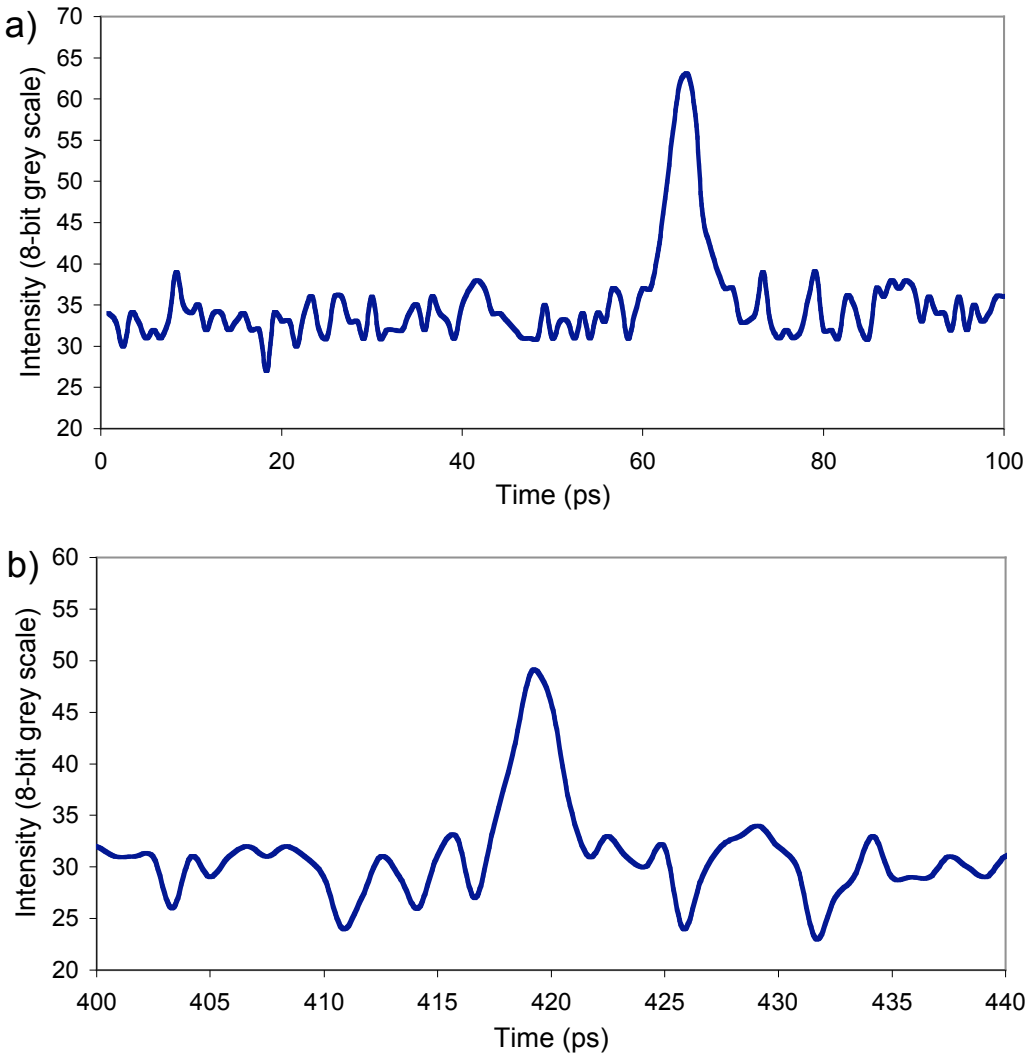

Figure 61 Streak camera image line-outs. a) The reflection of the laser beam off the photocathode with no rf in the gun (and therefore no photoelectron beam and emission produced). The 2 ps length demonstrates the camera resolution. b) Emission from the photoelectron beam with the laser blocked by a filter, showing the duration to be at or below the camera resolution (2 ps).

3.3.4.5 Bunch duration measurements

To get an estimate of the bunch length, a streak camera operating at its maximum streak speed of 20 ps/mm is used to image the phosphor screen. The streak image is captured on Polaroid film, which is then scanned into a computer, as discussed in Section 3.3.4.3. To determine the resolution of the camera, a measurement of incident uv laser pulses was first made (Figure 61a). The streak image was measured to be 2 ps long FWHM, which matches the nominal

resolution of the camera, as the actual duration of the uv laser pulse is well under 100 fs. When the electron beam is present, a prompt emission is observed on the streak image, followed by an image of the slow fluorescence of the phosphor. To distinguish between the light emitted by the electrons, and that corresponding to the diffused light from a uv laser pulse striking the photocathode, a Plexiglas filter is used to cover half of the entrance slit: only the visible optical radiation produced by the electrons propagates through the filter, while the laser light is strongly attenuated; in addition, the delay induced by the refractive index of the Plexiglas can be used to further calibrate the streak camera. It is unclear if the observed line is purely Cerenkov radiation, or also produced by fast x-rays interacting with the phosphor screen, but the duration of the light pulse in either case is directly correlated to the duration of the electron bunch, as shown in Figure 61b, where we find it to be equal to the 2 ps resolution of the camera itself, as determined by the technique described above; this indicates that the duration of the electron bunch is less than 2 ps. Further evidence of the extremely short electron bunch duration is obtained by considering the coherent synchrotron radiation emitted by the electrons when propagating in a short, slow-wave structure; this is studied in greater detail in Section 3.3.4.7.

3.3.4.6 Timing Jitter

Next, we have studied the timing jitter between the rf fields in the photoinjector, the uv laser pulses, and the photoelectrons. The measurement of the charge produced as a function of the laser injection phase provides an indirect estimate of the timing jitter between the uv laser pulses on the photocathode and the rf fields exciting the accelerator structure: if the jitter is larger than approximately 10 degrees of rf phase, such a measurement could not be performed; in fact, the good contrast on the coherent synchrotron radiation curves (Figure 62b) shows that the transition from photoemission to dark current can only be pinpointed to within 10 degrees.

To obtain a better estimate, we have systematically measured the timing between uv laser pulses and the visible radiation flashes produced by the photoelectrons on the screen used in Section 3.3.4.4; this is achieved by acquiring a large number of shots, and using statistical tools to analyze the experimental results. The first calibration is obtained by carefully measuring the timing jitter between the streak camera and the incident uv laser pulses; unfortunately, that

number is found to be high, of the order of 60 ps. This large number is due to jitter in the oscilloscope, the SRS box, and mostly jitter inherent in the streak camera. The reason for requiring a low base number is that, for uncorrelated sources of timing jitter, the statistical width of the measured distribution scales as

$$\Delta t = \sqrt{\Delta t_1^2 + \Delta t_1^2 + \cdots \Delta t_n^2}\,, \tag{44}$$

where the Δt_i correspond to different mechanisms producing timing jitter in the system. For our experiments, the main known and measured values are: Δt_l < 2 ps for the measured laser pulse duration, as streaked by the camera; Δt_e < 2 ps for the optical light flashes produced by the photoelectron beam; finally, Δt_{ls} = 60 ps is the timing jitter measured between the streak camera and the uv laser pulses. Clearly, this last contribution dominates in (44), and limits the accuracy of our measurement of the timing jitter between the photoelectrons and the incident uv laser pulses: if the width of the Gaussian statistical distribution can be estimated to within a relative accuracy, ε, it is easily seen that the corresponding precision on the timing jitter will be of the order of $\sqrt{2\varepsilon}$. In our case, $\varepsilon \approx 5\%$ and the minimum value of Δt_{le} that can be measured reliably is approximately equal to $\sqrt{2\varepsilon}\,\Delta t_{le}$ = 19 ps. Our analysis shows that the width of both distributions, the uv laser pulses on the one hand, and the Cerenkov radiation flashes on the other hand, are comparable; therefore, we conclude that the timing jitter between the laser and electron beams is less than 20 ps. This is an upper limit, and the actual value is most likely much less, since 20 ps corresponds to around 60 degrees of rf phase. For more accurate measurements, one would need to compare single-event pairs, but the amount of light produced by the electrons is quite small, making such a precise measurement a much more challenging task.

3.3.4.7 Coherent synchrotron radiation

As mentioned earlier, the photo-electron bunches produced by the X-band rf gun are very short, and streak camera measurements put an upper limit of approximately 2 ps on their duration; thus, they can radiate coherently at short wavelengths. This effect has been previously observed[104]. We have performed experiments where the bunches propagate through a corrugated waveguide and couple to the slow waves supported by that structure. To demonstrate that the

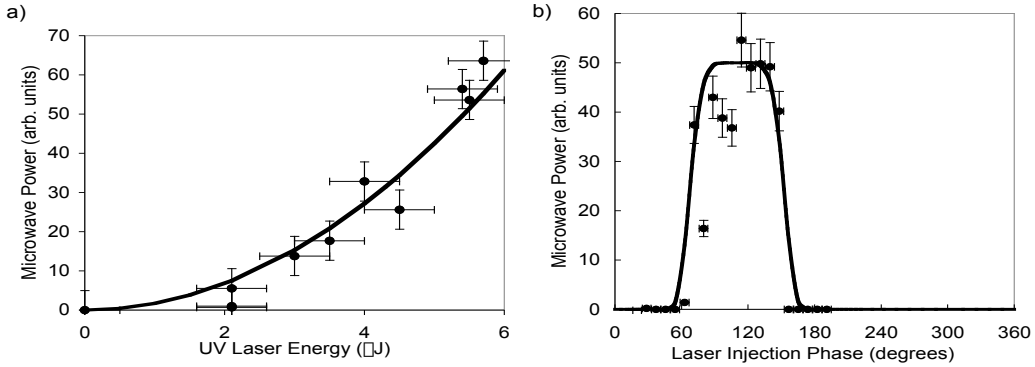

Figure62 Coherent synchrotron radiation measurements: a) radiation intensity as a function of laser energy with a quadratic fit, and b) radiation intensity as a function of rf phase relative to laser injection. The fit in (b) is the equation resulting in the fit of Figure 58 squared (only the total amplitude was varied, not the width).

radiation produced is, indeed, coherent, we have measured the power radiated as a function of the bunch charge. The variation of the bunch charge can be achieved in two different manners: on the one hand, the laser injection phase can be fixed, and the uv energy can be changed by using different combinations of calibrated neutral density filters, as shown in Figure 62a; on the other hand, the uv energy can be fixed, and the laser injection phase varied, thus taking advantage of the charge variation with phase, as studied in Sec. 3.3.4.2, and shown in Figure 62b.

The first experimental measurements consisted of measuring the rf power radiated by the bunches. A coupling horn gathered the radiation from the end of the beamline passing through a quartz window, and a waveguide section (collinear with the beamline) was used to provide low frequency cutoff before the wave reached the various frequency detectors used. We were able to confirm the emission of extremely short pulses of rf power up to Ka-band; at higher frequencies, the detector speed is believed to be insufficient: the characteristic time-scale of the radiation bursts is given by the slippage between the photo-electron bunch and the radiation pulse; as the corrugated waveguide section was only 10 cm long, the pulses were estimated to be 50-500 ps in duration, or approximately 2-20 rf cycles. At low frequency, between X-band and Ka-band, we were able to measure pulses with a FWHM of 500 ps, as illustrated in Figure 63; this is to be compared with the detector rise-time, specified at < 600 ps. At higher frequencies, the available detectors are not fast enough to follow the pulses.

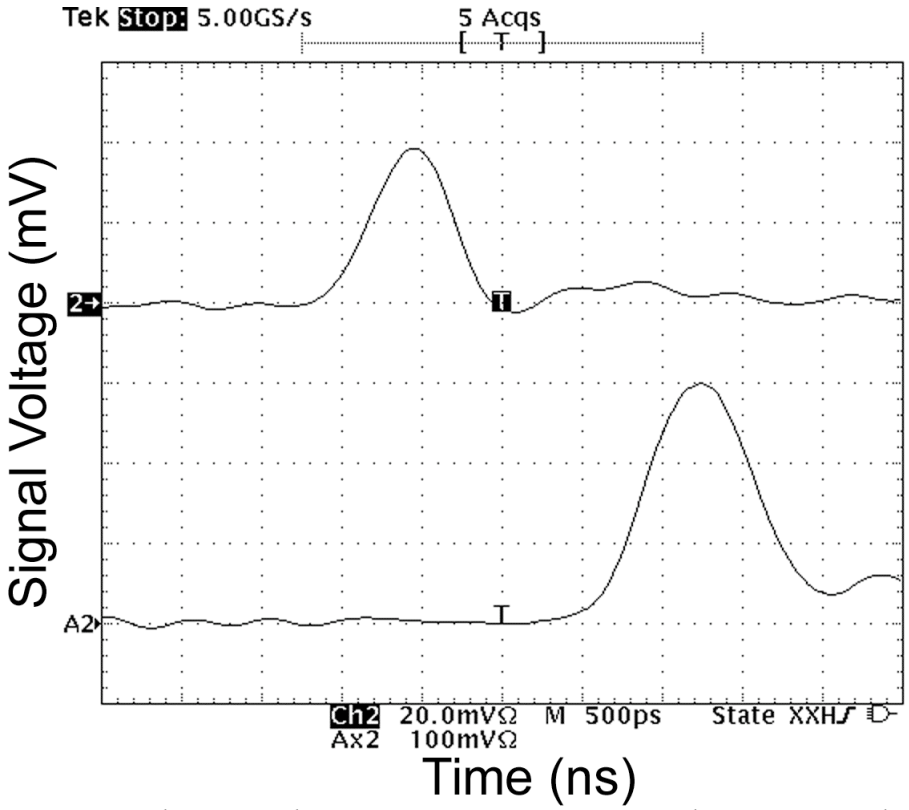

Figure 63 Coherent synchrotron radiation measurements. The upper trace shows the signal from an X-band microwave detector placed at the end of the beamline, and the lower trace shows the laser photodiode signal. This demonstrates the shortness of the microwave radiation burst (below the response time of the oscilloscope). The horizontal scale is 500 ps/div, and the vertical scale is 20 mV/div for the upper trace and 100 mV/div for the lower.

The quadratic scaling of the power radiated versus the bunch charge is very clearly demonstrated in Figure 62a; furthermore, we can take the supergaussian fit from Figure 58, properly squared, and match the rf data: the agreement is good (see Figure 62b), and confirms the coherence of the radiation emitted by the bunches. This has important potential application to millimeter-wave and far infrared coherent radiation generation, as the electron beam produced by the compact rf photo-injector are fully pre-bunched, and can radiated coherently up to the THz spectral region. In particular, theoretical work on pre-bunched free-electron masers[84] and the theory of coherence in synchrotron radiation[105] has shown that ultra-wideband, chirped-pulse radiation could be produced at power levels in excess of 2 MW, in the 100-200 GHz range. Such devices could be extremely useful for advanced radar systems, and as tools to probe materials and plasmas.

Finally, these measurements provide indirect confirmation that the electron bunches produced by our X-band photoinjector are very short. They also indicate, as pointed out by Carlsten[106], that one must pay very close attention to the beamline design for a system using this technology, as coherent synchrotron radiation typically degrades the high-brightness bunches because of correlated recoil effects. This implies that one must avoid bends, bellows, and cavities, which all strongly couple to the photoelectron bunches, and instead strive to provide smooth, continuous transverse boundaries for the beamline, in order to minimize unwanted radiation. Furthermore, the beamline can also be designed to avoid trapped modes, and to provide quenching of the lower frequency modes by a judicious combination of polarization and cut-off frequencies for those modes that couple most strongly with the pre-bunched beam.

Chapter 4. Interaction

The final step in creating a Thomson source is to bring the two beams discussed in Chapter 2 and Chapter 3 to the interaction point, and produce and diagnose the x-rays. This chapter will detail the set-up of the interaction region, arguably the most challenging part of source construction, and then will go through the various x-ray measurement that have been made.

4.1 Beam Interaction

There are several issues to be addressed in the design of the interaction, such as the fundamental interaction geometry, how to get the two beams to the interaction point, how to dump the beams after the interaction in a non-disruptive way, and how to verify the alignment of the beams.

4.1.1 Interaction Angle

The first decision to make in designing a Thomson source is the choice of interaction angle between the laser and the electron beam. Recall from Section 1.2.1.1 that

$$\square_{peak} = 2\square^2\left(1+\square\cos\square_{inc}\right), \tag{5}$$

so the peak energy is a direct function of the interaction angle. This is one consideration in choosing the interaction angle, but it is not in general the most significant one. The geometry of the interaction also has an effect on the x-ray pulse duration, the x-ray flux, and the allowable laser-electron jitter, all of which result from fairly simple geometrical considerations. To illustrate the relationships in this section, only 90° and 180° interactions will be discussed; other angles are result in effects with magnitudes somewhere between these two limits, and the best way to get quantitative values is through numerical simulations as discussed in [53].

The *pulse duration* dependence is illustrated schematically in Figure 64. X-rays are produced only when the laser and electron beams are overlapping. For a 90° interaction, with a laser duration shorter than the electron bunch length, the x-rays are produced during the transit

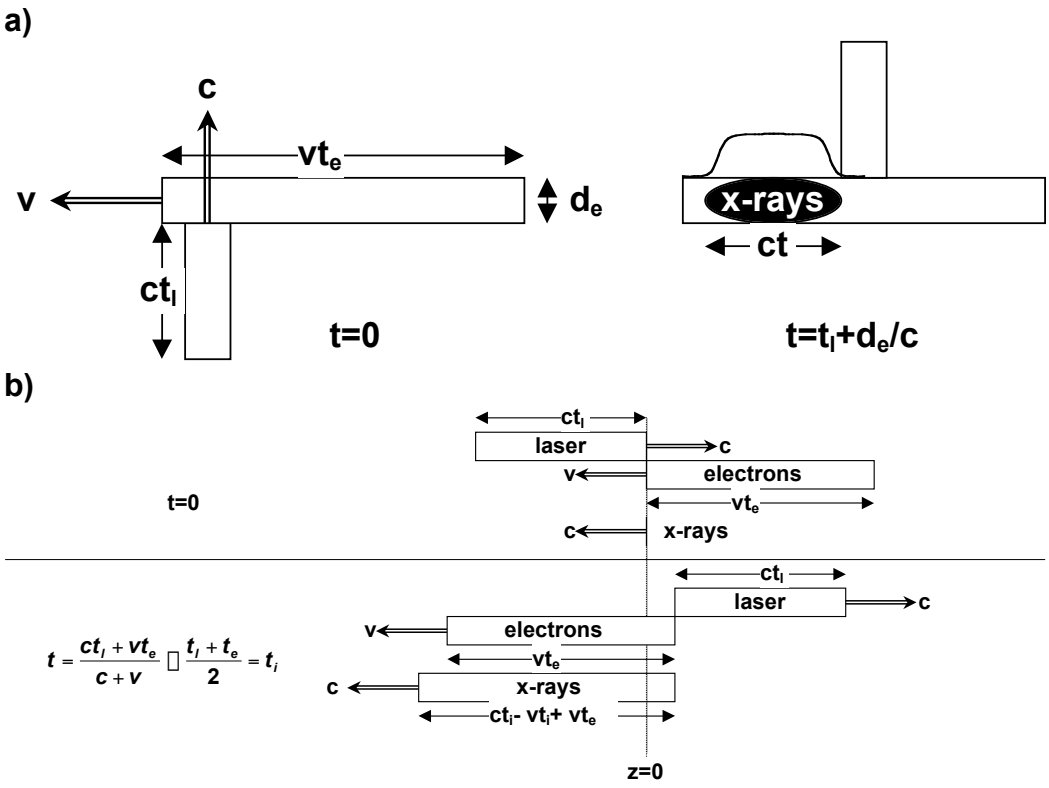

Figure 64 A schematic illustration of the duration of the produced x-ray pulses. a) 90° interaction, b) 180° interaction.

of the laser across the electrons (i.e. the duration of the laser pulse plus the width of the electron bunch.) This geometry therefore allows x-ray pulses with durations as short as ~100 fs. Conversely, in a 180° interaction, the laser passes through the entire electron beam. Because the electron beam is moving at a velocity near *c*, the produced x-rays essentially stay with the electron beam, and therefore the x-ray pulse length matches the electron bunch duration.

In fact, in this idealized geometry (collimated laser and electron beams), the duration of the laser bunch is almost irrelevant: the x-ray pulse length will grow by the amount the x-rays lead the electron beam over the course of the interaction. This leads to an x-ray duration of

$$\Delta t_{x\text{-}ray} = \frac{(c - v)\Delta t_{laser} + v\Delta t_{electron}}{c} = (1 - \beta)\Delta t_{laser} + \beta\Delta t_{electron} \approx \frac{\Delta t_{laser}}{2\gamma^2} + \Delta t_{electron}.$$

For a 50 MeV electron beam, $\gamma \approx 100$ so the laser pulse can be 20,000 times longer than the electron pulse and still only double the x-ray pulse length. A 3 ps electron bunch and a 60 ns laser pulse, in a head on geometry, will produce an x-ray pulse ~6ps long. Of course, a real interaction will not occur in this idealized geometry. To maximize the x-ray flux, the density of the electrons

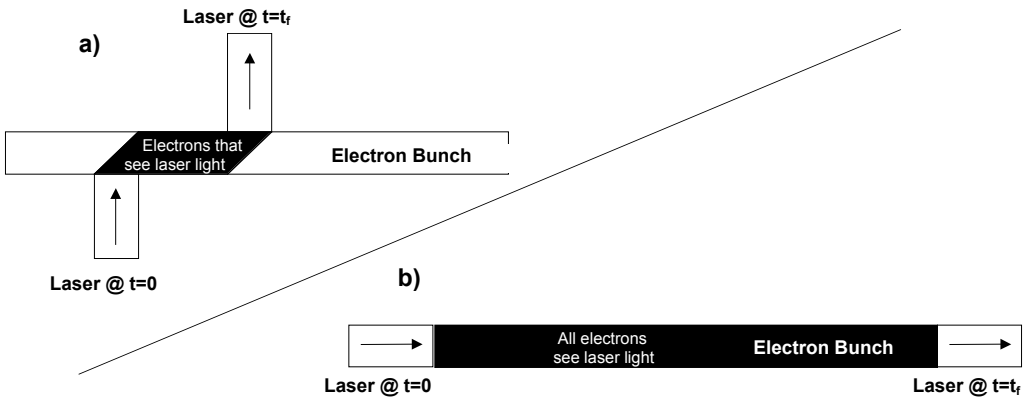

Figure 65 A schematic illustration of the flux dependence on the interaction geometry. a) in the 90° geometry, only some electrons interact with the laser; the others go to waste. b) in the 180° geometry, the laser sweeps through all the electrons, maximizing the potential collisions.

and photons needs to be maximized, and so both the laser and the electron beam will be focused. The divergence of the laser and electron beam then give a longitudinal limit to the interaction region, defined by the laser Rayleigh range and the electron beta function (see Figure 66). In this case, the laser pulse duration starts to affect not the x-ray pulse duration but the x-ray flux. Photons that aren't within the laser focus region while the electron beam is at the focus are essentially wasted; they will interact with the electrons in a much less dense regime, and so will produce far fewer x-rays. The focus region is typically a few millimeters long, so having a laser with a pulse length much longer that an few picosecond is not useful.

The *flux* dependence is illustrated in Figure 65. In a 90° interaction, most of the electrons never interact with the laser field. The x-ray flux is directly proportional to the number of electrons and photons that interact, so if the electrons only see a fraction of the photons, only a fraction of the potential x-rays will be produced. In a 180° interaction, all the photons in the laser bunch sweep through the entire electron beam, as illustrated in Figure 65b. Naturally, the limited overlap of the 90° geometry can be remediated by lengthening the laser pulse, but the flux is still lower than for a 180° interaction. For example, the photons at the front of the laser pulse would interact only with the electrons as the front of the electron bunch, so the total number of collisions would still be reduced from 180° levels. Additionally, this defeats the motivation for choosing a 90° interaction in the first place, namely the shorter-pulse x-ray production. An alternative option has been discussed[107] which would both allow the laser to interact with most of the electrons *and*

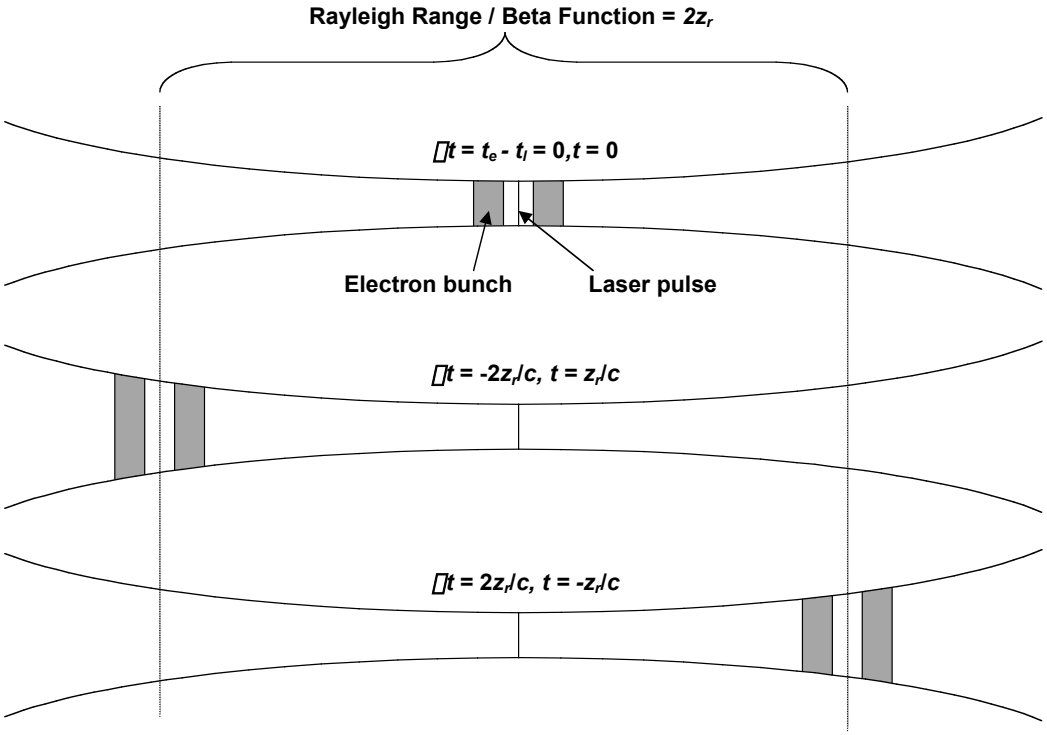

Figure 66 Diagram showing the allowable laser-electron jitter in a 180° interaction geometry.

produce a short pulse (approximately the duration of the laser pulse) by scattering at an angle close to zero degrees. In this case, the x-rays, produced within the envelope of the laser bunch, copropagate with the laser and so are always within that envelope; the electron bunch length then becomes irrelevant (except for the same Rayleigh range/beta function overlap caveat made above). Additionally, the laser interacts with all the electrons, so the flux is maximized. The catch here is that, from Equation (5), a scattering angle close to zero does not yield much upshift as the $\cos \theta_{inc}$ term approaches –1. This means very large accelerators are needed to make high-energy beams: 180 MeV electrons become necessary to produce 8 keV x-rays in this scheme, whereas in a 180° interaction only 18 MeV electrons are needed).

The third consideration in the choice of an interaction geometry is the acceptable alignment *jitter*. In terms of pointing stability, a 90° interaction requires the laser to hit an electron bunch that is (in the PLEIADES system) 20 μm x 1.5 mm in size, while in a 180° geometry the target is 20 μm x 20 μm. Although this makes the 90° interaction sound simpler, it is not actually that significant of a difference. Once the pointing jitter is down to 20 μm in one dimension, which

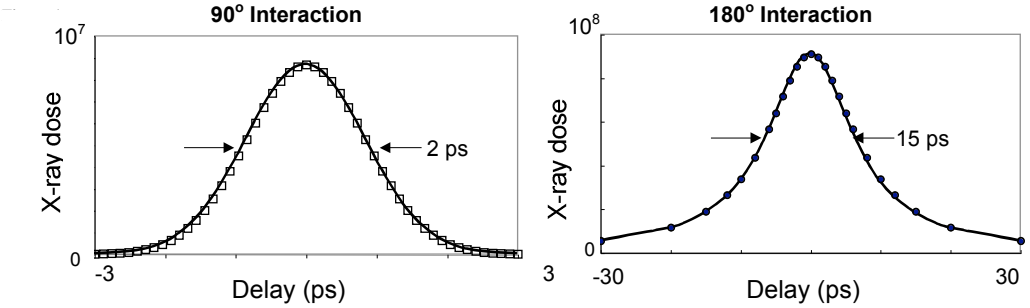

Figure 67 Simulation data showing the effect of interaction geometry on the x-ray flux and the allowable jitter between the laser and electron beams.

is necessary for either interaction, getting a similar pointing jitter in the other dimension is fairly straightforward. A much more significant consideration is the allowable timing jitter. In a 90° scattering geometry, the laser must arrive at the interaction point while the electron beam is present. This means the laser must arrive within a window equal to the length of the electron bunch, otherwise it will miss the beam. Therefore the timing jitter must be less than a couple of picosecond (or even a few hundred femtoseconds if bunch compression, as discussed in Section 5.1, is to be used). For a 180° interaction, however, the requirement becomes much less stringent. Figure 66 illustrates the interaction geometry. In this figure, $t_e = t = 0$ is defined to be the time at which the electron beam arrives at the focal point, and t_l is the time when the laser arrives at the focal point. If the laser is timed to arrive at the interaction point between $t = -\frac{2z_r}{c}$ and $t = \frac{2z_r}{c}$, the two beams will still interact within the focusing region, and still produce an appreciable x-ray flux. Because this length is generally on the order of several millimeters, the timing jitter can be several picoseconds and still produce reasonable x-ray fluxes.

Figure 67 illustrates both the flux and jitter dependencies on the interaction geometry. Simulations of the x-ray flux as a function of delay between the laser and electron bunch are shown. In a 180° interaction geometry, with a 50-fs, 20-μm diameter laser pulse and a 2-ps, 20-μm, 5-mm-mrad emittance electron beam, the full-width at half-maximum (FWHM) of the x-rays produced as a function of the delay between the arrival of the laser pulse and the arrival of the electron bunch at the focus is 15 ps. For the same beams in a 90° geometry, the FWHM is only 2 ps, and the number of x-rays produced drops by a factor of 10. Also, at a shallow interaction angle of 172°, simulations show that the interaction window drops to 2.3 ps; this lengthening of

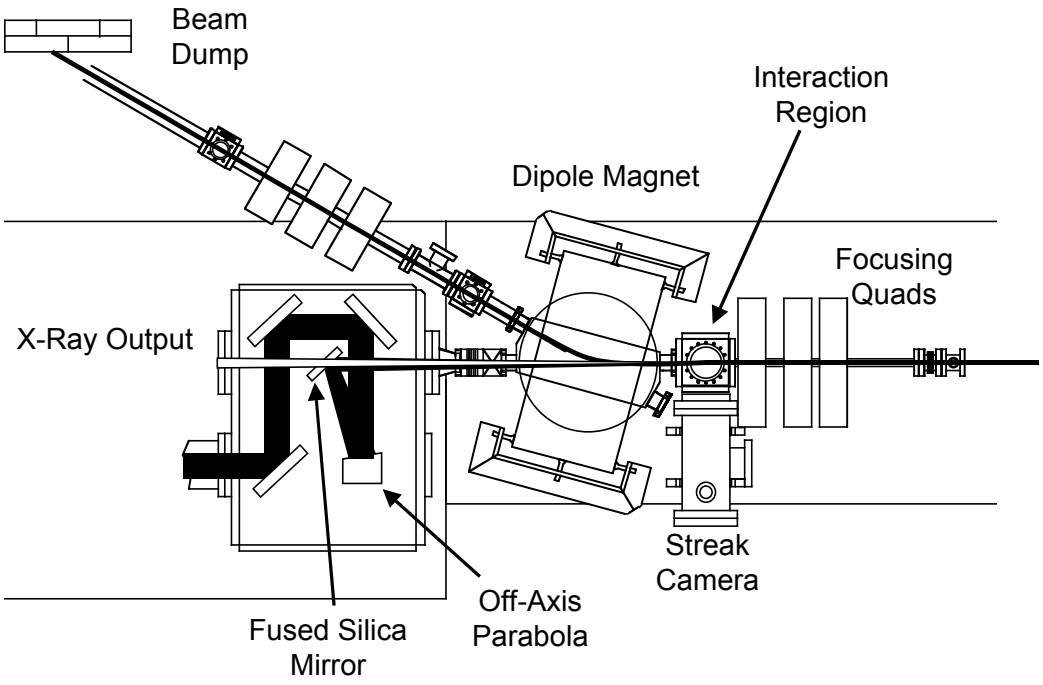

Figure 68 Layout of the PLEIADES experimental interaction region, showing the laser, electron, and x-ray beam paths

the allowable jitter depends on the two beams being completely overlapped within the focusing region.

Because of concerns about the temporal stability of the laser system and the ability to detect low x-ray fluxes, as well as the fact that x-ray pulse durations of a few ps would be sufficient for potential early experiments, we opted to build a system in the 180°, head-on scattering configuration.

4.1.2 PLEIADES Experimental Set-up

The layout of the PLEIADES interaction region is shown in Figure 68. Because a 180° configuration was chosen for the interaction, finding a scheme to get the laser and electron beams in and out of the interaction region is complicated. The electron beam goes straight into the interaction region via the electron focusing optics, along the main linac beamline. It is focused by a set of quadrupole magnets with a peak magnetic field gradient of 15 T/m. To aid alignment at the focus, two cross-oriented dipole magnets steer the beam into this magnetic lens. This beam is imaged on the alignment cube, discussed in the next section, and the focus is optimized to give

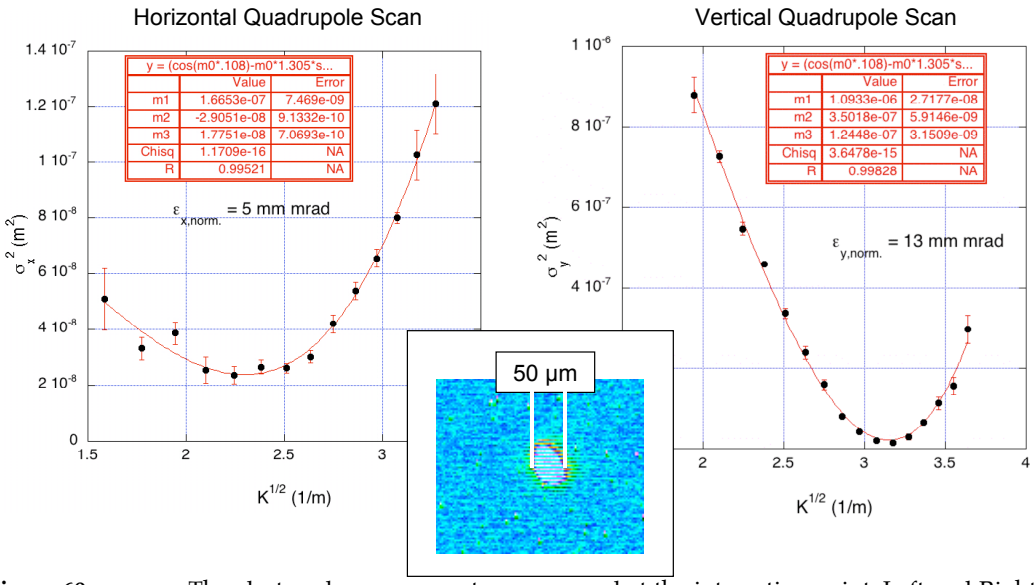

Figure 69 The electron beam parameters measured at the interaction point. Left and Right: Quad scan results, showing an emittance of 5 x 13 mm mrad. Inset: an image of the electron spot size.

the smallest spot. This optimization effectively fixes the transverse position of the focal spot, and gives the target for the laser alignment. Measurements of the e-beam at the focus have shown a spot size of 50 μm rms, and rms beam emittances ε_x = 5 mm mrad and ε_y = 13 mm mrad, which were measured using a standard quadrupole scan technique[85] (see Figure 69). These numbers vary day to day, but are generally within 20% of these values.

Following the interaction, the diverging electron beam must be bent away from the x-rays (which copropagate with the electrons) and dumped. Because the electrons will produce a significant amount of Bremsstrahlung radiation when stopped, they must be sent to a well shielded beam dump to avoid adding a large amount of background noise to the measurements. The separation of the electrons from the x-rays is done via a dipole magnet that bends the beam 30° from the beamline axis. This same dipole is also used to measure the beam energy at the interaction point. An image of the beam after the dipole, shown in Figure 70, shows a 57 MeV electron beam (γ = 112) with an energy spread of $\Delta\gamma/\gamma$=0.2%. This dipole can work with electron beam energies up to about 90 MeV, at which point the magnetic field saturates and it can no longer bend the beam far enough. This turns out to be the limiting factor for x-ray energies PLEIADES can produce, not the amount of acceleration available in the linac sections The space

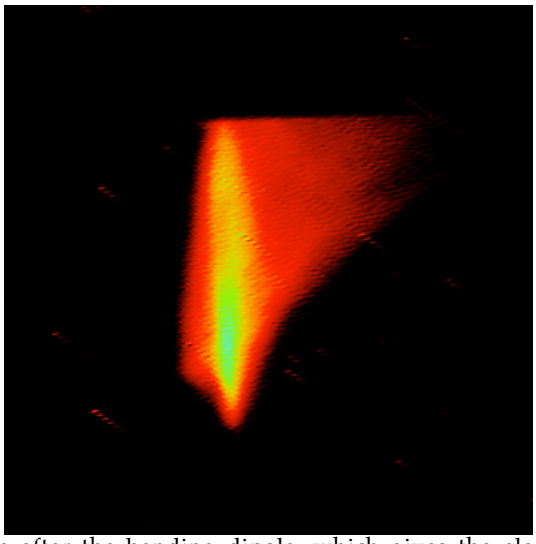

Figure 70 Image after the bending dipole, which gives the electron beam energy and energy spread. This image shows an energy of 57 MeV with 0.2% energy spread.

required to fit this dipole limits how close the final laser optics can be, and therefore how tightly the laser spot can be focused.

The ir laser pulse from FALCON that is to be scattered comes in to the interaction region offset from the electron beamline by 14", and is focused by a 60" focal length, 12° off-axis parabolic mirror. The focusing beam is then directed to the interaction region by a 3" diameter, 0.5" thick BK7 dielectric mirror. This mirror becomes important during the data analysis, as the x-rays must pass through it to get to the detectors. The mirror is mounted on a stepper-motor-controlled mount, which allows for remote control of the pointing of the laser focus at the interaction point, and its alignment to the electron spot. The longitudinal focus position is set by the distance from the parabola to the interaction point, and is fixed. The focusing quadrupole settings are adjusted to minimize the electron spot size at this longitudinal focal position. The laser spot is observed to have a mean $1/e^2$ waist radius of 50.5 μm (58.9 μm FWHM) and a mean M^2 value of 2.32 (Figure 71). The large value for M^2 compared to the values measured after the 2nd amplifier (Figure 16) is due to clipping in the transport chain. To dispose of the residual laser energy, the beam is allowed to propagate down the linac beamline. As it continues to expand from the focus, the energy is dumped along the walls of the beamline. Using an ir viewer, the light from the beam can be seen up to about 15 feet after the interaction point; further upstream in the accelerator it is not readily visible. However, the light was detected at the photoinjector

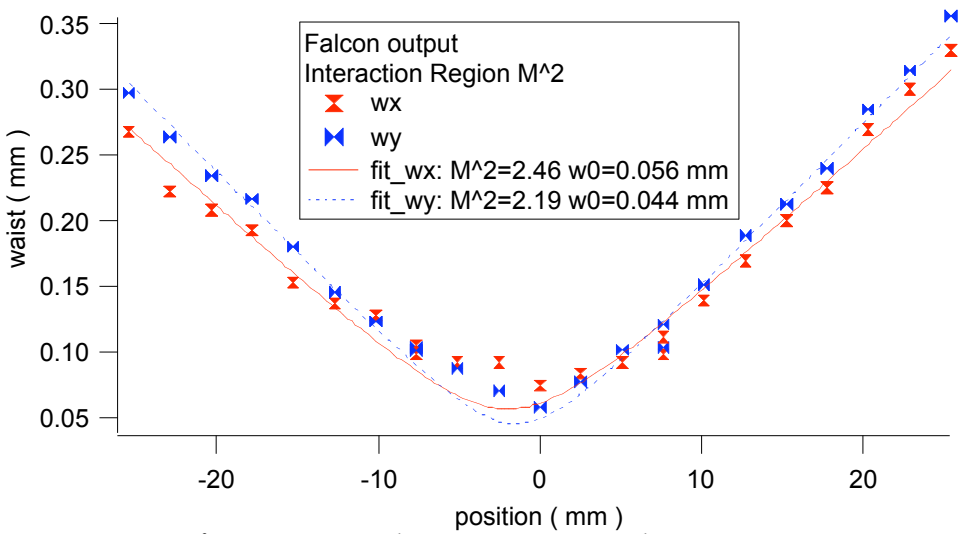

Figure 71 M^2 measurement at the interaction point of the FALCON beam.

end of the accelerator on the energy meter that monitors the PLS laser pulse, 57 feet from the interaction point.

4.1.3 Alignment Procedure

Once the two beams are in the interaction region is the first half of the story, all that remains is to align them correctly with each other. Alignment of the two focal spots was performed with the aid of a 0.3" aluminum cube polished to optical flatness. The cube is mounted on a three-axis translation stage with its faces oriented normal to the beamline in the vertical direction, and at 45° to the beamline in the horizontal direction, as diagrammed in Figure 72. Because the laser beam reflects from the surface, the focus at the surface of the cube can be imaged into a CCD camera. To avoid damaging the cube or camera, the ir laser pulse energy is reduced by a combination of mistiming the pump lasers to the □-4-pass amplifier and inserting neutral density filters to attenuate the beam by a factor of approximately 10^8. Meanwhile, when the electron beam strikes the cube, it produces optical transition radiation (OTR), which can also be imaged by the CCD camera. The vertical alignment of the two beams is then readily apparent, and the horizontal alignment is determined by positioning the cube such that both beams just hit the cube edge. Generally, the procedure is to place the cube at the laser focus, which is fixed by the parabola; optimize the electron beam focus on the cube, which sets the optimal electron beam

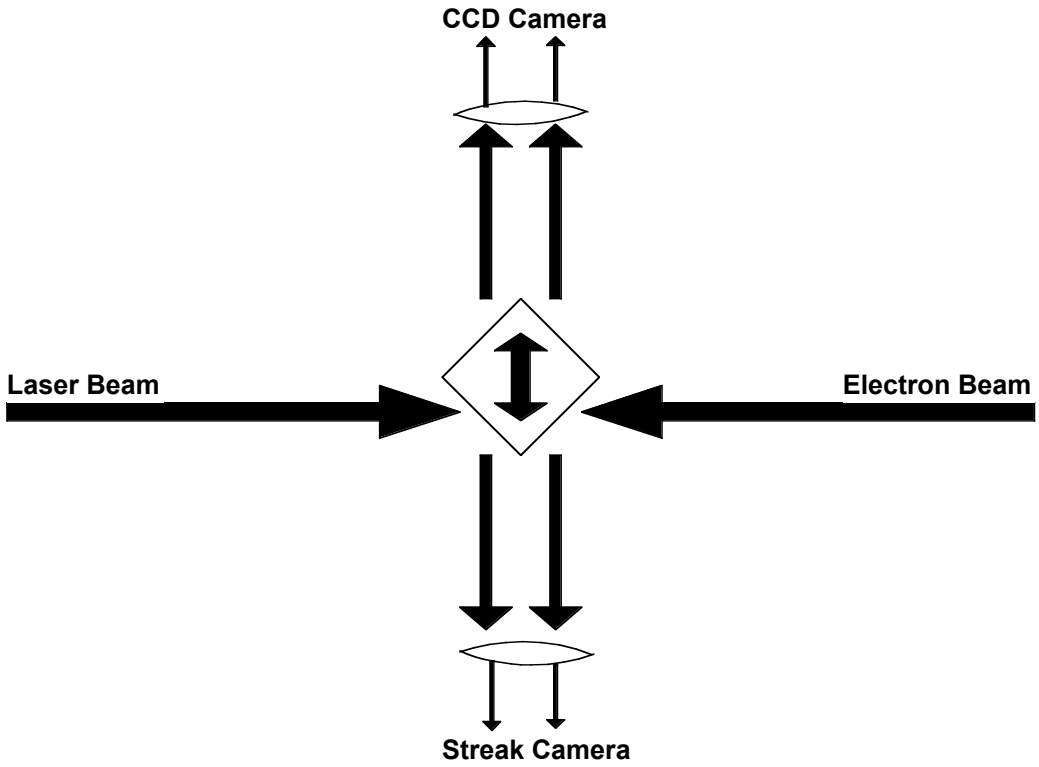

Figure 72 The system used to align the laser and electron beams spatially and temporally. The aluminum cube can slide in all three dimensions, allowing the tip to be placed at the laser focus, and the reflected beams to be sent to either the CCD camera or the streak camera.

transverse position, and then steer the laser beam laterally to align to the electron beam. To successfully align the beams, it is important that the cube face be optically flat; any curvature on the surface will cause the cube surface to act as a lens, preventing accurate determination of the laser focal spot, and the alignment procedure will fail.

Temporal alignment is more complex than the spatial alignment because the propagation times for the FALCON laser and the PLS/electrons, which are set by path lengths that are approximately 70 meters long, must be matched to within a few picoseconds. There are three steps to the initial synchronization. First, a beam-current pickoff and an ir photodiode are used to determine the initial timing. The electron beam propagating through the interaction area generates a short pulse magnetic field, which produces current in two 100-ohm junctions in the pickoff. The generated signal is then detected by an oscilloscope as ~150 ps FWHM pulses. Similar accuracy is obtained for the arrival time of the laser by using a fast infrared UHS 016 photodiode. By selecting the correct oscillator pulse to switch into the FALCON regenerative

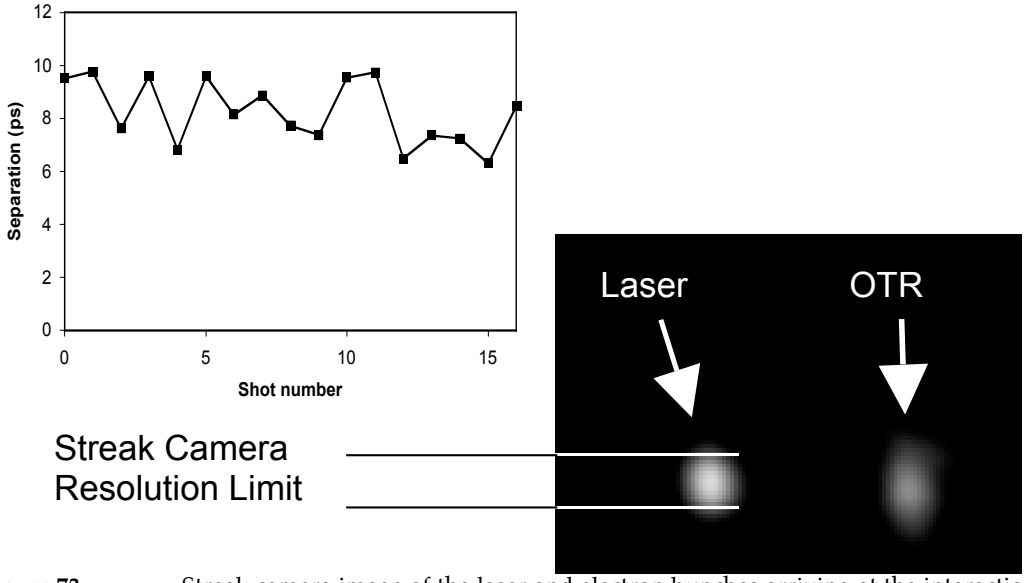

Figure 73 Streak camera image of the laser and electron bunches arriving at the interaction point and hitting the Al cube. Since the laser pulse is ~50fs in duration, the size of the laser spot illustrates the resolution of the streak camera. The plot shows the measured separation of the laser and OTR spots for several shots; this gives a measure of the laser-electron jitter.

amplifier, relative to the one switched into the PLS regenerative amplifier, we are able to get the electron and laser arrival time difference to less than 12 ns (the spacing between pairs of oscillator pulses).

Second, for more accurate timing, we use a Nikon Nikkor 50 mm f/1.4 lens to image the OTR and the laser light reflected from the cube onto the 100-μm slit of an Imacon 500 Series streak camera. This camera uses an S20 photo-cathode with a quantum efficiency greater than 5% over the visible wavelengths, which makes simultaneous streaking of the OTR and drive laser light possible. Using a combination of this streak camera and the current pick-off/photodiode signals mentioned above, the laser and electron paths are brought to within a few tens of picoseconds by manually sliding the retroreflecting roof mirror in the FALCON compressor along a 2-m rail (see Figure 19b). Because this mirror is located between the second and third grating strike in the compressor, its position does not have a significant effect on the compressed pulse.

The third and final stage of temporal alignment is performed using the streak camera at its highest sweep speed, 18.7 ps/mm, which gives us temporal resolution of 2-5 ps, limited by the

spacing on the microchannel plate that is used as an amplifier for the output phosphor and by the entrance slit size. Using this signal and a motorized stage under the same roof mirror in the compressor, we can synchronize the laser and electron beam arrival to the resolution of the streak camera. This measurement also gives us the relative timing jitter, which is seen to be below the streak camera resolution. Attempts at further optimizing the timing by maximizing the x-ray signal directly as a function of the delay between the pulses yield no improvement, indicating that the temporal overlap achieved with the 2-ps resolution of the streak camera was sufficient for the 180° interaction geometry.

4.2 X-Ray Production

Once the spatial and temporal alignment is complete, production of x-rays is straightforward. This section presents several of the measurements of the x-ray source that have been made to date, with an end goal of trying to measure the actual spectral brightness of this system. This requires measurement of the x-ray flux, spectrum, duration, spot size, and divergence (recall that brightness is measured in units of photons·s^{-1}·mm^{-2}·$mrad^{-2}$·(0.1% BW)$^{-1}$). Unfortunately, x-ray pulse duration and spot-size measurements have not yet been performed, but the theoretical expectations for these numbers based on measured laser and electron pulse lengths and spot sizes provide reliable numbers to use in the calculations.

4.2.1 X-Ray Diagnostics

The primary diagnostic we have for measurement of the x-rays is an x-ray CCD camera system. It consists of a 145-μm thick CsI(Tl) scintillator that is coupled by a 3:1 reducing fiber optic bundle to the input 1:1 bundle of an optical Princeton Instruments PI-SCX1300 camera. This is a 16-bit, 1340x1300-pixel CCD camera. The chip size is 2.54 x 2.54 cm, which gives a field of view as large as 7x7 cm, with a pixel size of 60 μm x 60 μm. The scintillator, which is protected by a 0.5-mm beryllium (Be) filter to keep stray light out, provides a photon detection quantum efficiency of 0.4 at 60 keV.

The x-ray CCD system was calibrated using a ^{241}Americium (^{241}Am) radioactive source and a single-photon counting Ge(Li) detector. The ^{241}Am source is mounted in a housing with

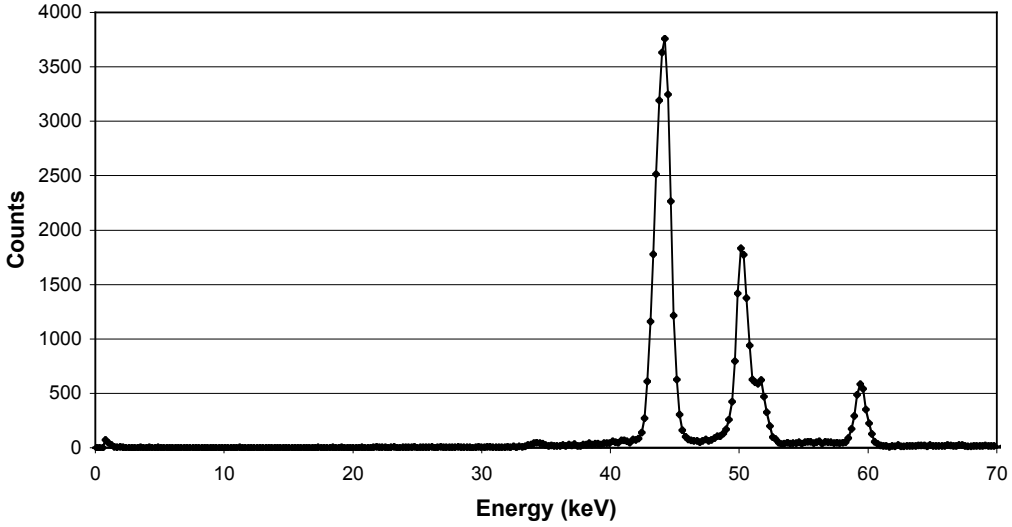

Figure 74 ^{241}Am source spectrum, as recorded by a Ge(Li) detector.

several different metal foils that can be used to generate fluorescence lines, and is referred to as a "pocket synchrotron". For the calibration, a terbium (Tb) foil was used, giving fluorescence lines at 44.5 keV and 50.3 keV in addition to the ^{241}Am 59.5 keV line. The Ge(Li) crystal is 19.8 mm thick and has a detection efficiency of ~1 for the energies of interest for this experiment, and so made an ideal instrument for calibrating the x-ray CCD detection efficiency.

The first step of the calibration is to determine how many photons the source is producing. The source is placed at the entrance window of the Ge(Li) detector, and the spectrum is recorded for 1 minute. A sample spectrum is shown in Figure 74. The second step is to determine how many counts the x-ray CCD camera sees from the source. First, a one minute integration is performed with no source to determine a background level. Then, the ^{241}Am source is placed against the Be window of the CCD system, and another one minute exposure is performed. The background and signal images are integrated over the whole CCD, the two numbers are subtracted, and the result gives the number of counts detected by the CCD due to the source. Alternatively, the signal and background images can be subtracted from each other, and the image of the source x-rays can be fit with a Gaussian curve, the integral of which can give the total number of counts. Both methods gave comparable numbers.

The final step is to take the ratio of the number of counts measured to the amount of energy deposited in the scintillator to find the counts/keV for the system. The curve of Figure 74,

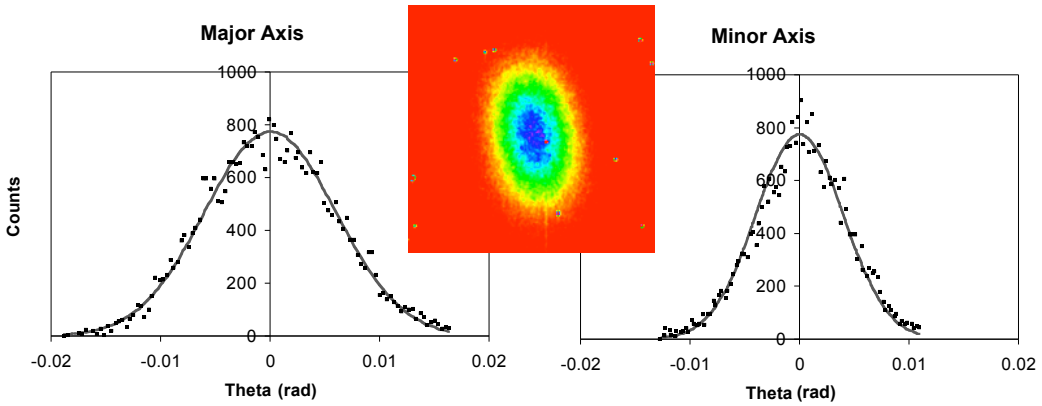

Figure 75 Left and Right: lineouts through the profile with Gaussian fits. Inset: a sample x-ray profile.

$N_{Am}(E)$, is multiplied by the energy E. This curve is then multiplied by the sensitivity of the CsI scintillator as a function of energy, $\eta_{CsI}(E)$ (see Figure 76). The total energy deposited into the scintillator is then

$$E_{dep} = \int EN_{Am}(E)\eta_{CsI}(E)dE.$$

Dividing the number of counts recorded by the CCD camera by the total energy deposited in the camera gives the sensitivity of the camera, η_{CCD}, which is 0.12 counts/keV. This accounts for the conversion ratio of the CsI(Tl) crystal, coupling losses into the fiber taper, and CCD quantum efficiency.

4.2.2 Flux Measurement

A typical x-ray CCD image of the Thomson x-rays is shown in Figure 75, along with

Table V — Representative x-ray production parameters

Electron Bunch Charge	250 pC
Electron Energy	57 MeV
Electron Spot Size	59 x 38 μm rms
Electron Divergence	1.8 x 3.1 mrad
Electron Emittance	4.2 x 11.2 mm-mrad
Laser Energy	400 mJ
Laser Wavelength	810 nm
Laser Spot Size	36 μm $1/e^2$ radius
Peak X-Ray Energy	77 keV

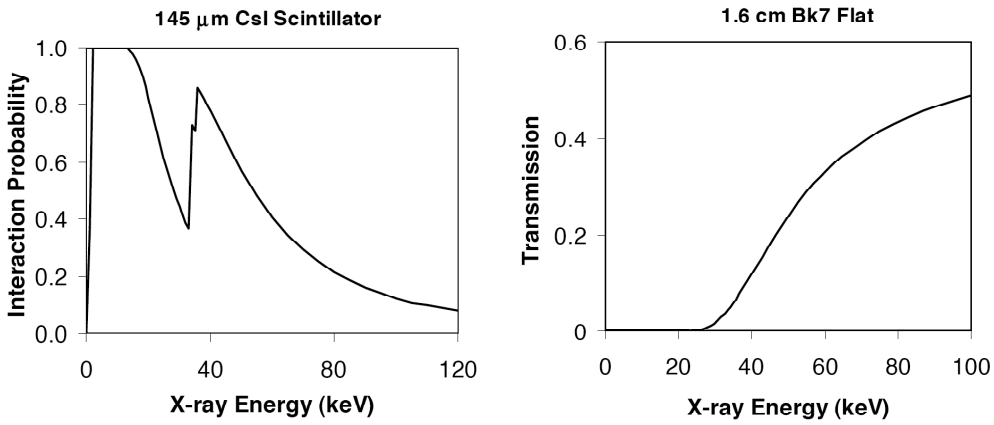

Figure 76 Left: spectral response of the CsI(Tl) scintillator, Right: transmission of the 0.5", 40°, BK7 final turning mirror.

lineouts along the major and minor axes of the ellipse. This spot was produced with the laser and electron parameters shown in Table V. The asymmetry of the spot is a combination of the laser polarization effect discussed in Section 1.2.1.2, and the asymmetric emittance of the electron bunch as measured in Section 4.1.2, which results in a larger electron beam divergence in the vertical direction than the horizontal direction, and therefore a larger vertical x-ray divergence as well. The measured x and y divergences of the beam are 3.1 mrad and 5.8 mrad , respectively.

To compare this result with what the theory predicts, the code from [53] is used. The electron bunch is constructed from a 6D Gaussian distribution of particles with spot sizes and divergences as given by the measurements at the interaction point shown in Table V. The code gives $N(\theta_x,\theta_y,\omega)$, the number of photons emitted as a function of direction and frequency. To allow for a direct comparison of the x-rays measured with the profile expected, the transmission to the CCD must be accounted for; the correlation between position and energy in the beam that results from Eq. (24) means the beam shape depends on the energy dependant transmission of the BK7 final turning flat ($T_{BK7}(\omega)$), and the spectral response of the CsI scintillator ($\eta_{CsI}(\omega)$). BK7 consists of 67% SiO_2, 12.6% B_2O_3, 8.1% Na_2O, and 12.3% K_2O by weight, so the transmission curve can be calculated from known attenuation factors for each element[108] and the density of the material, which is 2.51 g/cm3, and is shown in Figure 76. The greater attenuation of the lower energy x-rays in the BK7 substrate means the measured profile will be narrower than expected. What is observed on the camera is

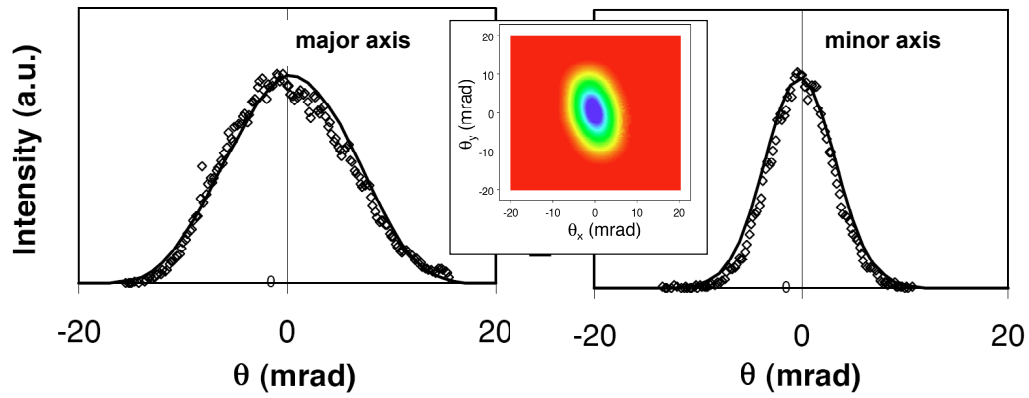

Figure 77 Left and right: the measured and theoretical profile lineouts. Inset: theoretical x-ray profile for the measured laser and x-ray parameters.

$$F(\theta_x,\theta_y) = \int \hbar\omega N(\theta_x,\theta_y,\omega) T_{BK7}(\omega) \eta_{CsI}(\omega) \eta_{CCD} d\omega,$$

where η_{CCD} is the detection efficiency of the CCD discussed in Section 4.2.1. Figure 77 shows the theoretical profile and the measured and predicted lineouts along the major and minor axes of the profiles, which shows very good agreement. To measure the flux of the x-rays, first the Gaussian fit to the measured x-ray profile is integrated to obtain a total number of counts. Then the theoretical profile can be similarly integrated to give a total predicted number of counts. Because the number of photons produced in the code is known, the ratio of the difference in counts can lead to an inference of the total flux of x-rays produced at the source

$$N_{measured} = \frac{\iiint N_{Theoretical}(\theta_x,\theta_y,\omega) d\theta_x d\theta_y d\omega}{\iint F_{Theoretical}(\theta_x,\theta_y) d\theta_x d\theta_y} \iint F_{measured}(\theta_x,\theta_y) d\theta_x d\theta_y,$$

and gives an estimate of 4.6×10^6 photons/shot. The caveat here is that this assumes the Thomson spectrum matches what theory says it should; a spectrum is required to confirm this. However, the fact that the theoretical and measured profiles match so well, despite such a strong spectral dependence of the transmission functions, implies the spectrum is not too far off from the theoretical value.

This same measurement was performed with x-ray peak energies ranging from 40-140 keV, with similar flux results for all energies. More significantly, the entire range was spanned in one evening of data taking, which demonstrates the ease of tuning with this method. A second measurement that was performed was a scan of the delay of the laser relative to the electron

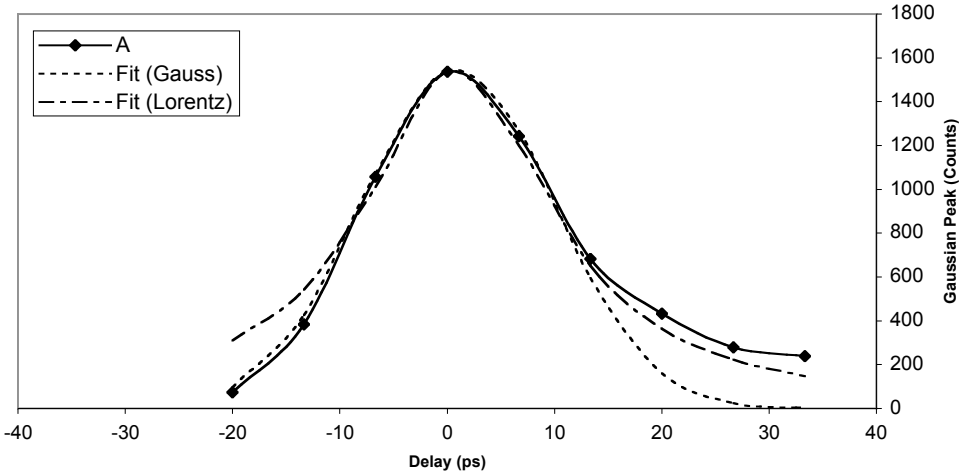

Figure 78 A plot of the x-ray amplitude as a function of laser delay relative to the electron beam, and two fits, one Gaussian and one Lorentzian, with the same fit parameters.

beam, recording the change in the x-ray flux. The CCD images for each delay were captured and fit with a 2D Gaussian function. The Gaussian amplitudes are plotted in Figure 78. Also shown are two fits, one to a Gaussian,

$$F_G(t) = Ae^{-4\ln 2\left(\frac{t-t_0}{\Delta_w}\right)^2},$$

and one to a Lorentzian

$$F_L(t) = \frac{A}{1+\left(\frac{2(t-t_0)}{\Delta_t}\right)^2}.$$

Both use the same fit parameters: A = 1550, t_0 = 1, and Δ_t = 21. This width corresponds to a FWHM for the signal of 6.3 mm. The width of the interaction region should correspond to the smaller of the laser Rayleigh range or the electron beta function. The Rayleigh range is given by

$$2z_r = \frac{2\pi\omega_0^2}{M^2\lambda} = 8.4 \text{ mm},$$

which corresponds well with the observed temporal profile. This also corresponds well with Figure 67, and illustrates the relative insensitivity to jitter of the 180° scattering geometry. The width is wider than shown in Figure 67, however the spot size and M^2 are both larger, so the Rayleigh range is also larger.

4.2.3 Spectral Measurement

To measure the x-ray spectrum, there are three methods available. The first is to use energy-sensitive detectors, such as the Ge(Li) detector used to calibrate the x-ray CCD camera. Also available is an AmpTek XR-100CR x-ray diode, with a 25 mm^2 active area. Both these devices work by measuring the amount of energy absorbed by the crystal during an integration period, which is typically on the order of microseconds. This means they can only see one x-ray photon per shot to produce an accurate spectrum. The problem with using these devices is that there is a large, high-energy background where the x-rays are to be detected both because the electron beam is dumped nearby, and also because the detector looks straight down the linac: any beam scraping or dark current can generate x-rays up to the energy of the electron beam (tens of MeV). Providing sufficient shielding from these x-rays would completely block the x-rays under study. Good shielding, a small pinhole aperture, and careful data rejection to eliminate noisy shots might be able to produce a reliable spectrum, but this has not been attempted yet due to time constraints on data taking.

The second method to measure the spectrum is to use the narrow bandwidth of a Bragg crystal to measure the spectrum. A bent-crystal x-ray spectrometer[109] has been built for this purpose, which is designed to be used in conjunction with the CCD camera, but comparatively low flux of x-rays at any given energy, coupled with the large backgrounds seen on the camera, make the diffracted spot impossible to see. Using a reflective Bragg crystal is hindered by the fact that the low energy (< 40 keV) x-ray are almost fully absorbed by the BK7 substrate through which they must pass to reach the detector, and to measure the higher energies requires very small angles on the crystals. The gated, intensified CCD camera discussed in Section 5.1 would improve the chances of the spectrometer signal being detected, and it is expected that a LiF crystal could be used as a monochromator to directly determine the spectrum; both of these will be tried in the future when time allows.

This leaves one final method of determining the spectrum. In most materials, the attenuation of x-rays is a very strong function of energy. Therefore, by filtering the signal with a material with a known attenuation, we can infer details about the spectrum. Ideally, one would

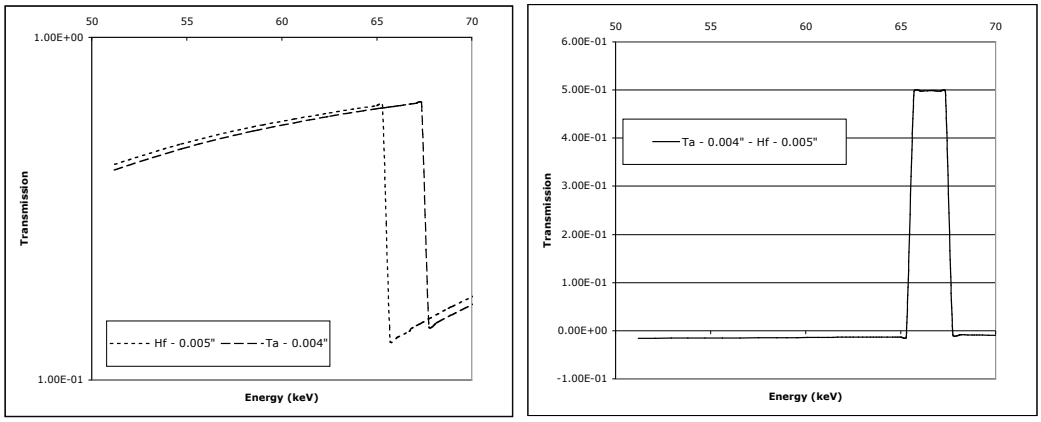

Figure 79 Left: the transmission through 0.005" Hf and 0.004" Ta foils. Right: the difference in transmission between the two; this is the net trasmission if a Hf image is subtracted from a Ta image.

use a filter with a square profile, so that in a range from E_i to $E_i + \Delta E$ the transmission is one, and elsewhere it is zero. This is very similar in effect to using a crystal to diffract the beam; in the diffraction case, only energies in a narrow range get bent out of the main beam path for detection, just as only energies in a narrow range get transmitted by our hypothetical filter material. Unfortunately, such a material isn't available, so other schemes must be tried.

One possibility is to make use of the sharp cutoff in transmission of a material near its K-edge (see Section 0). Figure 79 shows the transmission through hafnium (Hf) and tantalum (Ta) foils as a function of energy[108]. If two consecutive images of the x-ray beam were to be taken, one with the Hf foil in the beamline and one with the Ta foil in the beamline, the images could be subtracted from each other, leaving a net spectral sensitivity as shown on the right side of Figure 79. Using numerous pairs of foil, coarse spectral data can be obtained this way; the resolution of course is limited to the differences in K-edge locations, typically 1-2 keV apart from element to element. The problem with this method is numerous foils of numerous metals must be obtained to perform the measurement. On the experimental side, the problem in implementing this scheme was that the beam wasn't stable enough shot to shot to get a reliable measurement; the location of the x-ray spot would change, as would the intensity. Once these stability issues get addressed, there is a good chance this method would be experimentally feasible, if not too costly for foil procurement.

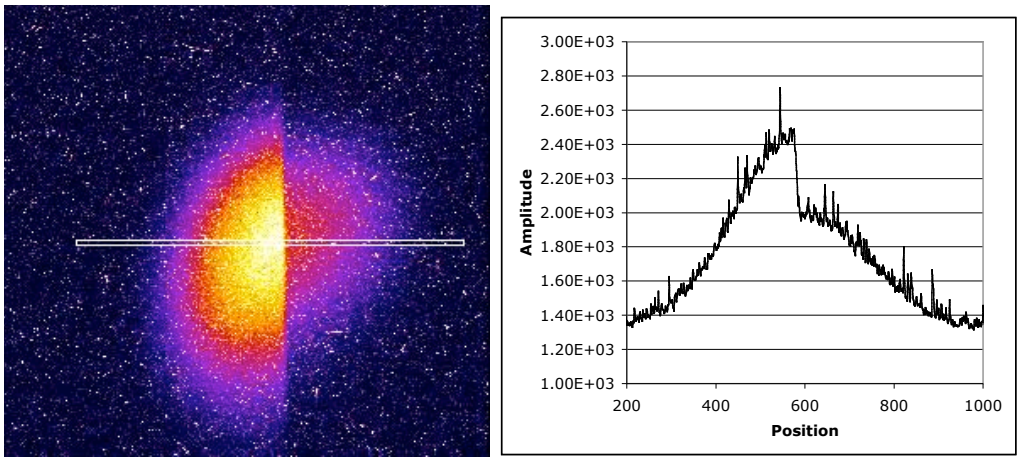

Figure 80 Transmission of x-rays through aluminum foil, and a lineout through the image.

The alternative to varying the material in the filter is to vary the thickness of the filter. The transmission through a material is given by

$$T(\rho, d) = e^{-\mu(\rho)\rho d}$$

where ρ is the density of the material (g/cm^3), $\mu(\rho)$ is the mass attenuation coefficient (cm^2/g), and d is the material thickness. The nonlinear nature of transmission as a function of thickness allows for the extraction of spectral information by comparing the relative attenuation as a function of material thickness.

Aluminum is chosen for the material due to it's ready availability in thin sheets. Images are recorded with the x-ray CCD of the beam transmitted through 1 to 27 Al plates, each of thickness ρ=787 μm. The plates are aligned such that half the beam passes through them, and the other half is unobstructed. This allows us the shot-to-shot variation in total x-ray flux to be compensated. A sample image and lineout is shown in Figure 80. By examining the relative magnitude change at the interface, the amount of attenuation for that thickness of Al can be determined. First, the theoretical spectrum is used in conjunction with the known aluminum transmission function to calculate what transmission is to be expected. Figure 81 shows the predicted and measured transmission; the agreement is good. This implies the spectrum is likely similar to what we expect to get from the theory.

The next step is to try to get a more quantitative measure of the spectrum. The signal transmitted through the Al plates is given by

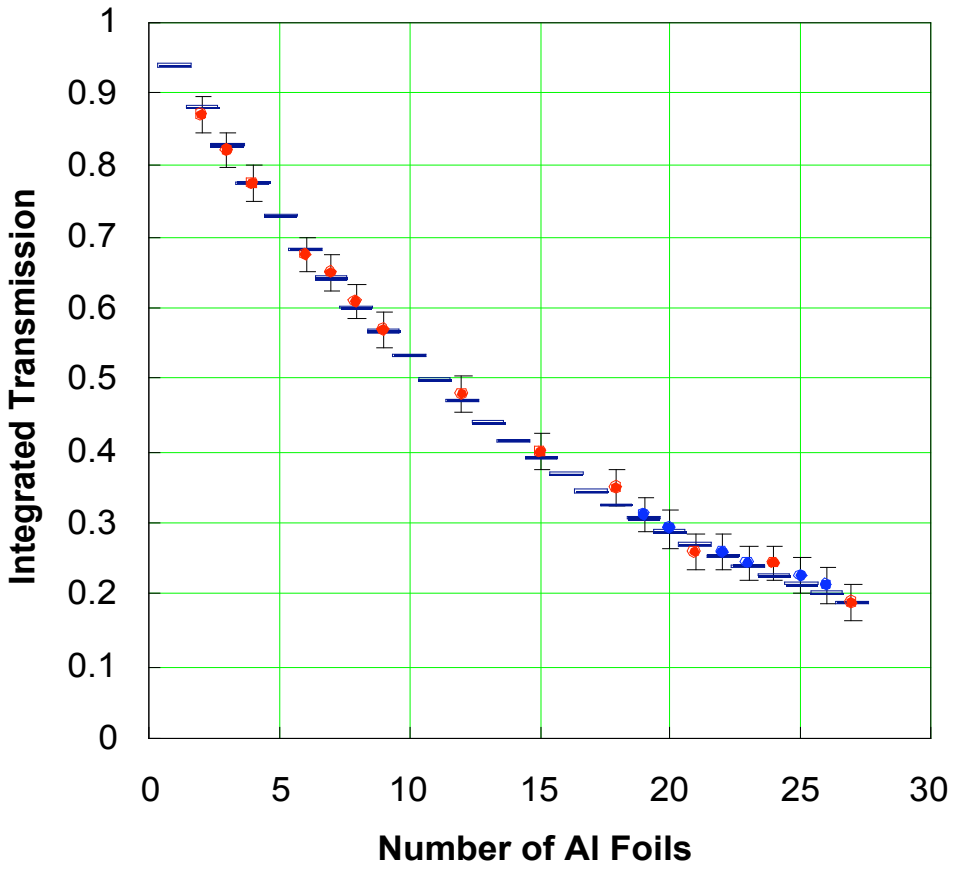

Figure 81 Measured and theoretical transmission of Thomson x-rays through various thicknessed of Al. Each foil is 787 μm thick. The lines are the predicted transmissions based on the theoretical spectrum, the dots are the actual measured transmission.

$$T(d) = \int_0^{\infty} S(E) e^{-d\rho_{Al}\mu_{Al}(E)} dE, \tag{45}$$

where $S(\hbar\omega)$ is the spectrum we are trying to find. We can allow the spectrum to be discretized to make the problem simpler to solve, at the expense of resolution. Therefore, we assume that the spectrum has the form

$$S(E) = \sum_{i=1}^{m} s_i R(E|E_i, \Delta E)$$

$$R(x|x_0, \Delta x) = \begin{cases} 1 & |x - x_0| < \frac{\Delta x}{2} \\ 0 & |x - x_0| > \frac{\Delta x}{2} \end{cases}.$$

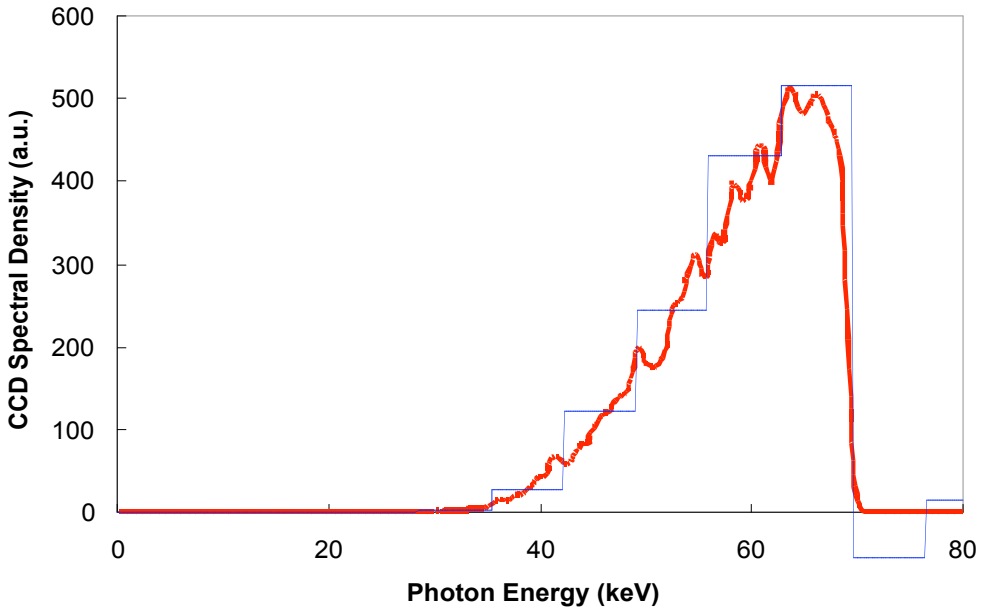

Figure 82 The theoretically predicted spectrum, and the spectrum inferred from the Al transmission measurements. The modulation on the theoretical spectrum is a statistical error due to too few electrons being used in the code.

Assuming the spectrum goes to zero outside the range covered by this sum, and plugging it into (45), gives

$$T_n = T(n\Box) = \sum_{i=1}^{m} s_i \int_{E_i-\frac{\Box E}{2}}^{E_i+\frac{\Box E}{2}} e^{-n\Box\Box_{Al}\Box_{Al}(E)}\,dE$$

or, rewriting it slightly,

$$T_n = \sum_{i=1}^{m} M_{ni} s_i$$

$$M_{ni} = \int_{E_i-\frac{\Box E}{2}}^{E_i+\frac{\Box E}{2}} e^{-n\Box\Box_{Al}\Box_{Al}(E)}\,dE$$

which is a simple linear system of n equations with m unknowns (the s_i); the T_n are measured from the recorded images, and the M_{ni} are calculated from the transmisson of Al given in [108]. The only component remaining undefined is the the E_i and $\Box E$ terms. The assumption that the spectrum goes to zero outside the calculated range puts some limits on the choices; the entire signal must be included. Repeatedly solving the system with different values for the energy bins always produced nearly identical results, or resulted in non-physical solutions (negative s_i's). The

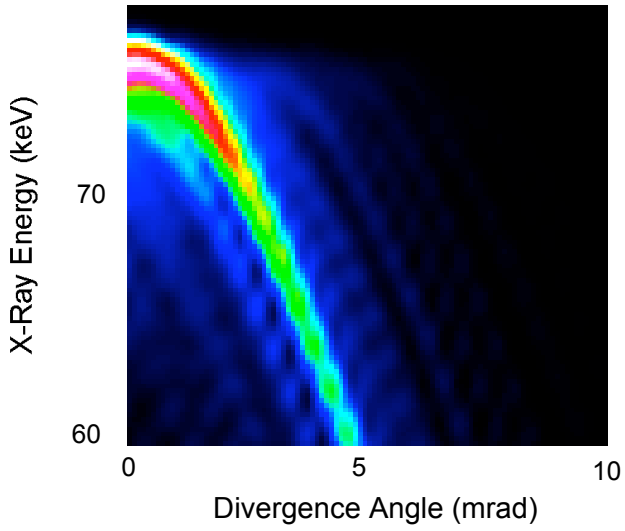

Figure 83 The x-ray spectrum as a function of divergence angle

resultant spectrum, based on 9 data points (and therefore quite coarse), is shown in Figure 82. Also shown is the theoretical spectrum for comparison. The modulation visible on the theoretical beam is a result of statistics in the modeling code: when few electrons are used, the produced spectrum is not smooth, though the general shape matches that generated for a large number of electrons. The evidence suggests that we are indeed generating the expected spectrum. Nonetheless, a more direct measurement would be desirable.

4.2.4 K-edge radiography

As mentioned in the previous section, materials have a sharp drop in transmission at what is known as the K-edge of the material. This is the point at witch the incoming photon has enough energy to eject an inner (K) shell electron. This is observed in the transmission spectrum as a very sharp drop in transmission right at the energy corresponding to the onset of photon absorbtion, then a fairly fast rise to high transmission as the photon continues to increase. There are similar edges, at lower energies, for absorption by electrons in the other shells (L, M, etc.) as well. This property allows for useful measurement techniques such as contrast enhancement by difference imaging. For our purposes, it provides a filter that will demonstrate the spatial

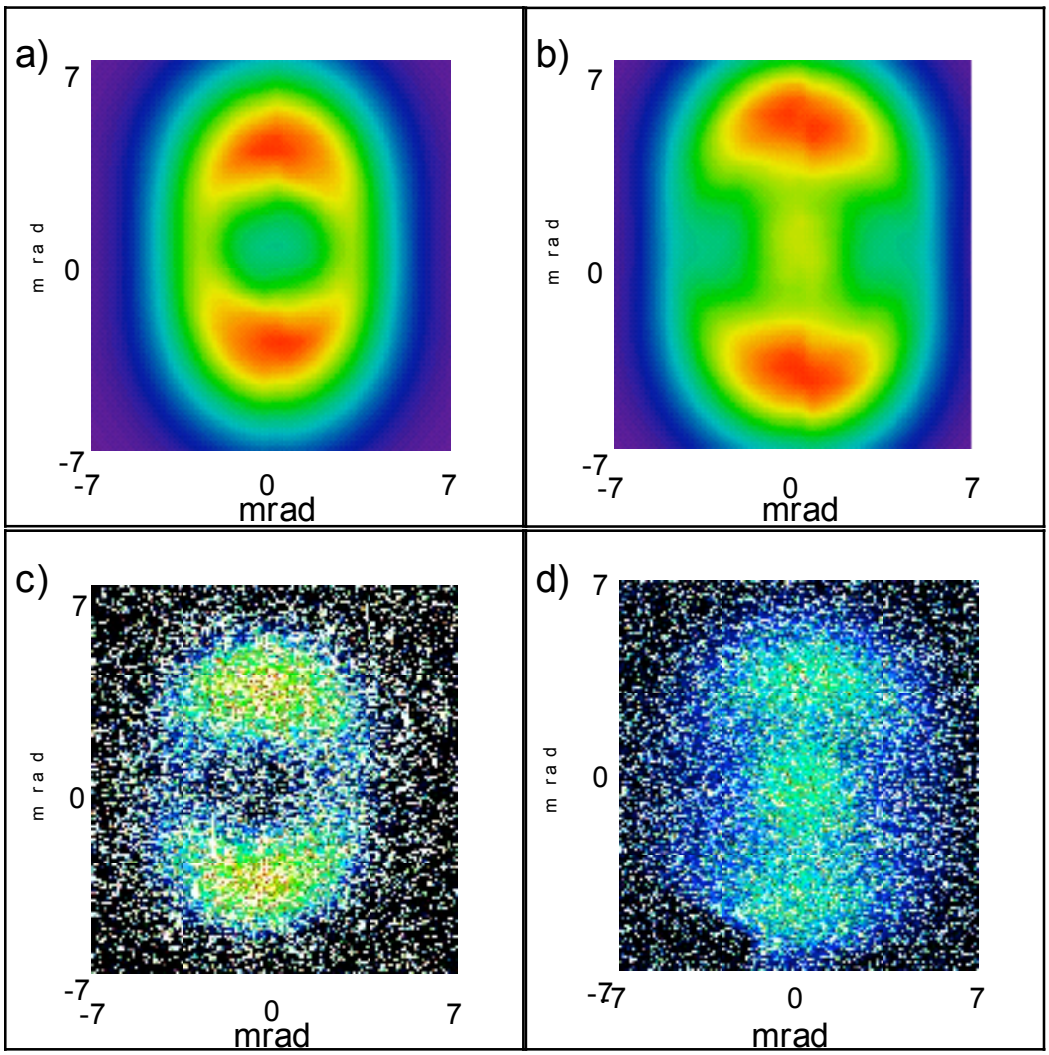

Figure 84 Theoretical and measured transmission through Ta foil. a) theoretical 72.8 keV peak trasnmisson, b) theoretical 78.2 keV peak transmission, c) measured 72.8 keV peak transmission, d) measured 78.2 keV peak transmission

dependence of the spectrum, and provide further evidence for the accuracy of our theoretical code results.

Figure 83 shows the predicted x-ray energy as a function of observation angle, with 0 corresponding to the electron propagation direction. If this beam is made to propagate through a 0.005" Ta foil, which has a transmission function as shown in Figure 79, the photons with energy just above the K-edge at 67.46 keV will be blocked, and given the profile shown in Figure 83, that means the photons in the center will be blocked. If the x-ray beam energy is raised a bit further, the central x-rays will start to transmit through the material more efficiently as their energy

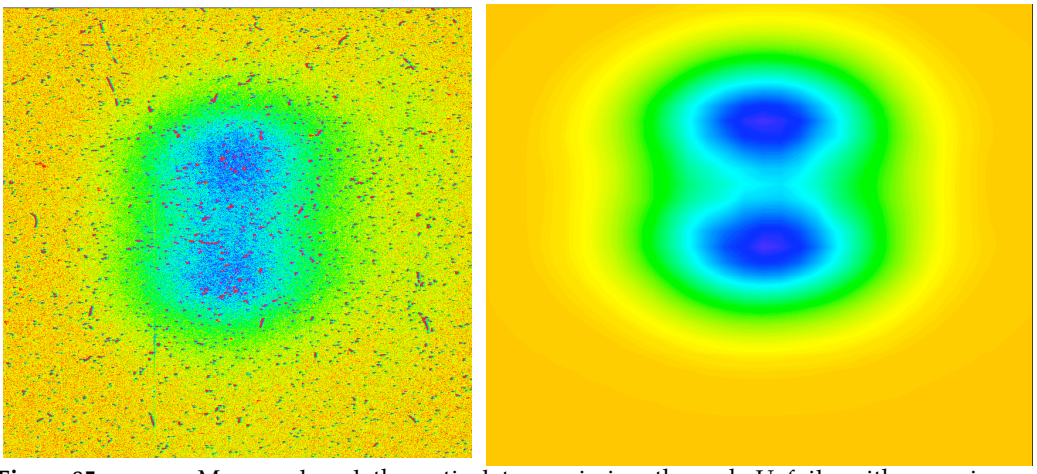

Figure 85 Measured and theoretical transmission through U foils with on-axis peak energy of 122.8 keV.

climbs the steep slope of the transmission curve, leaving a dark ring in the middle of the x-rays spot.

The theoretical and measured transmission at 72.8 and 78.2 keV on-axis peak x-ray energies are shown in Figure 84. The excellent agreement between the measured and theoretical serves as further indication that the code used to simulate the x-ray beam production produces accurate results. A similar test was done with depeted uranium (U) with a K-edge of 115.6 keV, and the results are shown in Figure 85. Again, the agreement is quite good.

4.2.5 Brightness Determination

The question that now remains is the brightness of the source; where does it fall on Figure 1. Because the spectrum seems to match that which is predicted by the theory, we will use the theoretical spectrum for the calculation. A single-shot image records 480 counts in the central 6 x 6 pixel cell. The total energy detected per unit solid angle is then

$$E_{meas} = \frac{N_{CCD}}{\Omega_{CCD}\left(\frac{x}{z}\right)^2}$$

Meanwhile, we have a theoretical value for the number of photons emitted per unit frequency per unit solid angle, $\frac{d^2N}{d\Omega d\omega}$, from the code of [53]. We can then find the total energy that would be expected at the CCD,

$$E_{theo} = \int_0^{\infty} \frac{d^2N}{d\Omega d\lambda} \hbar\omega T_{BK7}(\omega) \eta_{CsI}(\omega) d\omega .$$

This provides the magnitude scaling of the predicted spectrum. We can then use the theoretical spectrum to get the bandwidth portion of the brightness:

$$\frac{E_{meas}}{E_{theo}} \frac{d^2N}{d\Omega d\lambda}\left(10^{-3}\lambda\right) = 24.4 \frac{\text{photons}}{\text{mrad}^2 \cdot 0.1\%\text{BW}}.$$

The next component of the brightness is the source size. This can be approximated from the known laser and electron spot sizes. The overlap integral gives

$$\Delta A = \int_0^{\infty} e^{-\frac{2r^2}{w_0^2}} e^{-\frac{r^2}{2\sigma^2}} 2\pi r dr = 1.19 \cdot 10^{-3}\ \text{mm}^2.$$

Similarly, the temporal durationis given by the electron beam length, and so

$$\Delta t = \int_0^{\infty} e^{-\frac{t^2}{2\sigma^2}} dt = 7.52\ \text{ps}.$$

Putting these all together gives

$$\frac{1}{\Delta A}\frac{1}{\Delta t}\frac{E_{meas}}{E_{theo}} \frac{d^2N}{d\Omega d\lambda}\left(10^{-3}\lambda\right) = 2.75 \cdot 10^{15} \frac{\text{photons}}{\text{s} \cdot \text{mm}^2 \cdot \text{mrad}^2 \cdot 0.1\%\text{BW}}.$$

Chapter 5. Looking Forward

To date, a successful Thomson scattering source has been demonstrated, and the theoretical model of the x-rays expected from a Thomson source has been verified. The obvious next question is "What now?", to which there are two sets of answers. The first set relates to the PLEIADES facility itself, and how it can both be improved (better x-ray quality, more sensitive diagnostics, higher energy production, etc.) and used (how an experiment can be done). The second set relates to Thomson sources in general: how they can be designed to reached unique diagnostic regimes that are difficult to achieve with other x-ray sources discussed in Section 1.1.1, and what schemes might be used to improve or simplify the interaction process.

5.1 Upgrades

First, regarding the PLEIADES facility itself, there are several improvements and changes that can be made to improve the x-ray beam quality and utility. The first of these, which has already been implemented, is the replacement of the enhanced quadrupole magnets discussed in Section 4.1.2 with new permanent magnet-based quadrupoles (PMQs). The biggest advantage PMQs would offer a Thomson source is the much larger magnetic field gradient they can produce, which translates into a much stronger focus of the electron beam. For our system, the focusing strength goes from 15 T/m to 500 T/m when the enhanced quadrupoles are replaced by PMQs, producing a smaller x-ray source spot. With this smaller spot, the total x-ray flux is also expected to improve, since more of the electrons see the greater photon density at the center of the laser focus instead of passing by in the wings of the laser beam. Despite the higher flux and smaller spot size, both of which imply an improved brightness, it is unclear whether the total brightness would in fact go up; the trade-off in reducing the spot size by focusing the electron beam harder is an increased angular spread in the electrons at the focus; the emittance of the beam remains unchanged. This larger electron divergence translates to larger x-ray divergence, and therefore lower brightness.

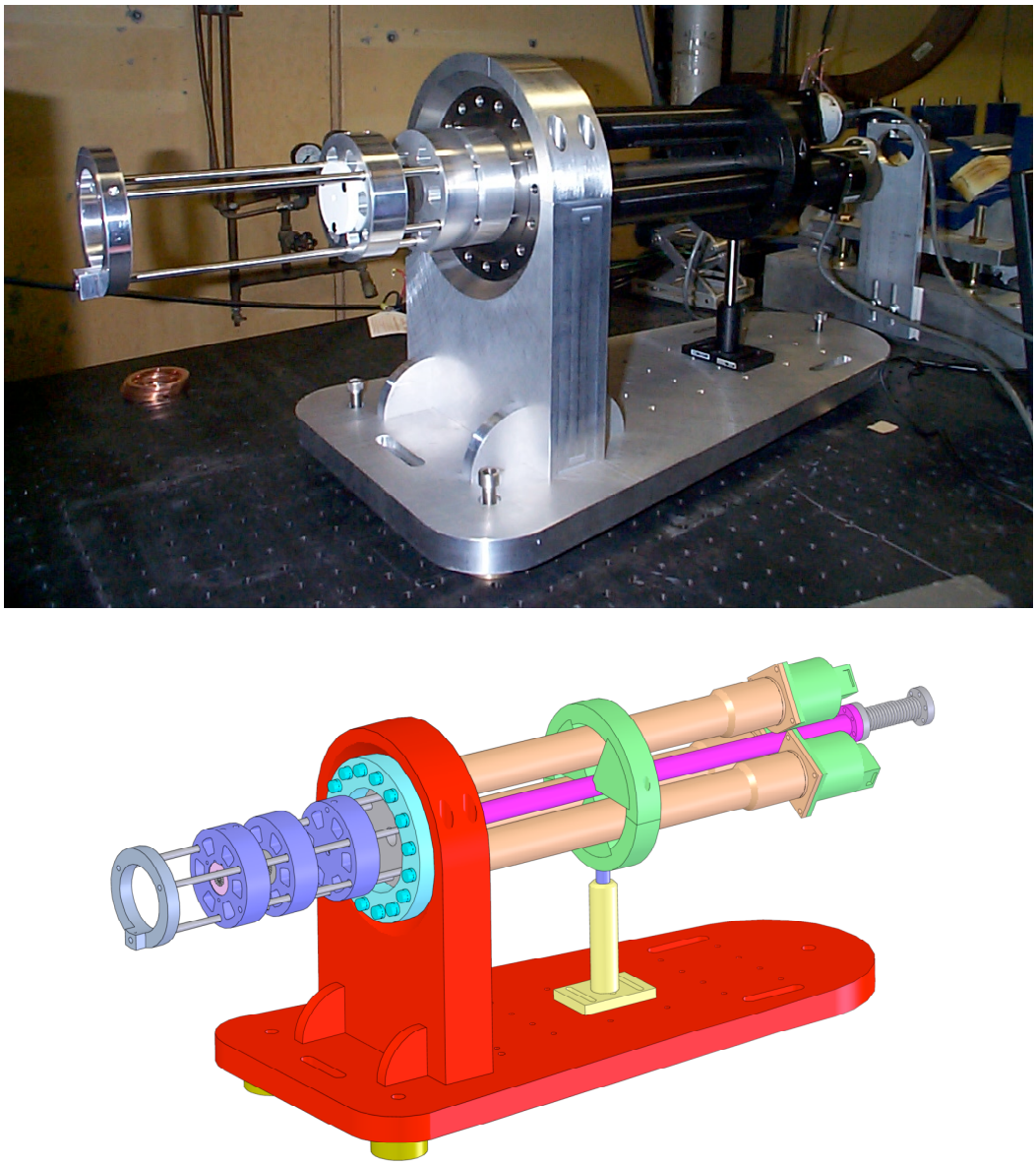

Figure 86 Photo and CAD model showing the permanent magnet quadrupoles, including the hardware necessary to adjust the magnet spacing, the only free parameter with these quads.

There are a few practical downsides to the switch to PMQs; first, because the magnets are, by definition, permanent, the focusing control usually provided by adjusting the current in the quadrupole magnets (and consequently the magnetic field strength) is lost. This leaves the spacing between the magnets as the only adjustment available to change the focusing properties of the system. A second difficulty with this system is that, because the electrons are focused so much harder, the focal point moves much closer to the quadrupole. Fortunately, in the 180°

geometry being used in PLEAIDES, this doesn't prove to be too significant of an issue because the laser beam still goes straight down the beam pipe; however, it does limit the lower energy of the system to ~50 MeV electrons – lower energies focus inside the PMQ assembly, making them impossible to diagnose: the alignment cube from Section 4.1.3 can't be placed at the focus. Yet another complication results from the need to collect and dispose of the electron beam after the focus: because the beam is expanding much faster from the tighter focus, getting the whole beam through the dipole spectrometer and into the beam dump without losing much energy to the walls (which would create x-rays and therefore noise in the detection system) is much harder. Finally, because the PMQs can't be turned off or easily adjusted, beam parameters such as the energy, energy spread, and emittance must now be measured upstream of the interaction region. Although it is not expected the parameters would change by going through the quads, at present we have no way to determine this conclusively. A PMQ set-up has been designed and implemented by collaborators at UCLA to be used on the PLEAIDES system (see Figure 86), and it has produced spot sizes <20 μm. Attempts are being made to quantify the increased levels of noise in this setup.

The next upgrade is a replacement of the x-ray CCD camera currently being used for all the measurements. The current fiber-coupled camera system, described in Section 4.2.1, has a very high electronic noise background. Furthermore, attempts to integrate the x-ray signal for long periods of time tend to increase the noise significantly. This is mostly due to the fact that, while the x-rays of interest are only present for a few tens of picoseconds every second, the background is around for microseconds (e.g. from dark current in the accelerator), or continuously (from activated components in the cave). In an attempt to solve this problem, a Princeton Instruments PI-MAX-512 CCD system was borrowed and tested. This system uses a gated image intensifier, with a rise time on the order of nanoseconds. The x-ray beam has been observed using this camera with signal-to-noise ratios greater than 10:1 (as compared with the sometimes 1.5:1 of the PI-SCX camera originally used, see Figure 87 for a comparison). Additionally, because of the gating, long integrations can be performed without significantly increasing the background. The downside of this camera is that it is not fiber-coupled. This means the CsI scintillator must be imaged with a lens onto the intensifier cathode, which

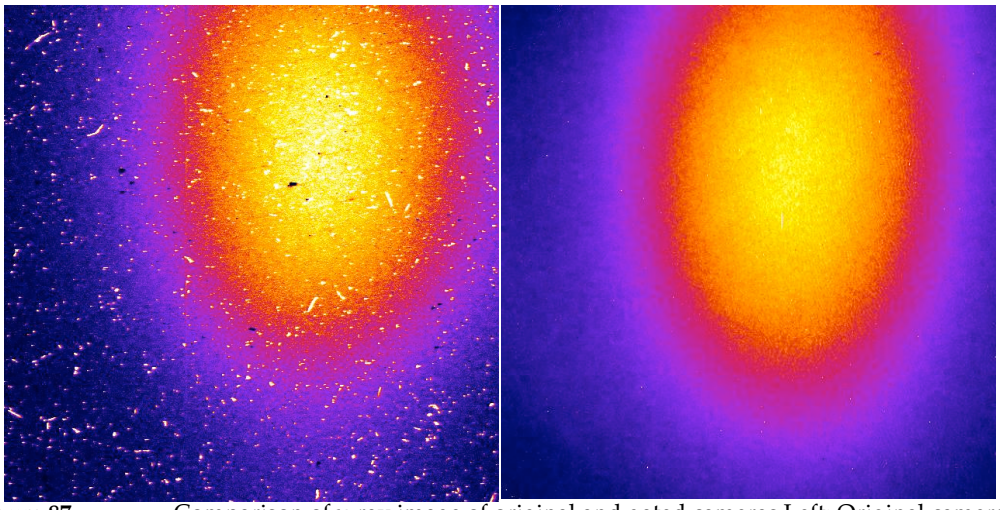

Figure 87 Comparison of x-ray image of original and gated cameras Left: Original camera Right: Gated Camera.

significantly reduces the light capture of the camera (<1% of the total light produced is collected). Based on the positive results with this camera, a new camera has been ordered that is both gated and fiber coupled, which should make experimental measurement much more accurate, and require fewer x-ray photons to perform them.

To increase the available x-ray flux, the final turning mirror, discussed in Section 4.1.2, will be replaced by a mirror with two holes drilled through the center, as shown in Figure 88. A 5-mm aperture is used for the holes, which will allow the central 5 mrad x-ray cone to pass through without the absorption 0.5" of BK7 glass would cause, which at 70 keV attenuates the signal by 40% and effectively blocks x-rays below 40 keV. The second hole is to allow the portion of the laser beam which would normally be reflected where the x-ray aperture is located to pass through the optic without depositing energy and ablating the glass on the side of the hole. Conveniently, this escaping beam can make a useful ultrafast pump for experiments, because it is well synchronized with the x-rays; such an experiment is discussed in Section 5.2.

Two other changes to the linac system (aside from the installation of the PMQs) are also being planned. The first is the use of a magnesium cathode instead of the current copper cathode. A small (< 2 mm diameter) magnesium plug would be embedded in a standard copper cathode and placed in the gun. The quantum efficiency for magnesium is over ten[110] times larger than for copper, so this would allow production of the same beam current with one tenth of the uv pulse energy. This means that energy could be sacrificed to produce more uniform spatial profile

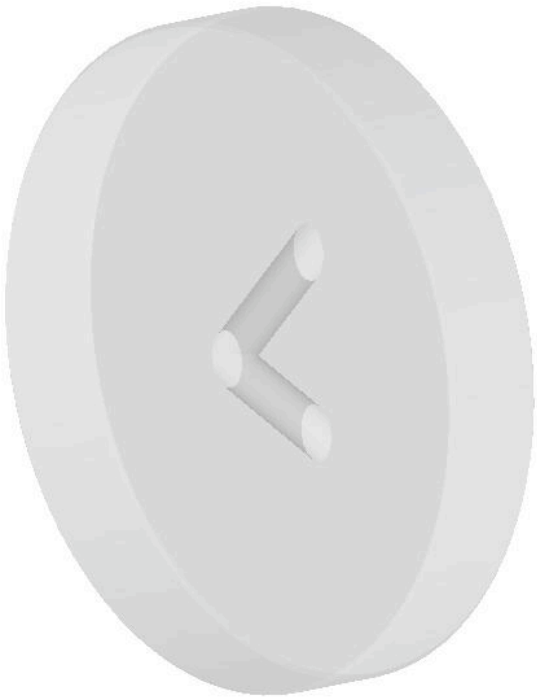

Figure 88 Replacement final turning mirror, with two holes drilled to allow the central part of the x-ray and laser beams to pass through it.

(compared to the highly irregular profile shown in Figure 39), or in producing a flat temporal pulse, either of which in turn could yield an improved electron beam and higher x-ray brightness. Alternatively, the uv system could be kept the same and a larger current could be produced, directly increasing the x-ray flux by increasing the number of scattering electrons.

The final change to the acceleration system, which has been tested already, is to temporally compress the electron beam. Because the x-ray duration in the 180° interaction geometry of PLEIADES is directly related to the electron bunch length, a short electron bunch would translate into a shorter x-ray pulse, with a higher corresponding peak brightness. The process is illustrated in Figure 89. Standard electron acceleration is performed with the electron bunch riding the crest of the rf field; the field is fairly constant over the length of the bunch, and provides a uniform accelerating gradient to the whole bunch. In the velocity compression scheme, the beam is injected into an accelerating section, not at the peak of the rf field, but at the zero crossing. Here, the latter part of the bunch experiences a positive accelerating gradient, and

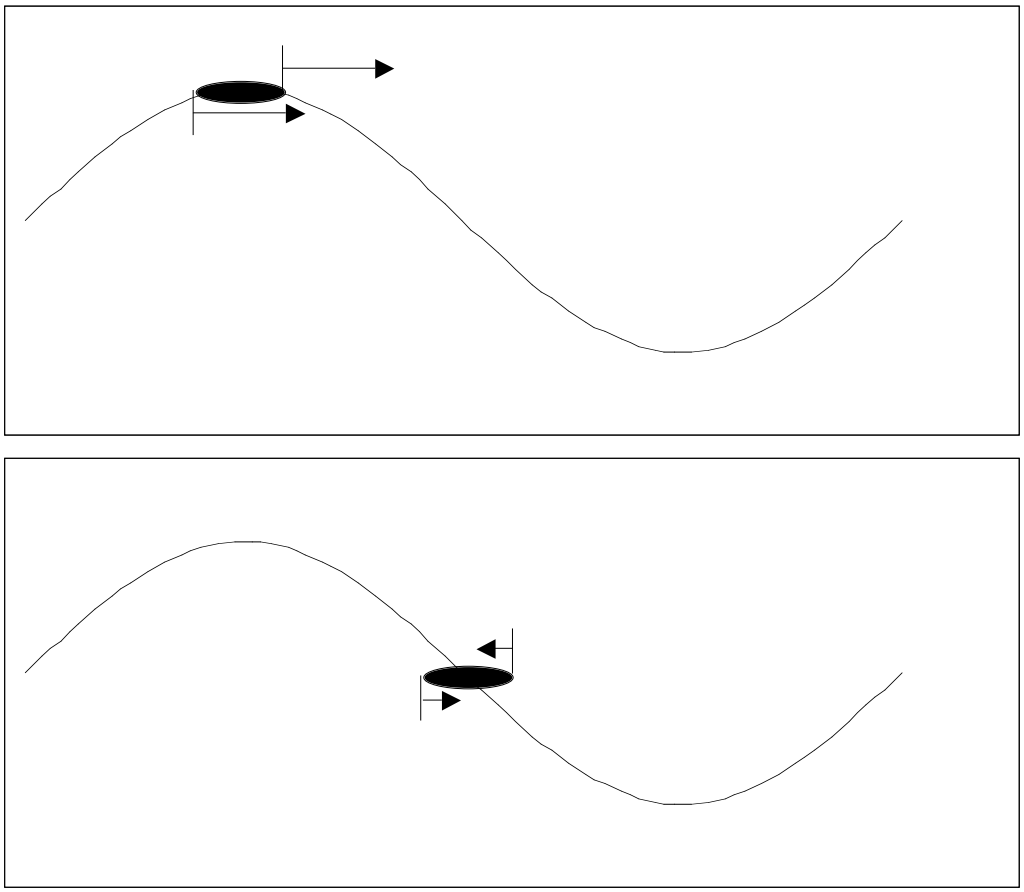

Figure 89 Velocity compression. The upper figure show standard acceleration: the electron bunch rides on the crest of the rf field, and the whole beam sees nearly uniform accelerating gradient. The lower figure shows the compression scheme: riding the zero crossing of the phase, the back of the electron bunch is accelerated and the front is decelerated, making the bunch shrink in length.

starts to catch up to the earlier electrons. Conversely, the electrons at the front of the beam experience a negative accelerating gradient and are slowed so as to drop back toward the center of the bunch. Thus, the bunch length is reduced. Bunch durations less than 300 fs have been demonstrated with the PLEIADES accelerator using this scheme[111], which implies the x-rays produced are similarly ~300 fs in duration.

5.2 Experimental work

There are two experiments currently planned using the PLEIADES source: one that will further test Thomson scattering theory, and one that will demonstrate the material study capabilities of the system. The first experiment will be a study of dynamic diffraction of gold. An

ultrashort laser pulse impinging upon the gold crystal will excite phonon modes in the crystal, which means that the lattice spacing will become a function of time; it is this temporal dependence that would be studied. With a collimated, monochromatic beam, this is a fairly straightforward task: with the crystal aligned such that the Bragg condition,

$$2d\sin\theta = n\lambda$$

(where d is the lattice spacing, θ is the incidence angle, and λ is the x-ray wavelength), is met, the diffracted signal is monitored. As the spacing varies from d, the signal will drop, giving an indication of the lattice spacing as a function of time.

Unfortunately, Thomson sources are neither monochromatic nor collimated. With the same setup and a polychromatic beam, as d varies, instead of the signal dropping, a different x-ray energy is reflected. With a non-collimated beam, there are different energies, impinging at different angles, which get diffracted by the crystal; a change in the lattice spacing then changes where which energies are going. All this makes the diffracted signal more difficult to sort out, and the change induced becomes a small perturbation to the overall signal being diffracted. This is then compounded by the fact that, unless the entire thickness of the crystal is deformed by the laser pulse, there will still be a strong component of the diffracted signal that results from diffraction from the unperturbed portion of the crystal. The expected change in the diffracted signal with a non-collimated, polychromatic source is then very small. There is, however, a solution.

This experiment will be very similar to one done at Lawrence Berkeley National Laboratory (LBL) using indium antimonide (InSb)[112]. There, they overcame these problems in two ways. First, the x-rays were collimated with small apertures, which also cut the flux down to approximately one photon every ten shots. Then, the spectrum and flux of the diffracted beam was monitored. As the lattice spacing increased, lower energy x-rays were diffracted from the crystal. This was observed as a broadening of the spectrum, and as a shift of the center of the spectrum. The measured shift was approximately 0.1% (from 29.72 keV to 29.68 keV, see Reference 112, Figure 2). However, the detector they used had a claimed resolution of only 1%, so although the numbers agree with the theoretical predictions, they are not fully convincing. Additionally, $>10^4$ shots had to be integrated over to obtain the spectrum at each delay point.

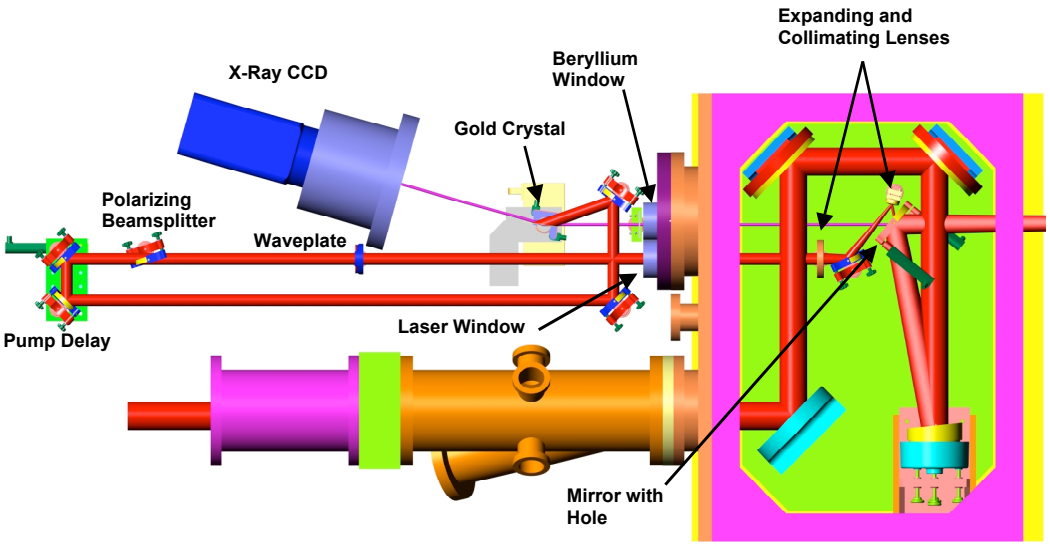

Figure 90 Experimental set-up for the initial dynamic diffraction experiment.

There is a method, however, which could provide a more robust experimental result, and allow it to be done without as many shots, because a single-photon-counting detector is not necessary; this is the method proposed for the first PLEIADES experiment.

The setup for this experiment is show in Figure 90. The FALCON laser follows the same path as discussed in Section 4.1.2. The final turning mirror in this case however has two holes drilled in it, as shown in Figure 88, to allow parts of the laser and x-ray beams to pass through it. Running at full power, with 540 mJ of ir light reaching the interaction region, approximately 25 mJ of light is expected to pass through the 5 mm hole in the mirror. The portion of the laser that passes through the mirror will then be up-collimated with a pair of lenses, and sent through a window out of the vacuum chamber. A waveplate and polarizer will be used to adjust the laser energy getting to the crystal. A delay stage will be used to adjust the timing of the laser arrival relative to the x-rays. The x-rays will propagate through the final turning mirror and leave the vacuum via a 300 μm beryllium window. They will diffract of the gold sample and be detected by the x-ray CCD camera.

The solution to the problems of a polychromatic, uncollimated source is the use of a K-edge filter to create a sharp edge in the spectrum. Figure 91 illustrates how this affects the diffraction. The upper left side of the figure shows the diffraction spot expected at the angle θ_b, given by

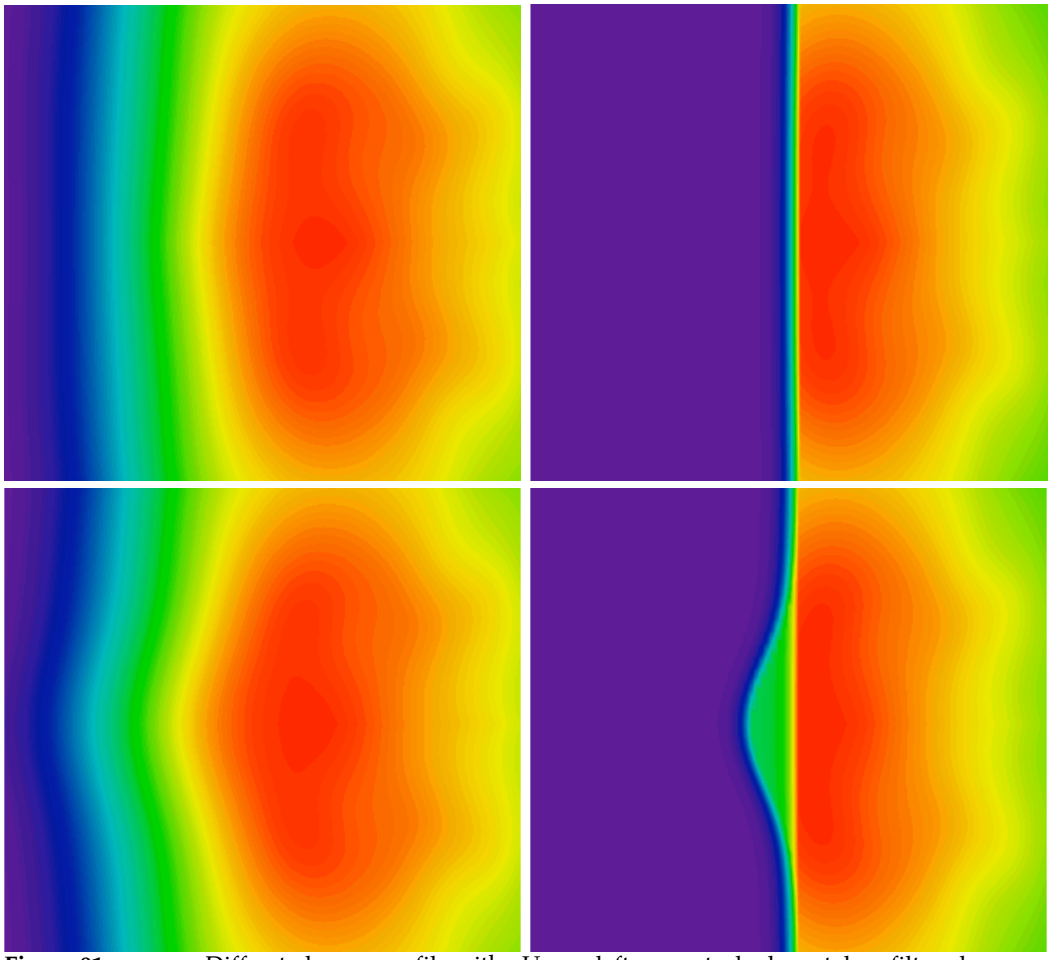

Figure 91 Diffracted x-ray profile with - Upper left: unperturbed crystal, unfiltered x-rays, Upper right: unperturbed crystal, filtered x-rays, Lower left: perturbed crystal, unfiltered x-rays, Lower right: perturbed crystal, filtered x-rays.

$$2d_0 \sin\theta_0 = \lambda_k,$$

where d_0 is the unperturbed lattice spacing and λ_k is the wavelength of the K-edge of the filter material. The spot is large, and a small change in the lattice spacing will essentially cause this shape to shift to the right or left somewhat, as the angle matching the Bragg condition changes. Once the filter is inserted, however, there are no longer any x-rays at shorter wavelengths than λ_k. Therefore, photons incident upon the surface at an angle $\theta_0+\Delta\theta$, which would require $\lambda > \lambda_k$, would still diffract, and show up at $\theta_0+\Delta\theta$, while photons incident at an angle $\theta_0-\Delta\theta$, which would show up then at $\theta_0-\Delta\theta$, would have been absorbed by the filter because of the requirement that $\lambda < \lambda_k$. This leaves the profile shown on the upper-right portion of Figure 91, with a dark, "background-free" region with no detected x-rays.

When the lattice is then deformed, the shape of this edge will change. For $d > d_0$, the diffraction angle $\theta < \theta_0$ will cause x-rays at the K-edge to move left, into the dark region, where they would be easily visible. Conversely, for $d < d_0$, the diffraction angle $\theta > \theta_0$ will cause the dark boundary to move to the right. The lower portion of Figure 91 illustrates the former case. The lower-right side shows the observed diffraction pattern when the center of the crystal is perturbed (the upper and lower edges are unperturbed). The x-rays near the K-edge where the lattice spacing has increased now appear in the dark region. Note that, because the region is dark, there is no background from the undistorted portion of the crystal to interfere with the measurement. The lower-left side of the image shows the result without the K-edge filter. Here, the small perturbation must be seen against the background of the higher-energy x-rays diffracting off the unperturbed portion of the crystal. Comparing the two left images with the two right images illustrates the advantage of the filtering technique. This should provide a more robust measurement of the changing diffraction pattern as the gold lattice spacing changes than the LBL experiment offered.

The second experiment planned is a further test of the theory of Thomson scattering by going into the non-linear scattering regime. This is done by replacing the 60" focal length parabola with a 12" focal length parabola. This much tighter focus should allow a focused beam size of approximately 6 μm, which would push the normalized vector potential a_0 above 1. The setup for this experiment is shown in Figure 92. The effect discussed in Section 1.2.3, depression of the peak x-ray energy, is expected to be observed; the easiest way to detect this is to repeat the K-edge transmission measurements of Section 0. If the x-rays are tuned above the K-edge, so that the hole is seen as in Figure 84, with $a_0 < 1$ (accomplished by not fully compressing the laser pulse), then a_0 can be turned up, and the x-ray peak energy will drop, causing the hole to fill in. Naturally, a direct spectral measurement would be ideal, but this is a good alternative until a suitable method to record the spectrum is found.

5.3 Scalability

Having successfully demonstrated a Thomson source, and verified the accuracy of the Thomson codes that have been created, it is now possible to look at the future possibilities for a

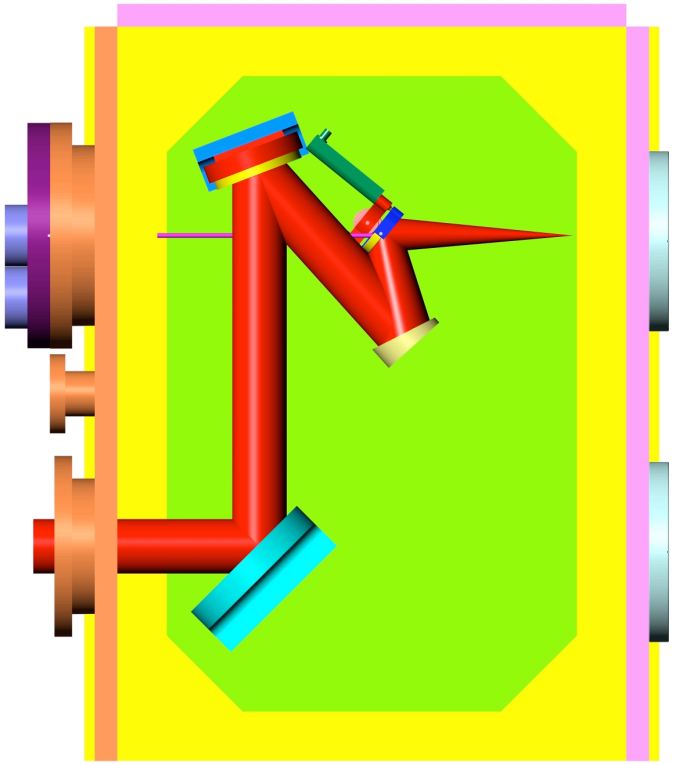

Figure 92 Laser setup for the nonlinear Thomson scattering experiment.

sources such as PLEIADES. There are two areas for improvement. Once is in the brightness of the source, the other is in the peak energy of the system. Hartemann[113] has come up with a scheme to improve the brightness by increasing the photon flux incident on the electron bunch that avoids the pitfalls of nonlinear scattering by using them to the advantage of the system.

Recall there are two effects in non-linear scattering: the depression of the peak energy, and the introduction of harmonics. Preliminary nonlinear theory work (which is hoped to be partially verified with the nonlinear experiment discussed in the previous section) has shown that the various harmonics produced can be suppressed by using circularly polarized light (to eliminate the high orders), and by making the laser pulse square temporally (to eliminate transient harmonics which come from the ramping up and down of the electron oscillation as it enters and exits the laser focus). So with a properly shaped pulse, the laser intensity can be turned up well past a_0=1, with the electron energy boosted accordingly to maintain the x-ray energy, to get much higher brightnesses than linear systems can produce.

Although capable of creating very short x-rays pulses, the simple scaling to higher energies is a potentially much more attractive feature of Thomson sources. As was shown in Figure 1, x-ray flux drops off rapidly at high energies for current synchrotron sources. 1 MeV energies are well beyond the range of modern synchrotrons: either the ring energy would have to be dramatically increased, or undulator periods would have to be significant decreased.

However, a 1 MeV Thomson source is quite easy to envision. Currently, the PLEIADES facility is running with four of five available SLAC sections, each capable of producing between 20 and 30 MeV of acceleration. If the fifth section is added to the system, an electron beam energy of 120 MeV should be easily achieved. Currently, the FALCON laser produces 810 nm light to scatter. If that light is frequency-tripled to 270 nm, (5) tells us that the peak photon energy will be 1021 keV. This would be a 1 MeV short-pulse x-ray source, with well established technology. Energies at that level would be excellent for many radiography measurements. The transmission of materials as a function of x-ray energy in general increases as energy increases, until around the 5 MeV level, at which point it begins to rise again. This is because once the x-ray energies get above 1.022 MeV, there is enough energy for pair creation. By passing these high-energy x-rays through a dense material, a very bright positron source can be produced, with very small positron bunch lengths.

It is clear that there are several potential developmental paths a Thomson scattering source can take from this point. Which one will depend on the desired application and therefore most important feature: shorter pulse, higher energy, or higher brightness. A Thomson source proves to be a useful alternative to other technologies in several regimes.

References

[1] *CRC Handbook of Chemisty and Physics*, 51st edition, R. C. Weast, ed.(Chemical Rubber Company, Cleveland, OH, 1970), p. E-198.

[2] C. V. Shank, R. Yen, C. Hirlimann, Phys. Rev. Lett. **51**, 900 (1983).

[3] B. L. Holian, P. S. Lomdahl, Science, **280**, 2085 (1998).

[4] W. G. Wagner, B. A. Lengyel, J. Appl. Phys., **34**, 2040 (1963).

[5] H. W. Mocker, R. J. Collins, Appl. Phys. Lett. **7**, 270 (1965).

[6] R. Ell, U. Morgner, F. X. Kärtner, *et al.*, Opt. Lett., **26**, 373 (2001).

[7] M.C. Downer, R. L. Fork, C. V. Shank, J. Opt. Soc. Am. B **2**, 595 (1985).

[8] C. V. Shank, R. Yen, C. Hirlimann, Phys. Rev. Lett. **50**, 454 (1983).

[9] C. V. Shank, R. L. Fork, R. F. Leheny, J. Shah, Phys. Rev. Lett. **42**, 112 (1979).

[10] N. F. Scherer, J. L. Knee, D. D. Smith, A. H. Zewail, J. Phys. Chem. **89**, 5141 (1985).

[11] S. DeSilvestri, J. G. Fujimoto, E. P. Ippen, *et al.*, Chem. Phys. Lett. **116**, 146 (1985).

[12] K.-J. Kim, in *Physics of Particle Accelerators*, edited by M. Month, M. Dienes (AIP Conf. Proc. 184, 1989), 565.

[13] M. Saes, C. Bressler, R. Abela, *et al.*, Phys. Rev. Lett., **90**, 047403 (2003).

[14] J. Larsson, P. A. Heimann, A. M. Lindenberg, *et al.*, Appl. Phys. A, **66**, 587 (1998).

[15] D. A. Reis, M. F. DeCamp, P. H. Bucksbaum, Phys. Rev. Lett., **86**, 3072 (2001).

[16] J. Larsson, Meas. Sci. Tech., **12**, 1835 (2001).

[17] A. A. Zholents and M. S. Zolotorev, Phys. Rev. Lett. **76**, 912 (1996).

[18] R. W. Schoenlein, S. Chattopadhyay, H. H. W. Chong *et al.*, Science **287**, 2237 (2000).

[19] D. Attwood, Supplemental Material to Ref. 55, available at http://www.coe.berkeley.edu/AST/sxreuv/2004/Ch05.pdf.

[20] T. Guo, Ch. Spielmann, B. C. Walker, C. P. J. Barty, Rev. Sci. Inst. **72**, 41 (2001).

[21] C. Rischel, A. Rousse, I. Uschmann, *et al.*, Nature, **390**, 490 (1997).

[22] A. Rousse, C. Rischel, S. Fourmaux, *et al.*, Nature, **410**, 65 (2001).

[23] C. W. Siders, A. Cavalleri, K. Sokolowski-Tinten, *et al.*, Science, **286**, 1340 (1999).

[24] A. Cavalleri, C. W. Siders, C. Rose-Petruck, *et al.*, Phys. Rev. B, **63**, 193306 (2001).

[25] A. Cavalleri, C. W. Siders, F. L. H. Brown, *et al.*, Phys. Rev. Lett.., **85**, 586 (2000).

[26] K. Sokolowski-Tinten, C. Blome, C. Dietrich, Phys. Rev. Lett., **87**, 225701 (2001).

[27] A. Cavalleri, Cs. Tóth, C. W. Siders, J. A. Squier, Phys. Rev. Lett., **87**, 237401 (2001).

[28] K. Kinoshita, H. Harano, K. Yoshii, *et al.*, Lasers Part. Beams., **19**, 125 (2001).

[29] A. Rousse, C. Rischel, S. Fourmaux, *et al.*, Meas. Sci. Tech., **12**, 1841 (2001).

[30] A. Cavalleri, Ch. Blome, P. Forget, *et al.*, Phase Trans., **75**, 769 (2002).

[31] J. Arthur, G. Materlik, R. Tatchyn, H. Winick, Rev. Sci. Inst. **66**, 1987 (1995).

[32] E. Feenberg and H. Primakoff, Phys. Rev. **73**, 449 (1948).

[33] R. H. Milburn, Phys. Rev. Lett. **10**, 75 (1963).

[34] F. R. Arutyunian, V. A. Tumanian, Phys. Lett. **4**, 176 (1963).

[35] G. Fiocco, E. Thompson, Phys. Rev. Lett. **10**, 89 (1963).

[36] C. Bemporad, R. H. Milburn, N. Tanaka, M. Fotino, Phys. Rev. **138**, B1546 (1965).

[37] P. Sprangle, A. Ting, E. Esarey, A. Fisher, J. Appl. Phys. **72**, 5032 (1992).

[38] I. V. Pogorelsky, Nuc. Inst. Meth. Phys. Res. A, **411**, 172 (1998).

[39] K. J. Kim, S. Chattopadhyay, C. V. Shank, Nuc. Inst. Meth. Phys. Res. A **341**, 351 (1994).

[40] R. W. Schoenlein, W. P. Leemans, A. H. Chin *et al.*, Science **274**, 236 (1996).

[41] P. Panek, J. Z. Kaminski, F. Ehlotzky, Opt. Commun, **213**, 121 (2002).

[42] P. Panek, J. Z. Kaminski, F. Ehlotzky, Eur. Phys. J. D, **26**, 3 (2003).

[43] J. Yang, M. Washio, A. Endo, T. Hori, Nuc. Inst. Meth. Phys. Res. A, **428**, 556 (1999).

[44] X. Zheng, C. Ruan, R. Shang, J. Deng, Rev. Sci. Inst. **69**, 4044 (1998).

[45] K. Lee, Y. H. Cha, M. S. Shin, *et al.*, Opt. Exp., **11** 309 (2003).

[46] E. Esarey, S. K. Ride, P. Sprangle, Phys. Rev. E, **48**, 3003 (1993).

[47] S. K. Ride, E. Esarey, M. Baine, Phys. Rev. E, **52**, 5425 (1995).

[48] Y. Y. Lau, F. He, D. P. Umstadter, R. Kowalczyk, Phys. Plasmas, **10**, 2155 (2003).

[49] F. He, Y. Y. Lau, D. P. Umstader, T. Strickler, Phys. Plasmas, **9**, 4324 (2002).

[50] F. V. Hartemann, A. L. Troha, N. C. Luhmann, Jr., Phys. Rev. E, **54**, 2956 (1996).

[51] F. V. Hartemann, H. A. Baldis, A. K. Kerman, *et al.*, Phys. Rev. E **64**, 016501 (2001).

[52] F. V. Hartemann, *High Field Electrodynamics* (CRC Press, Boca Raton, FL, 2002).

[53] W. J. Brown, F. V. Hartemann, Phys. Rev. Spec. Top.-Accel. and Beams, **7**, 060703.

[54] J. D. Jackson, *Classical Electrodynamics*, 3rd Edition (John Wiley & Sons, Inc., New York, NY, 1999).

[55] D. Attwood, *Soft X-Rays and Extreme Ultraviolet Radiation*, 1st Edition (Cambridge University Press, Cambridge, UK, 1999).

[56] F. V. Hartemann, Phys. Rev. E **61**, 972 (2000).

[57] R. Haberman, *Elementary Applied Partial Differential Equations*, 2nd Edition (Prentice Hall, Englewood Cliffs, NJ, 1983).

[58] F. Glotin, J.-M. Ortega, R. Prazeres, *et al.*, Phys Rev Lett, **77**, 3130 (1996).

[59] I. Sakai, T. Aoki, K. Dobashi, *et al.*, Phys. Rev. Spec. Top.-Accel. and Beams, **6**, 091001 (2003).

[60] H. Kotaki, M. Kando, H. Dewa, *et al.*, Nuc. Inst. Meth. Phys. Res. A, **455**, 166 (2000).

[61] K. Chouffani, D. Wells, F. Harmon, *et al.*, Nuc. Inst. Meth. Phys. Res. A, **495**, 95 (2002).

[62] S. Kashiwagi, M. Washio, T. Kobuki, *et al.*, Nuc. Inst. Meth. Phys. Res. A **455**, 36 (2000).

[63] A. Ting, R. Fischer, A. Fisher, *et al.*, J. Appl. Phys., **78**, 575 (1995).

[64] M.Yorozu, J. Yang, Y. Okada, *et al.*, Jap. J. Appl. Phys., **40**, 4228 (2001).

[65] F. E. Carroll, Am. J. Rad. **179**, 153 (2002).

[66] A. D'Angelo, O. Bartalini, V. Bellini, *et al.*, Nuc. Inst. Meth. Phys. Res. A, **455**, 1 (2000).

[67] R. Szipöcs, K. Ferencz, Ch. Spielmann, F. Krausz, Opt. Lett. **19**, 201 (1994).

[68] P. S. Banks, M. D. Perry, V. Yanovsky, *et al.*, IEEE J. Quant. Elect. **36**, 268 (2000).

[69] W. Koechner, *Solid-State Laser Engineering*, 5th Edition (Springer–Verlag, Berlin, 1999).

[70] S. Ito, H. Nagaoka, T. Miura, *et al.*, Appl. Phys. B **74** 343 (2002).

[71] R. Weber, B. Neuenschwander, M. Mac Donald, *et al.*, J. Quant. Elect., **34** 1046 (1998).

[72] P. O'Shea, M. Kimmel, X. Gu, R. Trebino, Opt. Lett. **26**, 932 (2001); P. O'Shea, M. Kimmel, R. Trebino, J. Opt. B **4**, 44 (2002).

[73] A. Piskarskas, D. Podenas, A. Stabinis, *et al.*, in *Ultrafast Phenomina V*, G. R. Fleming, A. E. Siegman, eds., (Springer, Berlin, 1986) p. 142.

[74] A. Dubietis, G. Jonasauskas, A. Piskarskas, Opt. Commun. **88**, 437 (1992).

[75] I. N. Ross, P. Matousek, M. Towrie, *et al.*, Opt. Commun **144**, 125 (1997).

[76] B. Wattellier, I. Jovanovic, C. P. J. Barty, in 2003 *Conference on Lasers and Electro-Optics Technical Digest*, paper CME1.

[77] I. J. Waxer, V. Bagnoud, I. A. Begishev, *et al.*, Opt. Lett. **28**, 1245 (2003).

[78] I. Jovanovic, C. A. Ebbers, C. P. J. Barty, Opt. Lett. **27** 1622 (2002).

[79] D. T. Palmer, X. J. Wang, R. H. Miller, *et al.*, *Proceedings of the 1997 Particle Accelerator Conference*, 1997, edited by M. Comyn, M.K. Craddock, M. Reiser, and J. Thomson, (IEEE, Piscataway, NJ, 1998), 2687.

[80] R. Alley, V. Bharadwaj, J. Clendenin, *et al.*, Nucl. Instrum. Methods Phys. Res. A, **429**, 324 (1999).

[81] D. Yu, T. Lee, S. Rajagopalan, J. Chen, *Proceedings of the 1997 Particle Accelerator Conference*, 1997, edited by M. Comyn, M.K. Craddock, M. Reiser, and J. Thomson, (IEEE, Piscataway, NJ, 1998), 2802.

[82] W.J. Brown, S. Trotz, K.E. Kreischer, *et al.*, Nucl. Instrum. Methods Phys. Res. A, **425**, 441 (1999).

[83] F. B. Kiewiet, O. J. Luiten, G. J. H. Brussaard, et al., *Proceedings of the European Particle Accelerator Conference*, 2000,Vienna, Austria, 1660.

[84] G. P. Le Sage, H. X. C. Feng, L. L. Laurent, *et al.*, IEEE Trans. Plasma Sci. **24**, 781 (1996).

[85] H. Wiedemann, *Particle Accelerator Physics: Basic Principles and Linear Beam Dynamics* (Springer-Verlag, Berlin 1993).

[86] K. T. McDonald, IEEE Trans. Elect. Dev., **35**, 2052 (1988).

[87] S. C. Fultz, C. L. Whitten, IEEE Trans. Nuc. Sci. **18**, 533 (1971).

[88] S. Kane, J. Squier, IEEE J. Quant. Elec., **31**, 2052 (1995).

[89] *CVI Laser Catalog* (CVI Laser, Albuquerque, NM 2003).

[90] J. Kuba, R. Shepherd, R. Booth, *et al.*, Proc. SPIE, **5194**, 183 (2004).

[91] G. P. Le Sage, S. G. Anderson, T. E. Cowan, et al., *Proceedings of The Ninth Workshop on Advanced Accelerator Concepts*, Sante Fe, New Mexico, 2000, edited by P. L. Colestock, S. Kelley (AIP Conf. Proc. 569, 2001), 391.

[92] B. E. Carlsten, Nuc. Inst. Meth. Phys. Res. A **285**, 313 (1989).

[93] J. Rosenzweig, E. Colby, *Advanced Accelerator Concepts*, 1994, edited by P. Schoessow, (AIP Conf. Proc. 335, 1995), 724.

[94] J. W. Wang, G. A. Loew, Stanford Linear Accelerator Center, SLAC-PUB-7684 (1997).

[95] Y. J. Chen, Nucl. Instrum. Methods Phys. Res. A, **279**, 433 (1989).

[96] G. P. LeSage, Ph. D. Thesis, University of California at Los Angeles, 1997.

[97] E. C. Landahl, Ph. D. Thesis, University of Californa at Davis, 2002.

[98] C. Spielmann, P. F. Curley, T. Brabec , F. Krausz, IEEE J. Quant. Elect., 30, 1100 (1994).

[99] A. Stingl, M. Lenzner, C. Spielmann, *et al.*, Opt. Lett., 20, 602 (1995).

[100] M. A. Allen, R.S. Callin, H. Deruyer, *et al.* , Stanford Linear Accelerator Center, SLAC-PUB-4650 (1988).

[101] G. P. Le Sage, C. V. Bennett, W. E. White, *et al.*, Phys. Plasmas, 5, 2048 (1998).

[102] R.H. Fowler, L. Nordheim, Proc. R. Soc. London Ser. A, 119, 173 (1928).

[103] B. Kulke, M. J. Burns, T. J. Orzechowski, Rev. Sci. Inst., 58, 1153 (1987).

[104] T. Nakazato, M. Oyamada, N. Niimura, *et al.*, Phys. Rev. Lett., 63, 1245 (1989).

[105] F. V. Hartemann, Phys. Rev. E, 61, 972 (2000).

[106] B. E. Carlsten, Phys. Rev. E, 54, 838 (1996).

[107] Y. Li, Z. Huang, M. D. Borland, S. Milton, Phys. Rev. Spec. Top. Accel. and Beams, **5**, 044701 (2002).

[108] Transmission data available at http://physics.nist.gov/PhysRefData/FFast/html/form.html

[109] L. T. Hudson, A. Hennis, R. D. Deslattes *et al.*, Rev. Sci. Inst. **73,** 2207 (2002).

[110] T. Srinivasan-Rao, I. Ben-Zvi, J. Smedley, *et al.*, *Proceedings of the 1997 Particle Accelerator Conference*, 1997, edited by M. Comyn, M.K. Craddock, M. Reiser, and J. Thomson, (IEEE, Piscataway, NJ, 1998), 2790.

[111] S. Anderson, Private Communication

[112] A. H. Chin, R. W. Schoenlein, T. E. Glover, *et al.*, Phys. Rev. Lett., **83** 336 (1999).

[113] F. V. Hartemann, W. J. Brown, S. G. Anderson, *et al.* Bull. Am. Phys. Soc. **48**, 196.